UNIVERSITY OF CALIFORNIA SAN DIEGO

Ocean-Island Interactions in the Western Pacific

A dissertation submitted in partial satisfaction of the
requirements for the degree Doctor of Philosophy

in

Oceanography

by

Travis Allen Schramek

Committee in charge:

Eric Terrill, Co-Chair
Bruce Cornuelle, Co-Chair
Sarah Giddings
Myrl Hendershott
Mark Merrifield
Geno Pawlak
Kraig Winters

2018

The dissertation of Travis Allen Schramek is approved, and it is acceptable in quality and form for publication on microfilm and electronically:

_____

_____

_____

_____

_____

_____

Co-Chair

_____

Co-Chair

University of California San Diego

2018

DEDICATION

To Patrick and Lori Colin of the Coral Reef Research Foundation, for their commitment to exploring the world's oceans. Your efforts in sustained observations and collaboration are the base upon which my dissertation stands.

And to my family, for your unwavering support and fostering my love of the water, both of which brought me to this work and carried me through it.

EPIGRAPH

We certainly cannot predict future events exactly if we cannot even measure the present state of the universe precisely!

Stephen Hawking

TABLE OF CONTENTS

Signature page……... iii

Dedication…….. iv

Epigraph……. v

Table of Contents…….. vi

List of Figures..……... ix

Acknowledgements…… xiv

Vita…… xviii

Abstract of the Dissertation……... xix

Introduction……... 1

References……..... 5

Chapter 1 Depth-dependent thermal stress around corals in the tropical Pacific Ocean..……...…… 10

1.1 Introduction…… 10

1.2 Methods……..…… 13

1.2.1 In-situ observations and gridded products……. 13

1.2.2 Filtering and the Oceanic Niño Index…...……. 14

1.2.3 Reconstructing temperature using regression techniques…….…. 14

1.2.4 Determining thermal stress – Degree Heating Weeks... 15

1.3 Results ……...…… 16

1.4 Conclusion and Discussion……..……... 19

1.5 Acknowledgements…… 20

1.6 Appendix - Supplemental Information…….. 26

1.7 References…….. 36

Chapter 2 Coastally Trapped Waves around Palau……..……. 40

2.1 Introduction……...……. 40

2.2 Methods ……..……... 43

2.2.1 Observational array……..……... 43
2.2.2 Statistical techniques…....…….... 44
2.2.3 Modeling the Wave-Guide..……...……... 45
2.3 Results…….……... 47
2.3.1 Background State of the Local Waters around Palau.... 47
2.3.2 A Strong Forcing Event – Typhoon Haiyan…….. 50
2.3.3 Modeling Results……..……. 53
2.4 Conclusion and Discussion….…… 56
2.5 Acknowledgements…… 58
2.6 Appendix…… 73
2.7 References…….. 78
Chapter 3 Channel flow through an island group driven by geostrophic flows and topographic effects…….. 83
3.1 Introduction…… 84
3.2 Data and Methods……... 85
3.2.1 Observational array and gridded products…….…… 85
3.2.2 Statistical techniques…..……... 86
3.2.3 High resolution ocean model…… 86
3.3 Results…… 87
3.3.1 The along-channel momentum balance…..……... 87
3.3.2 Pressure gradient related channel flow…….. 88
3.3.3 1/120° x 1/120° modeling application.....…….. 89
3.3.4 Relationship between channel current and regional flows.....……. 91
3.3.5 Reassessing the force balance…….……. 92
3.4 Conclusions and Discussion…..…….. 93
3.5 Acknowledgements…… 95
3.6 References……..... 108
Chapter 4 The role of the surface and internal tides in driving flow on the edge of an island……. 110
4.1 Introduction…… 110

4.2 Data and Methods……... 112
4.2.1 Observational array……..…… 112
4.2.2 Statistical techniques…...……. 112
4.3 Results…… 113
4.3.1 Characteristics of the flow field…….…… 113
4.3.2 Evidence of an internal tide in the tidal currents……... 113
4.3.3 The role of stratification…… 115
4.4 Conclusion and Discussion…..……... 116
4.5 Acknowledgements…… 118
4.6 References……..... 132

LIST OF FIGURES

Figure 1.1: a. Mean temperature profiles from Palau (observed – solid lines, MLR modeled – dashed lines), at Short Drop Off (Figure 1.S1.c) on the East coast of Palau, during all El Niño (ONI >= 0.5 – red) and La Niña (ONI <= -0.5 – blue) events as well as a neutral……. 22

Figure 1.2: a. Weekly-averaged temperatures were reconstructed for Short Drop Off (Figure 1.S1.c), on the East coast of Palau, using multiple linear regressions for depths between 0 and 90 m and are shown for the time period of Jan 1985 to Jun 2017……. 23

Figure 1.3: The spatial progression of the Rossby wave that shut down the 2015-2016 El Niño event can be seen in regional sea level anomaly (SLA), displayed as monthly averages, as the warm pool progressed from the central tropical Pacific in Feb 2016……. 24

Figure 1.4: a. DHW was computed from the CRW CoralTemp SSTs supplied for Short Drop Off (black line). This matches the record of DHW supplied by CRW (not shown). b. DHW was computed for the temperature reconstructions between 0 and 90 m, which shows….. 25

Figure 1.S1: a. Regional map showing the location of Palau in the western Tropical Pacific. b. A bathymetric map of Palau where the land is masked in gray and the locations of the three vertical temperature arrays, named Short Drop Off (SDO) (yellow circle square)…… 28

Figure 1.S2: Mean profiles of temperature records from Short Drop Off (Figure 1.S1.c), binned by (a) SST and (b) SLA…… 29

Figure 1.S3: NOAA Coral Reef Watch – CoralTemp 5km weekly averaged sea surface temperatures (a. Short Drop Off - blue, b. Ulong Rock - orange, c. West Channel - yellow) obtained from the NOAA Coral Reef Watch – CoralTemp product compared to the observations…. 30

Figure 1.S4: The results of the multiple linear regression analysis at Short Drop Off (a & d), Ulong Rock (b & e), and West Channel (c & f) using weekly averaged data. The fraction of variance predicted by each input variable in the multiple linear regression (a, b & c) all exhibit. 31

Figure 1.S5: a. Weekly-averaged in-situ temperature observations are shown between Jan 2015 and Jun 2017. Observations from 2017 (gray background) were withheld from the modeling training sets to allow for comparison. b. MLR modeled temperatures throughout.. 32

Figure 1.S6: Temperature records (black) and the corresponding reconstruction (red) using SLA and SST in the multiple linear regression techniques are displayed for the three sites, Short Drop Off (a-f), Ulong Rock (e-i) and West Channel (j-o)……. 33

Figure 2.1: Positions of observational instrumentation deployed around Palau during May – December 2013 including thermographs (red-circles, with labels), water level gauges (green-squares), an ADCP (yellow-diamond), and the meteorological station……. 60

Figure 2.2: Mean ARGO profile for 2004-2014 taken from grid point 7° 25.00N, 134° 45.00E. (a) Temperature, (b) Salinity, (c) Density, (d) Brunt-Visalia Frequency, (e) Vertical Temperature Gradient……..... 61
Figure 2.3: Offshore bathymetric profiles taken from the (a) East and (b) West coasts shown in Figure 1. Mean offshore profiles, solid lines, were computed from the three representative profile, dashed lines, from each region……..…… 62
Figure 2.4: Wind vectors from M1 (Table 2.1 and Figure 1) show the monsoonal wind busts throughout the observational period. The vertical red line in both (a) and (b) indicate when Typhoon Haiyan passed through Palau on 6 November 2013……. 63
Figure 2.5: Cross-correlations between the band-passed (3.5-20 Days) temperature records for a range of time lags (hours) between T1 and T2-T6. The cross-correlations have not been normalized to their max value to allow for comparison between successive sites... 64
Figure 2.6: Meteorological Data recorded between 04 – 14 November 2013 at site M1 (Figure 1and Table 2.1). Typhoon Haiyan's impact can be seen on 6 November in the wind vectors (a) and sea level pressure.. 65
Figure 2.7: ADCP observations at C1 (Figure 1 and Table 2.1) in the central region of the East coast of Palau between 17 October – 26 November 2013. (a) Depth averaged, and Godin filtered current velocities. These data are rotated into principal axis where major… 66
Figure 2.8: De-tided pressure gauge observations from sites P1-P5 (a-e). Each of these pressure records were used as input in the Matlab program t_tide and the predicted tidal components of SSH were removed from the record leaving the residual water level (thin line)……. 67
Figure 2.9: a. T-X diagram of demeaned temperature records from T1 to T6 (Figure 1) at 57m, black, placed at their respective distances from observation point T1. Distance between sites is measured clockwise around the island chain, as noted in Table 2.1……. 68
Figure 2.10: a. Velocity mode structure for the first three baroclinic modes computed using the vertical structure equation applied to the mean ARGO profile in Figure 2. The profile was extended to a depth of 4500 m via linear interpolating from the deepest ARGO derived…. 69
Figure 2.11: Trapped waves computed by BC85 for a range of user provided along-coast wave numbers. Quasi dispersion curves can be visualized extending through a range of frequency wave number pairings. Modeled phase speeds range between 0.07 m/s and 0.40... 70
Figure 2.S1: a. The meridional component of the wind field observed at M1 (black line) and M2 (red line) are presented for the period between 21 May and 31 October 2013. b. Cross-correlations between the two wind time series presented in (a) over a range of lags in days… 73
Figure 2.S2: T-X diagram of de-tided water level records (thin line – demeaned and de-tided, thick line – demeaned, de-tided and godin filtered) from P1 to P5 (Figure 2.1) at depths ranging from 2 m to 17 m, black, placed at their respective distances from observation point… 74

Figure 2.S3: Spectra computed over 60-day period around Typhoon Haiyan (using 20 day windows). The gray lines indicate (left to right) the inertial band, 2*internal band, diurnal band and semidiurnal band. Locations of P1 through P5 are listed in Table 2.1 and are shown…. 75
Figure 2.S4: a. Water level (black) observed by the Malakal Harbor NOAA station and the predicted tides (blue) computed using the Matlab package t_tide. The red line indicates when Typhoon Haiyan passed through Palau on 6 November 2013. b. Residual water…… 76
Figure 2.S5: a. Depth averaged meridional velocity (left axis) from C1/P1 (same sight) versus pressure record that has been de-tided (right axis). Both records have been godin filtered. b. Temperature records from both 57 m (black) and 90 (m) stations at T1 (right axis)……..…….. 77
Figure 3.1: a. Palau is located in the tropical western Pacific at 7.5°N and 134.5°E, north of Papua New Guinea and east of the Philippines. b. The locations of the observation stations maintained by pressure loggers (P* - orange circles) and a current meter (C* - blue circle)... 97
Figure 3.2: Water level, derived from observations of in situ pressure between 20 and 28 m of water depth of the fore reefs encircling the major barrier reef of Palau. The mean water level over the course of the deployment, from March 2016 through March 2017…….…….... 98
Figure 3.3: Mean sea level anomaly, computed using the observations of pressure from Palau's fore reefs (OBS - orange line), shown in Figure 3.2, is shown in comparison to the NOAA tide gauge station located in Malakal Harbor (MKH - gold line) and the CMEMS….. 98
Figure 3.4: a. Depth averaged East (black) and North (red) current vectors shown between March 2014 and June 2018. b. Godin filtered depth averaged current vectors show the subtidal signals observed through the 4-year observational record……... 99
Figure 3.5: The relationships between the observed zonal flow through the channel (blue lines, left y-axes) and the differences in sea surface height, denoted as Δη, across the island (orange lines, right y-axes) is examined…….…. 100
Figure 3.6: a. The full model domain is displayed for the ROMS run PALAU_120B, where the subdomains displayed in (b) and (c) are designated by the solid and dashed black lines, respectively. b. The southern extent of Palau in the model domain is shown……..……. 101
Figure 3.7: a. The relationships between the modeled zonal flow through the channel (blue solid line, left y-axes) and the differences in sea surface height across the island (orange line, right y-axes), shown as Δη, is examined. b. Time lagged cross correlations……..... 102
Figure 3.8: Daily mean output for (a) June 19th, 2016 and (b) July 1st, 2016 in the ROMS model run, denoted as Palau_120B, with 1/120° x 1/120° resolution is shown. Currents vectors, which are subsampled for display purposes, are shown as arrows,…….. 103

Figure 3.9: The relationships between the modeled along channel flow (blue lines, left y-axes) and the differences in sea surface height across the island (orange lines, right y-axes), shown as $\Delta\eta$, is examined. Velocities were taken from the grid points noted in Figure 3.6c..… 104
Figure 3.10: Correlation coefficients computed between the observed zonal pressure gradient, $\Delta\eta$, (a, b), as shown in Figure 3.5b between March and September 2016, and the CMEMS geostrophic velocity output in both the u (left column) and v (right column)…… 105
Figure 3.11: Monthly mean surface currents as observed by HF Radar off of the east coast of Palau during (a) June, (b) July, and (c) August 2016. Vectors show the direction of the flow and are auto scaled. Magnitude is shown by color……..…..…….……... 106
Figure 3.12: a. Equating the pressure term (y-axis) and friction term (x-axis), excluding the drag coefficient, allows the fitting of a slope to obtain a drag coefficient that relates the two terms. The slope for the linear fit between the two terms is noted in the figure as C_D=0.0009 ~10^{-4}. 107
Figure 4.1: a. Regional map of the western tropical Pacific with a black box denoting the region around the island nation of Palau, as depicted in b. b. Palau is shown with gray contours denoting the 100, 500 and 1000 m isobaths…… 119
Figure 4.2: Top. Depth averaged East (black) and North (red) current vectors shown between March 2014 and June 2018. Bottom. Godin filtered depth averaged current vectors show the subtidal frequency signals observed through the 4-year observational record.……...… 120
Figure 4.3: Rotary spectra of the depth averaged currents between Mar2014-Jun2017. There is elevated energy in the dirnal (D) and semidiurnal (SD) tidal bands as well as their harmonics. Broadband excitation is seen around the inertial band denoted by the gray vertical band...…… 120
Figure 4.4: Spectra of the sea level observations made by the ADCP located on Hydrographers Bank. Elevated energy is seen at the diurnal (D) and semidiurnal (SD) bands as well as the tidal harmonics…...…… 121
Figure 4.5: Spectrograms of depth averaged current vectors, East (top) and North (bottom), between March 2014 and June 2018. There is elevated energy at the semidiurnal (dash dot line), diurnal (dashed line) and inertial (solid line) bands. Energy levels are higher..…… 122
Figure 4.6: Top. Sea level anomaly observations from Malakal Harbor (black) and rotated depth-averaged currents (red), both normalized by their respective variances, band passed for the semidiurnal band. Bottom. SLA data from Malakal Harbor (black) and rotated depth-averaged.… 123
Figure 4.7: Top. Observed currents were high-pass filtered (blue), maintaining periods less than 2 days. Tidal constituents were computed using the observations from March 2014 through March 2015 and then tides were predicted for the whole observational window……... 124
Figure 4.8: Top. The sea level anomaly observations from Malakal Harbor (black) and rotated depth-averaged currents (red), both normalized by their respective variances, band passed for the semidiurnal band. Bottom. SLA data from Malakal Harbor (black)……. 125

Figure 4.9: Wavelet coherence is shown between the surface tide, represented by the SLA observed by the ADCP for this computation, and major-axis velocity in the semidiurnal and diurnal bands between March 2014 and March 2015. Elevated levels of coherence are see……. 126
Figure 4.10: Wavelet coherence is shown between the surface tide, represented by the SLA observed by the ADCP for this computation, and major axis velocity in the (a) semidiurnal and (c) diurnal bands between March 2014 and March 2015…… 127
Figure 4.11: Wavelet coherence between SLA observed by the ADCP and tidal band currents (x-axis) versus the amplitude of the tidal band currents. Semidiurnal (top row) and diurnal (bottom row) bands both show a relationship between the coherence…….. 128
Figure 4.12: Sea level anomaly (top) and the depth profile of temperature at West Channel between 0 and 65 m of depth (bottom) are compared. An internal tide corresponding with peak low tide is present during this time period in October of 2014…… 129
Figure 4.13: Sea level anomaly (top) and the depth profile of temperature at West Channel between 0 and 65 m of depth (bottom) are compared. Large amounts of internal wave driven variability is present during this time period in January and February of 2015……. 130
Figure 4.14: Sea level anomaly (top) and the depth profile of temperature at West Channel between 0 and 65 m of depth (bottom) are compared. An internal tide corresponding with peak low tide is present during this time period in September 2014..... 131

ACKNOWLEDGEMENTS

I would for like to thank my advisor, Eric Terrill, for teaching me how to be a field-going oceanographer. He gave me countless opportunities to develop my skills. These experiences coupled with his training about how to approach problems, from a higher level down through the finer details, facilitated a diverse means of intellectual growth, for which I am be a better scientist and person. I thank him for the opportunity to have worked with him in this capacity as well and his support and efforts in advising me.

Bruce Cornuelle spent years helping me to refine my problem-solving skills and theoretical understanding when approaching oceanographic questions. I thank him for being my co-advisor and these efforts. In the final years of my graduate work, Mark Merrifield enhanced my ability to find the story within the data and the context for it in the larger field of ocean sciences. I thank him for his dedication to engaging with students and fostering their curiosities. I also acknowledge my committee members, Drs., Sarah Giddings, Geno Pawlak, Myrl Hendershott and Kraig Winters, for their time and insightful feedback throughout the process. The body of work contained here is much better due to your inputs.

I would like to acknowledge the community of professors whom dedicate substantial efforts to rearing the next generation of ocean scientists here. For me, Dr Myrl Hendershott exemplified commitment to teaching at a level I have rarely seen. As a member of the teaching community here at SIO, he has spent countless hours engaging with new crops of SIO COAP students. Each year Myrl dedicates his off hours to doing board work with first year students, helping them learn to think freely about new problems in route to successful departmental exams. I have found myself revisiting the problem solving techniques throughout my graduate work and

look back to those moments of engagement with great appreciation. I am fortunate to have been your student.

The Coastal Observing Research and Development Center at Scripps Oceanography has provided me a home to learn in over the past six plus years. The staff at CORDC are a daily example of what is possible when talented people are tasked to challenging problems. I'd like to acknowledge Lisa Hazard for making the ship sail and Shannon Scott for his efforts in training me on how to operate in the field. Extensive amounts of fieldwork time with Andy Nager, Myles Sveryud, Evan Walsh, Bob Hess, Mike Jilka, Joel Hazard, Tom Cook, and Carlos Garcia-Moreno made for a fantastic set of experiences. Thanks for putting up with me. Both Megan Cimino and Sophia Merrifield were wonderful mentors and I thank them for their support.

The Coral Reef Research Foundation has been an essential collaborator in my graduate experience. I graciously acknowledge their efforts in facilitating our observational work in Palau. My dissertation has relied heavily on their generous sharing of observations collected over nearly two decades. I thank them for their efforts in collecting these observations, allowing me the opportunity to work with them, and their unfettered support throughout the process.

The modeling component of my 3rd chapter was done by Harper Simmons and his group at the University of Alaska - Fairbanks. I thank them for allowing me access the model output and efforts in helping me to understand the model itself.

Thank you to the Office of Naval Research, whom funded the entirety of my PhD. ONR has a strong commitment to the advancement of engineering and answering fundamental questions in oceanography. The ocean sciences are greatly advanced due to ONR's collective effort and backings.

I would like to acknowledge the members of Project Recover at the University of Delaware, the Bent Prop Project, and here at Scripps Oceanography. While my experiences working with this project are not contained in any of the chapters of my dissertation, they have been a thread woven through the entirety of my graduate experience. The efforts of this project have been an inspiration for me and it has been an absolute pleasure to work with them on this endeavor. I would like to acknowledge both Mark Moline and Patrick Scannon for their mentorship and efforts over these last six years.

Being a part of the SIO community is a true highlight of being a graduate student here. The student body has been a source of comradery through both success and struggle. I'd like to thank the Cohort of 2012 and the AOS student group for being such a delightful group of people to share time with at SIO. Jeff Campana was a forever patient office mate. I thank him for being a great mentor and friend. Eric Gallimore and Allison Ho have been great lab mates and I thank them for their support and friendship. To all of the people whom have soaked in the waters off of La Jolla or hustled around east country with me, including Nick Pizzo, Noah Ben-Ardent, Nick Cavanaugh, Evan Goodwin, Eric Orenstein, and many more, thanks for sharing these passions. I am fortunate to have shared time here with all of you.

Kasia Zaba, thank you for everything you are and have done for me in these past years. Your endless support and partnership made an indelible mark on my time in graduate school and who I have become. Thank you for showing me how to explore more freely and what it means to be a best friend. Many adventures lie ahead. I am as excited to head into this next one with you as I was the day we stepped off of the ferry in Dar es Salaam together.

Thank you to my family, both immediate and extended, whom never flinched in helping me on this long academic and personal journey. I am thankful to my sister Dana, who is model of

tenacity that I could always look to for support while in graduate school. To my parents, anything I ever accomplish stands on the shoulders of your investments in Dana and I, and commitment to our family. The waters of St Joseph Sound are where my affinity with the ocean began. They lead me on a path the world around. Thank you for fostering these interests and passions. I am sure we will see it pay off some day. My gratitude is immeasurable.

Chapter 1, in full, has been published in Geophysical Research Letters. The dissertation author was the primary investigator and author of this paper: Schramek, T. A., Colin, P. L., Merrifield, M. A., & Terrill, E. J. (2018). Depth-dependent thermal stress around corals in the tropical Pacific Ocean. Geophysical Research Letters, 45, doi:10.1029/2018GL078782.

Chapter 2, in full, is under review at Continental Shelf Research, 2018, Schramek, Travis A.; Terrill, Eric J.; Colin, Patrick L.; Cornuelle, Bruce D. The dissertation author was the primary investigator and author of this paper.

Chapter 3, in part is currently being prepared for submission for publication of the material. Schramek, Travis A.; Merrifield, Mark A.; Colin, Patrick L.; Simmons, Harper; Merrifield, Sophia; Terrill, Eric J. The dissertation author was the primary investigator and author of this material.

Chapter 4, is coauthored by Merrifield, Mark A.; Colin, Patrick L.; Terrill, Eric J. The dissertation author was the primary investigator and author of this material.

VITA

2010 Bachelor of Science (Ocean Engineering), Florida Institute of Technology

2015 Master of Science (Mechanical Engineering), University of California San Diego

2018 Doctor of Philosophy (Oceanography), University of California San Diego

PUBLICATIONS

Terrill, E. J., M.A. Moline, P. Scannon, E. Gallimore, **T. A. Schramek**, A. Nager, R. Hess, M. Cimino, P. L. Colin, A. Pietruszka, M. Anderson, 2017. Project Recover: Extending the applications of unmanned platforms and autonomy to support underwater MIA searches. Oceanography 30(2), 150-159.

Cimino, M., P. L. Colin, **T. A. Schramek**, S. Lindberg, M. Domeier, E. J. Terrill, 2018. Oceanographic, acoustic and remote approaches reveal the spatio-temporal dynamics of blackfin snapper at an aggregation site in Palau. Marine Ecological Progress Series, doi: 10.3354/meps12651.

Schramek, T. A., Colin, P., Merrifield, M., Terrill, E., (2018). Depth-dependent thermal stress around corals in the tropical Pacific Ocean. Geophysical Research Letters, doi:10.1029/2018GL078782.

ABSTRACT OF THE DISSERTATION

Ocean-Island Interactions in the Western Pacific

by

Travis Allen Schramek

Doctor of Philosophy in Oceanography

University of California San Diego, 2018

Eric Terrill, Co-Chair

Bruce Cornuelle, Co-Chair

Coastal processes around islands encompass dynamics on a range of scales with physics that can differ from typical continental shelves due to steeper bathymetry, potentially allowing the surrounding basin waters to ‘communicate’ quickly to the shoreline. This thesis work advances our understanding about these interactions, using a unique set of nearshore oceanographic

observations from around the island group encompassed by the Republic of Palau in the tropical western Pacific.

The influence of large scale and climatic variability on nearshore island environments can be seen through an empirical model of fore reef temperature structure based on SST and sea level anomaly (SLA) made from nearly two decades of temperature observations (2-90m depth) from three stations around Palau. SLA complements SST by providing a proxy for vertical isotherm displacements driven by local and remote winds on intraseasonal to interannual time scales. Thermal stress on coral ecosystems can now be forecast into the mesophotic zone using this means of predicting subsurface temperatures which are easily accessible for the tropical Pacific.

Baroclinic variability around islands has multiple drivers on a range of time scales. Observations of temperature and currents from around the main island group of Palau exhibit a persistent presence of baroclinic coastally trapped waves and internal tides. The largest amplitude signals of coastally trapped waves in fore reef temperature were concurrent with the passage of Typhoon Haiyan, which crossed the northern most Palauan islands in November of 2013. The sub-inertial signals present after Typhoon Haiyan were tracked propagating around the island group for upwards of a week after the typhoon passed. Internal tides were also deemed to be present, but with varying amplitude and phase modulating in and out of phase with the local surface tide.

Surface currents impinging upon Palau have a direct impact on the local sea level field around the island group. An array of nearshore pressure gauges, in depths of 20-28 m, encircling the island group and a high resolution (1/120° x 1/120°) regional circulation model are used to examine the space-time characteristics of the flow in a channel in the southern extent of Palau in comparison to the large-scale currents near the island group. A balance between the along-channel pressure difference and bottom friction in the channel was inferred based on the current and

pressure observations and the high-resolution model simulations. A drag coefficient for the channel, computed using in situ observations, is $O(10^{-3}\text{-}10^{-4})$. Variations in large-scale zonal currents correlate with the pressure difference across the channel as well as the along-channel flow. The model simulations indicate that as the large-scale flow impinges on the island group, topographic blocking results in a pressure difference on either side of the island which causes a pressure gradient along the channel.

The fore reef waters of Palau are shown to be influenced by a range of dynamics across all spatial and temporal scales of our observations. There is an apparent omnipresence of both internal tides and coastally trapped waves throughout the observational window which provide a regular cycling of temperature at depth. These waves have their largest effects at the thermocline, the depth of which can be estimated in this region using only surface variables, as described above. Together, our assessments of these dynamics provide an enhanced perspective on the potential for thermal conditioning of benthic communities living on the outer reef slopes and an advanced perspective of how the large-scale oceanographic field translates to the fore reef environment.

Introduction

Islands in the open ocean typically lack shelves and are characterized by steep bathymetric slopes, resulting in a connection of the high seas to vibrant coastal ecosystems on their coastlines. Offshore oceanographic fields can translate directly to shore due to these rapid shifts from deep to shallow water. The mean oceanographic fields in the Tropical Pacific, a region home to hundreds of islands, has a predominantly zonal structure (Talley, 2011). Equatorial winds, which include the trades, drive zonal flows across the Pacific basin. Seasonal patterns in wind fields vary across the tropics, with a large monsoonal influence present in the western Pacific (Kubota et al., 2005). Temporal variability in this region is dominated by signals at the interannual time scale, such as the El Niño-Southern Oscillation (ENSO; Ando & Hasegawa, 2009). Meridional variability in these interannual signals (Widlansky et al., 2014) drive varied responses on island fore reefs residing on opposing sides of the equator. On shorter time scales, typhoons play an active role in the region (D'Asaro et al., 2011) having substantial impact on island communities throughout. High intensity winds from the typhoons drive the generation of surface gravity waves (Charnock, 1955) compounding the effects of storm surge (Marks et al., 1998), intensifying shoreline change (Darwin, 1842; Ford & Kench, 2014) and shallow water ecosystem damage (Ogg & Koslow, 1978; Stephenson et al., 1958). The surface wave field generated by tropical systems propagate from the immediate vicinity of the storm system in the form of swell, allowing them to influence regions far from the storm. Additionally, both cold wakes (Shay et al., 1992) and coastally trapped waves (Merrifield, 2002) can be lasting signatures of these large atmospheric forcing events.

Observational physical oceanography around islands in the Tropical Pacific has a rich history, likely starting with the stick maps of the seafaring communities living in the Marshall Islands, first documented by Gulick (1862) as in existence in the 1200s. The charts were used to

plot how islands refracted surface wave fields, useful for maritime navigation when islands were out of sight (Genz et al., 2009). During World War II, Harold Sverdrup (1944), director of the Scripps Institution of Oceanography, played a critical role in developing wind and current maps of the Pacific for purposes of aiding downed aviators surviving in life rafts. These wind maps (and estimates of geostrophic currents) were based on large-scale barometric pressure observations. The role of remote and local wind forcing in driving variability in the fore reef oceanographic structure and lagoon flushing around islands and atoll systems were studied in the period after World War II (Munk & Sargent, 1948). Theoretical assessments of trapping of the large-scale ocean waves were later developed (Longuet-Higgins, 1967) and eventually tested in the case of Bermuda in the Atlantic (Hogg, 1980) and Hawaii in the Pacific (Merrifield, 2002; Munger & Cheung, 2008). Jarvis Island in the South Pacific allowed for a case study of what could be inferred about the large-scale currents impinging on an island through in situ observations of pressure offshore of an island's fore reefs (Roemmich, 1984). The biological implications of this flow field was assessed to better understand drivers of local ecological variability (Gove et al., 2006).

Islands have been shown to be centers of upper ocean productivity in the open sea (Caldeira et al., 2002; Doty & Oguri, 1956; Gilmartin & Revelante, 1974; J. M. Gove et al., 2016). There are biological implications of spatial gradients in the oceanographic environment, which can span across island groups or down to the scale of an individual island fore reef system. Meridional differences in oceanographic fields exist across the Line Islands, which straddle the equator, resulting in varied amounts of primary production on the fore reefs across this island group. Variations in primary production, food availability, and depth on a fore reefs drive trophic selection for coral species (Fox et al., 2018), connecting variability of the larger oceanographic environment to the ecosystem community scale. Furthermore, variability of oceanographic

properties across a single island group can drive spatial differences in community structure (J. Gove et al., 2015; Williams et al., 2013).

The island nation of Palau rises up from the Palauan Trench and sits at the western end of the Caroline Islands in the tropical western Pacific. This island group is home to some of the most diverse and unique coral ecosystems in the world (Colin, 2009). Palau is located at the mean latitude of the transition between two large zonal surface currents: the North Equatorial Current (NEC) to the north, flowing east-to-west, and the North Equatorial Counter Current (NECC) to the south, flowing west-to-east (Heron et al., 2006; Schönau & Rudnick, 2015). Both of these current systems have seasonal and interannual variability linked to ENSO (Hsin & Qiu, 2012; Qiu & Joyce, 1992; Zhao et al., 2013). A highly active internal wave field has been observed on Palau's fore reefs (Colin, 2009; Wolanski et al., 2004), generated both locally and remotely. Assessments have been made of the biological communities in Palau (Colin, 2009) including the impacts of large thermal stress events on local corals (Bruno et al., 2001; Golbuu et al., 2007), and work has been done to connect studies of nearshore biological activity to the physical oceanographic drivers (Cimino et al., 2018; Schramek et al., 2018). This island group serves as an ideal platform to study how the interaction of the synoptic ocean conditions with the nearshore environment, with attention paid to the resulting ocean habitat changes of the local marine ecosystems.

Just as nearshore environments around islands are influenced by the state of the offshore conditions, there is feedback from the shoreline to the synoptic field. To what degree this coupling is one- or two-way is still to be determined. Global operational ocean models are typically too coarse to resolve steep topographic features such as islands, where individual islands or even whole island groups are too small to be resolved by the model grid. The influence of these sub-grid-scale topographic features on the temporally-evolving ocean state are often parameterized, intending to

accurately characterize the interaction of the flow encountering the abrupt topography. Nearshore observations from islands groups such as Palau can help to identify how sub-grid-scale shoreline processes are related to open ocean dynamics, providing a means to assess the accuracy of these parametrizations.

This dissertation assesses how offshore oceanographic and atmospheric influence drive fore-reef variability, focusing on in-situ observations. An array of pressure sensors, thermographs and current meters were moored on the sea bottom around the outer perimeter of the main barrier reef of Palau at depths ranging from 2 m to 90 m. This observational campaign started in March 2010 and is still being maintained at the time of the completion of this dissertation. The array discussed in the pages of this dissertation was developed as the nearshore in situ observational component of a broad array of observations conducted by a multi-institution team of researchers on the Office of Naval Research directed research initiative focused on FLows Encountering Abrupt Topography (FLEAT). This campaign builds on nearly 20 years of fore reef temperature observations collected by the Coral Reef Research Foundation (CRRF), also included in this dissertation. An ocean circulation model run at a 1/120° x 1/120° resolution by FLEAT collaborators at the University of Alaska – Fairbanks (PALAU_120B) was used in support of the observations. Chapter 1 describes the relationship between sea level and fore reef temperature structure from the surface down to the mesophotic zone, between 30 and 150 m depth, and an application using this method to predict thermal stress metrics for coral ecosystems in this depth range. Chapter 2 assesses coastally trapped waves generated by Typhoon Haiyan, which passed over Palau in November of 2013. Chapter 3 investigates the force balance of subtidal flows in a channel at the southern end of the main island group of Palau and relates them to the regional

oceanographic fields. Chapter 4 studies tidal currents in that same channel, attempting to determine the influence of the surface and internal tides as well as other variability.

References

Ando, K., & Hasegawa, T. (2009). Annual Zonal Displacement of Pacific Warm Pool in Association with El Niño Onset. *Sola*, *5*, 149–152. https://doi.org/10.2151/sola.2009-038

Bruno, J., Siddon, C., Witman, J., Colin, P., & Toscano, M. (2001). El Niño related coral bleaching in Palau, Western Caroline Islands. *Coral Reefs*, *20*(2), 127–136. https://doi.org/10.1007/s003380100151

Caldeira, R. M. A., Groom, S., Miller, P., Pilgrim, D., & Nezlin, N. P. (2002). Sea-surface signatures of the island mass effect phenomena around Madeira Island, Northeast Atlantic. *Remote Sensing of Environment*, *80*(2), 336–360. https://doi.org/10.1016/S0034-4257(01)00316-9

Charnock, H. (1955). Wind stress on a water surface. *Quarterly Journal of the Royal Meteorological Society*, *81*(350), 639–640. https://doi.org/10.1002/qj.49708135027

Cimino, M., Colin, P., Schramek, T., Lindfield, S., Domeier, M., & Terrill, E. (2018). Oceanographic, acoustic, and remote approaches reveal the spatio-temporal dynamics of blackfin snapper at an aggregation site in Palau. *Marine Ecology Progress Series*, *601*, 185–201. https://doi.org/10.3354/meps12651

Colin, P. L. (2009). *Marine environments of Palau*. Taiwan: Indo-Pacific Press. Retrieved from http://coralreefpalau.org/wp-content/uploads/2017/04/Colin-PL-2009-Marine-Environments-of-Palau.pdf

Darwin, C. (1842). *The Structure and Distribution of Coral Reefs*. D. Appleton.

D'Asaro, E., Black, P., Centurioni, L., Harr, P., Jayne, S., Lin, I. I., et al. (2011). Typhoon-Ocean Interaction in the Western North Pacific: Part 1, *24*. https://doi.org/10.5670/oceanog.2011.91

Doty, M. S., & Oguri, M. (1956). The island mass effect. *ICES Journal of Marine Science*, *22*(1), 33–37.

Ford, M. R., & Kench, P. S. (2014). Formation and adjustment of typhoon-impacted reef islands interpreted from remote imagery: Nadikdik Atoll, Marshall Islands. *Geomorphology*, *214*, 216–222. https://doi.org/10.1016/j.geomorph.2014.02.006

Fox, M. D., Williams, G. J., Johnson, M. D., Radice, V. Z., Zgliczynski, B. J., Kelly, E. L. A., et al. (2018). Gradients in Primary Production Predict Trophic Strategies of Mixotrophic Corals across Spatial Scales. *Current Biology*. https://doi.org/10.1016/j.cub.2018.08.057

Genz, J., Aucan, J., Merrifield, M., Finney, B., Joel, K., & Kelen, A. (2009). Wave Navigation in the Marshall Islands: Comparing Indigenous and Western Scientific Knowledge of the Ocean. *Oceanography*, *22*(2), 234–245. https://doi.org/10.5670/oceanog.2009.52

Gilmartin, M., & Revelante, N. (1974). The 'island mass' effect on the phytoplankton and primary production of the Hawaiian Islands. *Journal of Experimental Marine Biology and Ecology*, *16*(2), 181–204. https://doi.org/10.1016/0022-0981(74)90019-7

Golbuu, Y., Victor, S., Penland, L., Idip, D., Emaurois, C., Okaji, K., et al. (2007). Palau's coral reefs show differential habitat recovery following the 1998-bleaching event. *Coral Reefs*, *26*(2), 319–332. https://doi.org/10.1007/s00338-007-0200-7

Gove, J., Williams, G., McManus, M., Clark, S., Ehses, J., & Wedding, L. (2015). Coral reef benthic regimes exhibit non-linear threshold responses to natural physical drivers. *Marine Ecology Progress Series*, *522*, 33–48. https://doi.org/10.3354/meps11118

Gove, J. M., Merrifield, M. A., & Brainard, R. E. (2006). Temporal variability of current-driven upwelling at Jarvis Island. *Journal of Geophysical Research: Oceans*, *111*(C12), 1–10. https://doi.org/10.1029/2005JC003161

Gove, J. M., McManus, M. A., Neuheimer, A. B., Polovina, J. J., Drazen, J. C., Smith, C. R., et al. (2016). Near-island biological hotspots in barren ocean basins. *Nature Communications*, *7*, 10581. https://doi.org/10.1038/ncomms10581

Gulick, L. H. (1862). Micronesia of the Pacific Ocean. *Nautical Magazine and Naval Chronicle*, *31*, 161-182,237-245,298-308,408-417.

Heron, S. F., Metzger, E. J., & Skirving, W. J. (2006). Seasonal Variations of the Ocean Surface Circulation in the Vacinity of Palau. *Journal of Oceanography*, *62*(1992), 413–426.

Hogg, N. G. (1980). Observations of Internal Kelvin Waves Trapped Round Bermuda. *Journal of Physical Oceanography*, *10*(9), 1353–1376. https://doi.org/10.1175/1520-0485(1980)010<1353:OOIKWT>2.0.CO;2

Hsin, Y. C., & Qiu, B. (2012). Seasonal fluctuations of the surface North Equatorial Countercurrent (NECC) across the Pacific basin. *Journal of Geophysical Research: Oceans*, *117*(6). https://doi.org/10.1029/2011JC007794

Kubota, H., Shirooka, R., Ushiyama, T., Chuda, T., Iwasaki, S., & Takeuchi, K. (2005). Seasonal Variations of Precipitation Properties Associated with the Monsoon over Palau in the Western Pacific. *Journal of Hydrometeorology*, *6*(Matsumoto 1992), 518–531. https://doi.org/10.1175/JHM432.1

Longuet-Higgins, M. S. (1967). On the trapping of wave energy round islands. *Journal of Fluid Mechanics*, *29*(04), 781–821. https://doi.org/10.1017/S0022112067001181

Marks, F. D., Shay, L. K., Barnes, G., Black, P., & al, et. (1998). Landfalling tropical cyclones: Forecast problems and associated research opportunities. *Bulletin of the American Meteorological Society; Boston*, *79*(2), 305–323.

Merrifield, M. a. (2002). Numerical simulations of a storm-generated island-trapped wave event at the Hawaiian Islands. *Journal of Geophysical Research*, *107*(C10), 1–10. https://doi.org/10.1029/2001JC001134

Munger, S., & Cheung, K. F. (2008). Resonance in Hawaii waters from the 2006 Kuril Islands Tsunami. *Geophysical Research Letters*, *35*(7), 1–7. https://doi.org/10.1029/2007GL032843

Munk, W. H., & Sargent, M. C. (1948). Adjustment of Bikini Atoll to ocean waves. *Eos, Transactions American Geophysical Union*, *29*(6), 855–860. https://doi.org/10.1029/TR029i006p00855

Ogg, J. G., & Koslow, J. A. (1978). The Impact of Typhoon Pamela (1976) on Guam's Coral Reefs and Beaches! *PACIFIC SCIENCE*, *32*, 14.

Qiu, B., & Joyce, T. M. (1992). Interannual Variability in the Mid- and Low-Latitude Western North Pacific. *Journal of Physical Oceanography*, *22*(9), 1062–1079. https://doi.org/10.1175/1520-0485(1992)022<1062:IVITMA>2.0.CO;2

Roemmich, D. (1984). Indirect Sensing of Equatorial Currents by Means of Island Pressure Measurements. *Journal of Physical Oceanography*, *14*(9), 1458–1469. https://doi.org/10.1175/1520-0485(1984)014<1458:ISOECB>2.0.CO;2

Schönau, M. C., & Rudnick, D. L. (2015). Glider observations of the North Equatorial Current in the western tropical Pacific. *Journal of Geophysical Research: Oceans*, *120*(5), 3586–3605. https://doi.org/10.1002/2014JC010595

Schramek, T. A., Colin, P. L., Merrifield, M. A., & Terrill, E. J. (2018). Depth-Dependent Thermal Stress Around Corals in the Tropical Pacific Ocean. *Geophysical Research Letters*, *0*(0). https://doi.org/10.1029/2018GL078782

Shay, L. K., Black, P. G., Mariano, A. J., Hawkins, J. D., & Elsberry, R. L. (1992). Upper ocean response to Hurricane Gilbert. *Journal of Geophysical Research: Oceans*, *97*(C12), 20227–20248. https://doi.org/10.1029/92JC01586

Stephenson, W., Endean, R., & Bennett, I. (1958). An Ecological Survey of the Marine Fauna of Low Isles, Queensland. *Marine and Freshwater Research*, *9*(2), 261–318. https://doi.org/10.1071/mf9580261

Sverdrup, H. (1944). *The Use of Cloth Survival Charts in the Navigation of Rubber Rafts* (WWII Cloth Escape Charts No. OPNAV-16-V#S109). Retrieved from https://doi.org/10.1080/03091928908208894

Talley, L. D. (2011). *Descriptive Physical Oceanography: An Introduction*. Academic Press.

Widlansky, M. J., Timmermann, A., Mcgregor, S., Stuecker, M. F., & Cai, W. (2014). An Interhemispheric Tropical Sea Level Seesaw Due to El Nino Taimasa. *Journal of Climate*, *27*(3), 1070–1081. https://doi.org/10.1175/JCLI-D-13-00276.1

Williams, G. J., Smith, J. E., Conklin, E. J., Gove, J. M., Sala, E., & Sandin, S. a. (2013). Benthic communities at two remote Pacific coral reefs: effects of reef habitat, depth, and wave energy gradients on spatial patterns. *PeerJ*, *1*, e81. https://doi.org/10.7717/peerj.81

Wolanski, E., Colin, P., Naithani, J., Deleersnijder, E., & Golbuu, Y. (2004). Large amplitude, leaky, island-generated, internal waves around Palau, Micronesia. *Estuarine, Coastal and Shelf Science*, *60*(4), 705–716. https://doi.org/10.1016/j.ecss.2004.03.009

Zhao, J., Li, Y., & Wang, F. (2013). Dynamical responses of the west Pacific North Equatorial Countercurrent (NECC) system to El Ni??o events. *Journal of Geophysical Research: Oceans*, *118*(6), 2828–2844. https://doi.org/10.1002/jgrc.20196

Chapter 1:

Depth-dependent thermal stress around corals in the tropical Pacific Ocean

Thermally driven bleaching events are a growing concern for reef ecosystems across the tropics. To assess and predict thermal stress impacts on reefs, remotely observed sea surface temperature (SST) commonly is used, however, reef communities typically extend to depths where SST alone may not be an accurate measure of in-situ variability. Here, nearly two decades of temperature observations (2-90 m depth) at three stations around Palau are used to develop an empirical model of temperature variability versus depth based on SST and sea level anomaly (SLA). The technique yields depth-averaged R2 values > 0.88, with SLA predicting fore-reef temperatures near the thermocline and SST capturing upper mixed layer temperatures. SLA complements SST by providing a proxy for vertical isotherm displacements driven by local and remote winds on intraseasonal to interannual time scales. Utilizing this concept, thermal stress on corals can be predicted from the surface through the mesophotic zone.

1.1 Introduction

Thermal stress is a major driver of coral bleaching, which threatens coral reefs around the world (Hughes et al., 2018; Langlais et al., 2017). Climate change and warming oceans adversely impact coral communities (Hughes et al., 2018; Wellington et al., 2001), and with no indication of immediate relief (Donner, 2009; Hoegh-Guldberg, 1999; Langlais et al., 2017), marine ecosystems (Glynn, 1993) and the social and economic systems dependent on them (Bridge et al., 2013, p. 201) are threatened. Sea surface temperature (SST) is the principal ocean parameter used to predict coral bleaching (Gleeson & Strong, 1995; Liu et al., 2006, 2014; Strong et al., 2004) and to derive

metrics quantifying thermal stress in surface waters, such as Degree Heating Weeks (DHW) (Strong et al., 2004). The depth/temporal variability of thermal regimes on reef systems has been understudied leading to a lack of understanding of thermal stress on corals through the extent of their depth range. Deeper reef waters in the mesophotic zone (Baker et al., 2016; Kahng et al., 2010; Lesser et al., 2009), between 30-150 m, have been hypothesized to possibly provide refuge for coral reefs in the future (Bongaerts et al., 2017; Bridge et al., 2014; Neal et al., 2014; Riegl & Piller, 2003; Shlesinger et al., 2018), but have recently been shown to be ecologically distinct (Rocha et al., 2018). These factors motivate the need for new methods to assess coral stressors at each depth zone independently.

Warm conditions that may lead to thermal stress and coral bleaching currently are forecast using SST values derived from satellite observations (Scott F. Heron et al., 2016; Liu et al., 2014; McClanahan et al., 2007). Elevated SSTs have been shown to be predictive of coral bleaching for shallow fore-reef corals (Couch et al., 2017; Eakin et al., 2010; Glynn & D'croz, 1990; Liu et al., 2014; McClanahan et al., 2007). At the same time, quantifying accurate bleaching thresholds for corals between 10-30 m has been limited and assessments of thermal stress on mesophotic coral reefs have only been done in a few studies (Bruno et al., 2001; Nir et al., 2014). This is primarily due to the lack of sustained temperature records at depths > 10-30 m and inconsistent surveying of bleaching events at depths exceeding 20 m (Bak et al., 2005). Depth has been recently shown to be a relevant parameter is assessing coral bleaching (Couch et al., 2017, p. 200; Safaie et al., 2018), but in the context of other environmental and ecological factors. We propose that the vertical dimension, something not captured in SST measurements, is critical when developing indicators of thermal stress as temperature variance is observed to increase closer to the thermocline (Bak et al., 2005; Wolanski et al., 2004). Sea level anomaly (SLA) is a relevant

observation that facilitates the prediction of temperatures starting at depths of 20-30 m, typically below the upper mixed layer (UML), for which SST is a poor proxy. A major part of the coral biomass exists below the base of the UML, denoted as the mixed layer depth (MLD), in the tropical Pacific (Bridge et al., 2013). The depth of isotherms below the MLD and SLA have been shown to be related in the tropical Pacific (Chaen & Wyrtki, 1981; Rebert et al., 1985), but the impact of isotherm displacements on the thermal structure at a tropical fore-reef system has not been documented on the time scales considered here due to a lack of in-situ observations.

The Republic of Palau, an island nation in the tropical western Pacific (Figure 1.S1.a), has a high diversity of marine habitats with exceptional coral reefs (Colin, 2009). Coral bleaching events have occurred in Palau with the largest on record concurrent with the 1998 La Niña (Bruno et al., 2001; Colin, 2009; Golbuu et al., 2007) with a lesser bleaching event on Palau's lagoons/outer slopes in 2010 (van Woesik et al., 2012). Bleaching in the mesophotic zone during the 1998 event was qualitatively observed down to 60 m (Bruno et al., 2001; Colin, 2009). Baker et al. (2016, p. 20) documented bleaching during the 2010 El Niño-Southern Oscillation (ENSO) event in Palau. Qualitative examples of both shallow, depths < 30 m, and mesophotic, depths 30-150 m, corals bleached during the 2010 event are shown in Figure 1.1.c and d, respectively. During July 2014 there was some bleaching in shallow, depths 2-10 m, lagoon corals (Colin, personal observation). The summer of 2016 saw the initiation of minor bleaching on both the fore-reefs and in the lagoons (Colin, personal observation). Impacted coral species during the 2014 and 2016 events are listed in the Supplemental Information (SI) (Text S1). High bleaching occurrence at all depths where reefs occur during the 1998 event motivated a long-term temperature monitoring program by the Coral Reef Research Foundation (CRRF) using vertical arrays of thermographs. Program data from Short Drop Off, Ulong Rock, and West Channel (Table 1.S1 and Figure 1.S1.c-

e, respectively), provide a near two-decade record of the vertical temperature structure affecting Palau's fore-reefs.

There are two main objectives of this study. First, to assess the ability of SLA, coupled with SST and observed fore-reef temperature, to reconstruct fore-reef temperature records. Second, to apply DHW at a range of depths in the upper water column and adjust the thermal stress metric to account for increased temperature variance in depth.

1.2 Methods

1.2.1 In-situ observations and gridded products

In-situ temperature at the seafloor was collected by CRRF at 17 stations in three locations around Palau at depths ranging from 2-90 m (Table 1.S1). Sampling intervals ranged from 30 seconds to 30 minutes. The observational campaign began in 2000 and is ongoing at the time of publication. Both daytime and nighttime records were used. A detailed description of the in-situ data is available in the SI (Text 1.S2, Table 1.S1).

SST at Palau was specified using the NOAA Coral Reef Watch (CRW) CoralTemp 5 km product (https://coralreefwatch.noaa.gov/satellite/coraltemp.php). SST time series were selected at the grid point closest to each observation station locations (Table 1.S1) (S F Heron et al., 2014, 2015; Liu et al., 2017). The SST product extends from 1985 to present. This product uses nighttime retrievals only from 2002 onwards and is available as a part of CRW 5km product that currently goes from 2013-present for the Palau Virtual Station (https://coralreefwatch.noaa.gov/vs/data/palau.txt). The relevant climatological values used in this work were obtained from this Virtual Station output. Regional SST maps were constructed from the NOAA OI SST V2 High Resolution Dataset due to ease of data access for the entire Pacific

(https://www.esrl.noaa.gov/psd/data/gridded/data.noaa.oisst.v2.highres.html) (Reynolds et al., 2007). Daily averages were obtained on a 0.25° x 0.25° global grid.

Daily tide gauge records were obtained from the Malakal Harbor station for 1970 through 2017 from the University of Hawaii Sea Level Center (http://uhslc.soest.hawaii.edu/data/) (Caldwell et al., 2017). Regional sea level was specified using the global ocean gridded sea level anomaly L4 output, 0.25° x 0.25° resolution, from Copernicus Marine Environment Monitoring Service (CMEMS) (marine.copernicus.eu/services-portfolio/access-to-products/). NCEP surface wind records (Kalnay et al., 1996) on a 0.25° x 0.25° global grid from 2000 to 2017 were obtained (https://www.esrl.noaa.gov/psd/data/gridded/data.ncep.reanalysis.html).

1.2.2 Filtering and the Oceanic Niño Index

Weekly averages were constructed for all data records to examine sub-inertial variability. The local inertial period is roughly 4 days. Partitioning of the data into ENSO phases was done by finding concurrent time steps when the Oceanic Niño Index (ONI) was greater than or equal to 0.5 (El Niño) or less than or equal to -0.5 (La Niña).

1.2.3 Reconstructing temperature using regression techniques

A multiple linear regression (MLR) analysis (Chatterjee & Hadi, 1986) was used to estimate in-situ temperature based on SST (CoralTemp SST) and SLA (Malakal tide gauge). SLA^2 was included as an MLR input to account for a nonlinear relationship between SLA and observed temperatures at some depth ranges (Figure 1.1.e). The regression model, applied at each sensor depth, z,

$$T(z) = a(z)\,SST + b(z)\,SLA^2 + c(z)\,SLA + d(z) \quad (1)$$

was used to reconstruct the upper ocean temperature profiles between 1985-2017. Code for implementing this methodology is available in the SI and can be accessed with accompanying example files at https://github.com/tschramek/ThermalStress.

1.2.4 Determining thermal stress – Degree Heating Weeks

Degree heating weeks (DHW) is a measure of the sustained thermal stress experienced by coral communities (Liu et al., 2014; Strong et al., 2004). DHW is the sum of thermal anomalies (Hotspots) that exceed a prescribed threshold accumulated during a 12-week running window (Strong et al., 2004). Coral bleaching is known to occur when SSTs exceed 1°C above the maximum monthly mean (MMM) temperature (Glynn & D'croz, 1990); hence MMM+1°C is the typical threshold used for the DHW calculation, or the bleaching threshold (Berkelmans & Willis, 1999).

To evaluate the potential thermal stress at depth, we considered three measures of DHW. The first is the traditional method based on when SST exceeds the bleaching threshold, which is computed using MMM at the sea surface, at z = 0, determined from SST,

$$SST > MMM(0) + 1°C. \quad (2)$$

The second uses in-situ temperature at each depth from the MLR reconstructions, with the bleaching threshold determined from SST,

$$T(z) > MMM(0) + 1°C. \quad (3)$$

This method assumes that thermal stress tolerances appropriate for the sea surface applies at all depths. Lastly, we adjust the bleaching threshold with depth to account for changes in the mean and variable temperature through the water column. A scaled version of the bleaching threshold was computed as,

$$T(z) > MMM(z) + 1°\mathrm{C}\frac{std\big(T(z)\big)}{std(SST)}. \quad (4)$$

Code for computing DHW has been provided in the SI and can be accessed with example data at https://github.com/tschramek/ThermalStress. MMM(z) were computed using the temperature reconstructions over the same base period (1985-2012) as the CRW supplied MMM computed from CoralTemp SSTs, noted above as MMM(0), for Palau (https://coralreefwatch.noaa.gov/vs/data/palau.txt).

1.3 Results

Surface Changes in temperature structure with SLA are illustrated for different phases of ENSO, when SLAs range from high (La Niña) to low (El Niño) in Palau (Figure 1.1.a,b). During La Niña conditions, the mixed layer is deep (greater than 35 m) with a weaker temperature gradient in the thermocline than during neutral ENSO phases (Baker et al., 2016). During El Niños, the mixed layer is shallow (15 m) with weak temperature gradients to ~35 m depth, and strong gradients below ~35 m. In general, as sea level rises/falls, the thermocline deepens/shoals, with UML temperatures tracking SST.

Binning the temperature data by SST (Figure 1.S2.a) and SLA (Figure 1.S2.b) shows how the vertical temperature gradient varies with each variable. SST represents temperature in the UML, SLA captures temperature variability below the MLD. Binning of temperature observations by SST yields distinct temperature profiles with constant temperatures in depth to the MLD (Figure 1.S2.a). At three sites, small differences exist between the in-situ temperature at 2 m depth and the CRW CoralTemp 5km SST product (Figure 1.S3.a-c). Influences from the lagoon systems, be it rainfall runoff, evaporation in the lagoon system resulting in increased salinity, and the

position of the thermographs on the top of barrier reefs offshore of the main island surface expression, as seen from Google Earth satellite imagery (Figure 1.S1.c-e), could be some of drivers of the differences between the near surface (depths < 10 m) stations.

The MLR analysis yields an estimate of temperature at each thermograph station that agrees remarkably well with the observed temperatures (Figure 1.1.f & g, Figure 1.S4.a-c). The MLR accounts for a significant fraction of temperature variability across depths and study sites (Figure 1.S4.a-c) with depth-averaged R^2 values of 0.88, 0.89 and 0.90 at Short Drop off (Figure 1.S1.c), Ulong Rock (Figure 1.S1.d) and West Channel (Figure 1.S1.e), respectively. The MLR model captures the observed profile changes during different ENSO phases (Figure 1.1.a – dashed lines). As anticipated from Figure 1.S2, SST is the important MLR input at depths in the UML, and SLA becomes important below the MLD. SLA^2 can be important near the surface and well below the MLD where the relationship between in-situ temperature and SLA are not always linear (Figure 1.S4.a & b).

Using the MLR derived coefficients in eq. (1) (Figure 1.S4.d-f), temperature profiles are reconstructed (Figure 1.2.a) back to the first full year of the SST and SLA records (1985, Figure 1.2.b,c). Observations of temperature from 2017 were withheld from the MLR model training to validate the model showing good agreement with correlation coefficients between 0.83 and 0.95 for each respective depth, and a depth-average correlation of 0.90 (Figure 1.S5).

The temperature reconstruction shows the warmest events in the UML at Palau tend to occur during large La Niña conditions that follow moderate to large El Niños, such as during the summers of 1998, 2010, and 2016 following peak El Niño conditions in the preceding winter. The amplitude of the UML warm events tend to increase over the course of the record, reflecting the

trend in observed SST of 0.022°C/yr between 1985 and 2016 (Figure 1.2.c – thin black line). In addition to high SSTs, these warm events are characterized by downward thermocline displacements corresponding to high SLA conditions.

The warm conditions at Palau following peak El Niños are associated with wind variations north of the equator. SLA variations at Palau are partially driven by local winds and remote winds to the east of Palau. Regionally, the wind-driven response reflects the ENSO zonal dipole pattern, and a meridional dipole (Widlansky et al., 2014). SLA variations often reach Palau via westward propagation in the form of Rossby waves. To illustrate this phenomenon, as well as the abrupt warming following El Niños, we examine SST, SLA, and the MLR temperature time-depth variability for 2015-2016 (Figure 1.3). As the El Niño event weakens, SLA and the surface wind field show a rapid, Pacific wide change between February and June of 2016 (Figure 1.3.a-c) with the trade winds extending westward along with a positive SLA. As the wind-forced anomaly reaches Palau in March 2016, local SLA rises (Figure 1.3.g), the thermocline deepens and UML temperatures abruptly increase (Figure 1.3.h). The anomaly is present through the summer of 2016.

The ONI suggests that a weak La Niña followed the strong El Niño in 2015-16. Monthly averaged SST show high temperatures near Palau and a La Niña like anomaly by June 2016 (Figure 1.3.d-e). The maps emphasize that in addition to La Niña conditions, it is the narrow band of easterly wind anomalies around the latitude of Palau, which mark the end of strong El Niño events in the spring, that lead to the abrupt and long-lasting warming events at Palau.

Based on DHW values computed using SST, potential bleaching events occurred during 1998, 2010, 2014, and 2016 (Figure 1.4.a). Each event occurs after a moderate to large El Niño,

except 2014. Extensive bleaching occurred in Palau during the 1998 and 2010 events (Bruno et al., 2001; Golbuu et al., 2007; van Woesik et al., 2012) while minor bleaching occurred during 2014 and 2016 in shallow corals (Colin, personal observation, Text S1). Using the bleaching threshold based on SST, the DHW estimate shows that the warming events at the surface penetrate to 30 m or so, largely reflecting the isothermal conditions in the UML (Figure 1.4.b). Using the scaled bleaching threshold, we find elevated DHW vales extending deeper in the water column to ~50 m, such as during the 1998 La Niña event (Figure 1.4.c). The scaled bleaching thus increases the estimated thermal stress compared to the standard DHW estimate based on only SST (Figure 1.4.c).

1.4 Conclusion and Discussion

In summary, A unique set of long-term, in-situ temperature records from Palau provide an opportunity to derive a new empirical model of upper-ocean temperature variability at fore-reefs using SST and SLA time series. We hypothesize that this relationship could persist throughout the tropical Pacific where the thermocline depth is largely dependent on large scale wind driven flows (Widlansky et al., 2014), and SLA has already been shown to be an indicator of the 20°C isotherm depth (Rebert et al., 1985). This concept has been used to derive synthetic temperature profiles in the Atlantic based on satellite altimeter data (Carnes et al., 1990), and temperature and salinity profiles in large scale ocean models (Fox et al., 2002), adding credence to the hypothesis. We caution that the method does not account for salinity effects, and in particular upper ocean thermal structures associated with barrier layers, which are salinity driven temperature inversions in the tropical western Pacific (Bosc Christelle et al., 2009; Lukas & Lindstrom, 1991). When barrier layers are prevalent, SLA may not always accurately predict the temperature structure.

We conclude that DHW estimates based only on SST may not adequately account for prolonged warming at depth associated with high sea levels and downward thermocline displacements. We have attempted to adjust the bleaching condition with depth to account for observed temperature variations with depth; however further studies are needed to confirm that the depth-dependent bleaching threshold matches observed bleaching events below the upper mixed layer where multiple stressors may also play a role in bleaching (Harborne et al., 2017). As a case in point, coral bleaching in Palau was observed at 60 m depth during the 2010 warm event; however, our DHW estimates only show heightened thermal stress to about 30 m, even with the adjusted bleaching condition. Nevertheless, our findings highlight that mesophotic coral reefs are vulnerable to thermal stress and that these depth zones may not be a refugia.

High temporal resolution and long duration observations of temperature on Palau's fore-reef system provide insight into the depth variable structure of thermal stress, leading to a new variance-based approach for predicting thermal stress. Our methods here provide a new means of assessing thermal stress due to the depth dependent nature of temperature variance seen throughout the range of depths where corals exist in this tropical Pacific location.

1.5 Acknowledgements

This work was funded under two Office of Naval Research grants specifically under the Flow Encounter Abrupt Topography DRI. The authors have no competing financial interests to disclose. The authors would like to thank the staff at both the Coastal Research and Development Center at the Scripps Institution of Oceanography and the Coral Reef Research Foundation for making this work possible. Conversations with Megan Cimino, Sophia Merrifield, Mike Fox, and Travis Courtney significantly improved this work. Ganesh Gopalakrishnan and Bruce Cornuelle kindly provided NCEP wind records. Erick Geiger and William Skirving at NOAA's CRW

provided site specific CoralTemp SST output and insights on their methodologies. In-situ temperature records can be accessed from the Coral Reef Research Foundation's Water Temperature Catalog at http://wtc.coralreefpalau.org/. All three anonymous reviewers gave insightful comments that greatly improved the manuscript. Example code for implementing the methods presented can be found in the SI or at https://github.com/tschramek/ThermalStress.

Chapter 1 in full has been published in Geophysical Research Letters. The dissertation author was the primary investigator and author of this paper: Schramek, T. A., Colin, P. L., Merrifield, M. A., & Terrill, E. J. (2018). Depth-dependent thermal stress around corals in the tropical Pacific Ocean. Geophysical Research Letters, 45, doi:10.1029/2018GL078782.

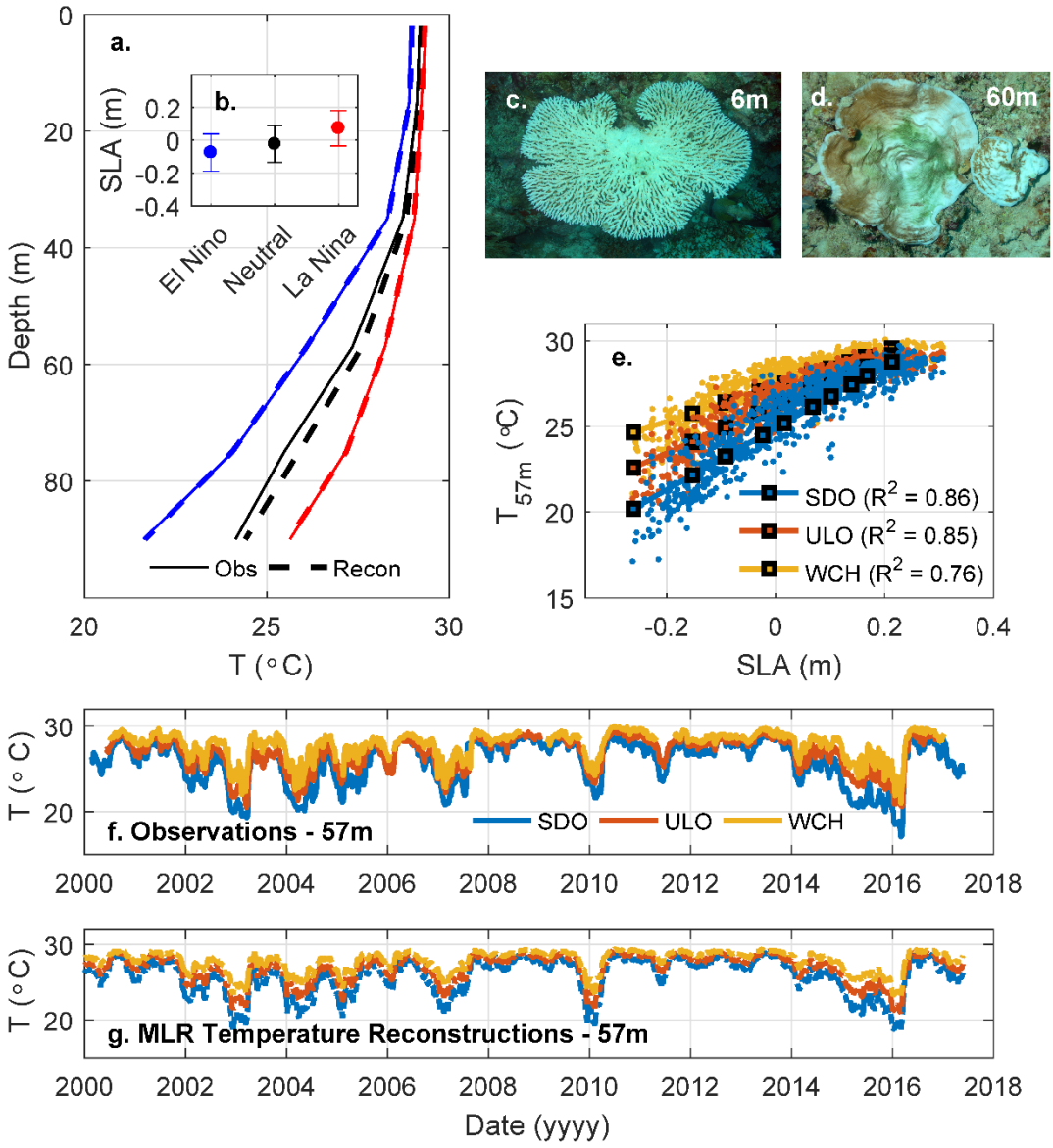

Figure 1.1: **a.** Mean temperature profiles from Palau (observed – solid lines, MLR modeled – dashed lines), at Short Drop Off (Figure 1.S1.c) on the East coast of Palau, during all El Niño (ONI >= 0.5 – red) and La Niña (ONI <= -0.5 – blue) events as well as a neutral condition (0.5 > ONI > -0.5 – black). **b.** Weekly SLA binned by ONI phase shows distinct regimes for the different phases of the ONI. Examples of coral bleached after the 2010 event from the **(c)** reef top (Acropora sp.) and **(d)** deeper reef slope (Pachyseris speciosa). **(e)** Linear regressions between SLA and the weekly-averaged temperature observations at 57 m from Short Drop Off (SDO, Figure 1.S1.c), Ulong Rock (ULO, Figure 1.S1.d), and West Channel (WCH, Figure 1.S1.e) with their corresponding R^2 values noted. **(g)** Weekly-averaged temperature observations from the same three locations as in (e) are shown. **(h)** MLR reconstructions (dashed lines) of each temperature record shown in (g) using tide gauge SLA and SST shown in Figure 1.3.b and c.

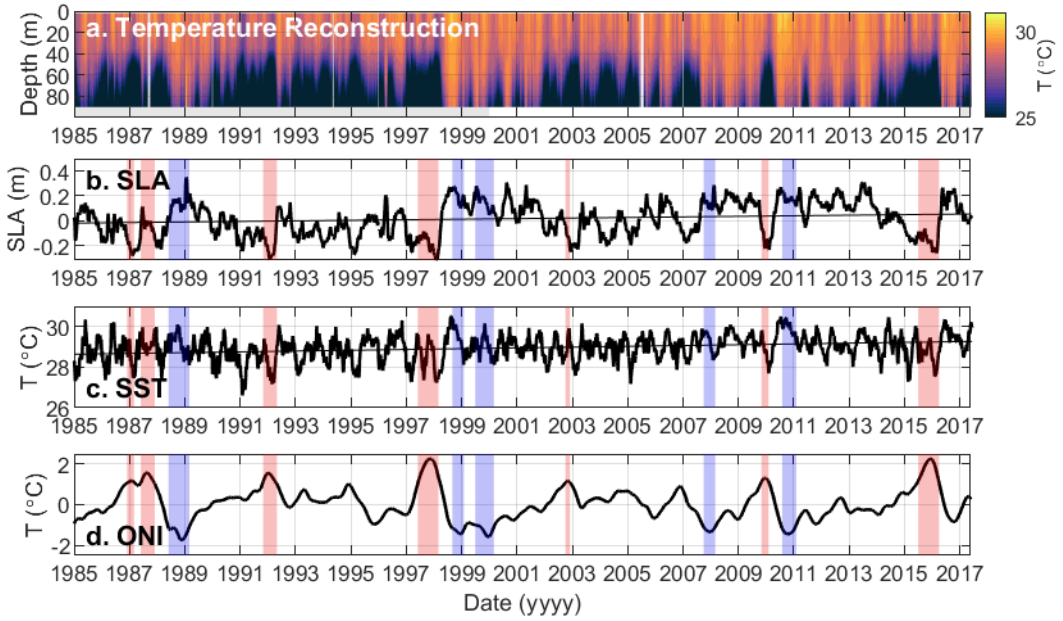

Figure 1.2: **a.** Weekly-averaged temperatures were reconstructed for Short Drop Off (Figure 1.S1.c), on the East coast of Palau, using multiple linear regressions for depths between 0 and 90 m and are shown for the time period of Jan 1985 to Jun 2017. Temperature observations from Short Drop Off between Jan 2000 and Dec 2016 (white background) were used to train the models. The depth-averaged R^2 was 0.88 for the reconstructions during that time period. The models were used to reconstruct temperatures (gray background) in depth as a hindcast (1985-2000) and a forecast (2017). **b.** Weekly-averaged sea level anomalies observed at the Malakal Harbor gauge (thick black line) are shown with an accompanying linear trend (thin black line). Red and blue patches indicate periods of at least moderate El Niño (ONI > 1) and La Niña (ONI < -1) events, respectively. **c.** SSTs at the closest grid point in the CoralTemp 5 km SST product to our observation station at Short Drop Off (thick black line) are shown with an accompanying linear trend (thin black line). **d.** The ONI is displayed between 1985 and 2017.

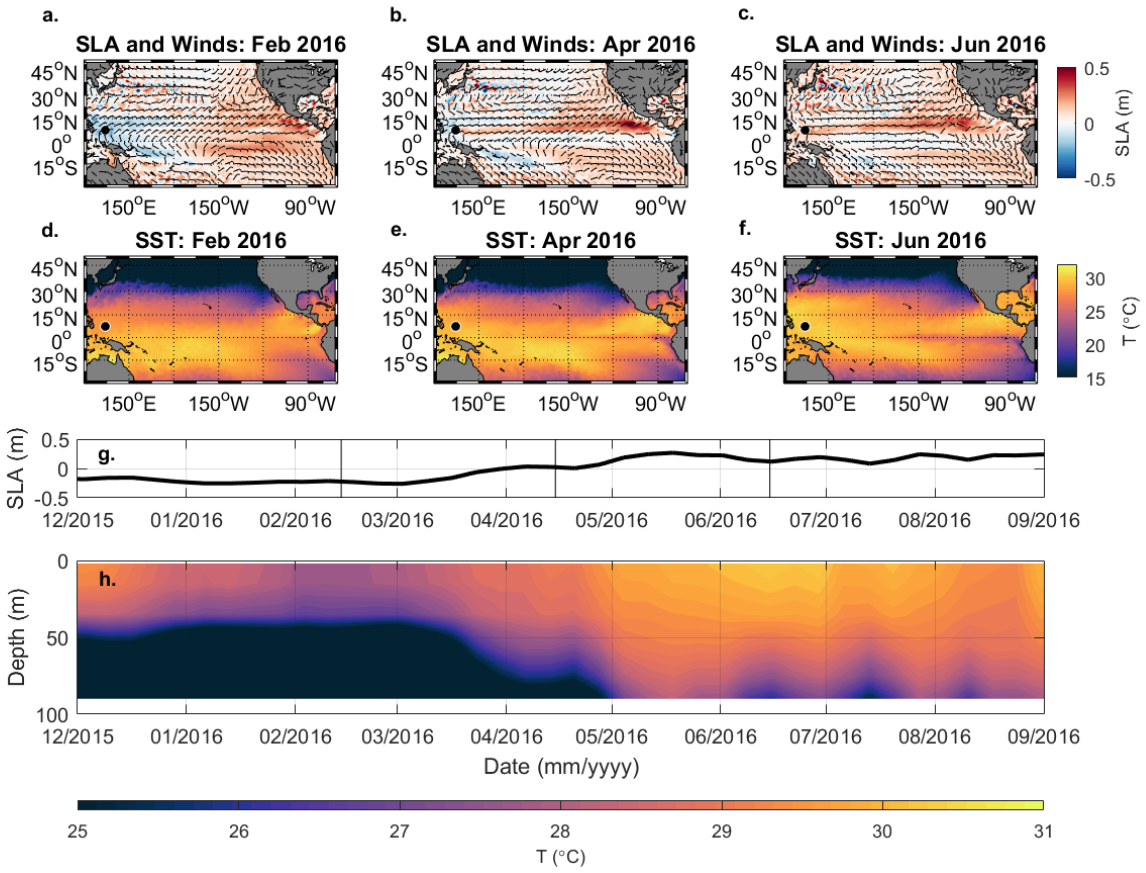

Figure 1.3: The spatial progression of the Rossby wave that shut down the 2015-2016 El Niño event can be seen in regional sea level anomaly (SLA), displayed as monthly averages, as the warm pool progressed from the central tropical Pacific in Feb 2016 (**a**) westward during the winter and spring of 2016 (**b**) terminating in the tropical western Pacific in the summer of 2016 (**c**). Palau is noted in a-c by a black dot in the Western Pacific at 7.5N, 134E. Surface level wind fields are overlaid on the SLA subplots (a-c). Monthly averaged SST from (**d**) February, (**e**) April, and (**f**) June show the Eastern Pacific and extra-tropical response to the decay of the 2015-2016 event, but no large change around Palau. Vertical black lines in (g) indicate the time stamps of the monthly averages (a-c, d-e). The local response at Palau to this event is evident in the weekly averaged SLA record (**g**), which is also reflected in reconstructed temperature time series from the east coast of Palau at Short Drop Off (**h**). Both (g) and (h) are subsets of the records shown in Figure 1.2.b and 2.a, respectively. The source data for the SLA (a-c) and SST (d-f) maps are CMEMS SLA 0.25° x 0.25° and NOAA OI SST 0.25° x 0.25°, respectively. Local SLA data (g) is from the NOAA Malakal tide gauge.

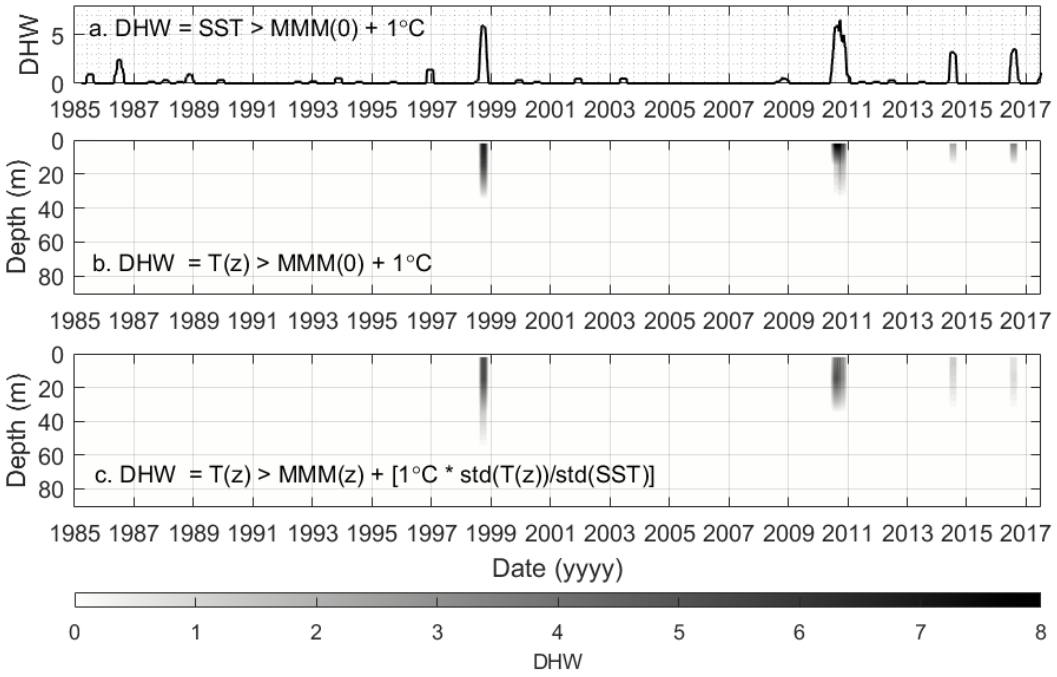

Figure 1.4: **a.** DHW was computed from the CRW CoralTemp SSTs supplied for Short Drop Off (black line). This matches the record of DHW supplied by CRW (not shown). **b.** DHW was computed for the temperature reconstructions between 0 and 90 m, which shows the temporal evolution of the depth variable thermal stress present through the records. DHWs were computed using the MMM supplied for CRW based off of the CoralTemp SST. DHW calculations for (a) and (b) use a bleaching thershold of 1°C. **c.** DHWs is shown between 0 and 90 m for the temperature records using the MMM computed for the temperature record at that depth. The bleaching threshold is now the standard deviation of the temperature time series at that depth multiplied by 1°C over the standard deviation of the SST. This give a proportional variance threshold, which the temperatures would have to exceed to be deemed a thermal stress. All relevant parameters for this figure are in Table 1.S2.

1.5 Appendix - Supplemental Information

Text 1.S1:

During July 2014 there was some bleaching in shallow (2 and 10 m depth) lagoon corals, particularly in head *Porites* spp., finger *Porites* spp., *Porites rus*, *Acropora* "*cerealias*", A. "*hyacinthus*" and *Psammocora* sp. (Colin, personal observation).

The summer of 2016 saw the initiation of minor bleaching on both the fore-reefs and lagoons in finger *Porites sp.*, head *Porites, Goniopora* spp., *Pachyseris* sp., *Archelia* sp., *Seratiopora* spp., *Fungiids, Pocillopora* spp. *Anacropora* sp., *Acropora* spp., *Acropora palifera, Asteropora*, *Pavona cactus* (Colin, personal observation).

Text 1.S2:

Four types of electronic thermographs (Onset Hobo H8 Pro, Onset U22-001, Sea-bird Scientific SBE 56 and RBR Solo) were used during the data collection and an accuracy of 0.1°C or better was obtained for all measurements. Starting in 2000 the non-waterproof H8 units, with resolution of 0.05°C or less and accuracy of 0.3°C (within the temperature range anticipated), were installed inside PVC plastic pressure proof housings measuring at 30 min intervals. A cabled external thermistor which rested against a stainless-steel plate (exposed to ambient temperatures) to reduce response time to temperature changes, while an internal thermistor (inside the thermograph itself) was occasionally used to validate external measurements. Units were calibrated pre- and post-deployment by immersing thermistors in a circulating water bath and comparing measurements against a NIST traceable mercury thermometer over 1-2 hours and a temperature range. Correction values determined for each instrument and applied to data. Their deployment was also described in Wolanski et al. (2004).

In 2010 Onset U22 thermographs recording at 30 min intervals were substituted for the H8 units. These had a resolution of 0.02°C, accuracy of 0.2°C and were similarly calibrated to insure final data of 0.1°C accuracy (most were already accurate within 0.1°C). At shallower depths (2 m, 11-15 m, 35 m) with little dynamic change, Onset U22 units have been used to the present.

In 2012 Sea-bird Scientific SBE 56 thermographs sampling at 1 min intervals were deployed at the deeper (57 and 90 m) stations, often with Onset U22 units alongside, with measurements averaged over 30 min for comparison to earlier data. In 2015 RBR Solo

thermographs were added to the inventory and the SBE and RBR units were used interchangeably at deeper stations, as they were within the 0.1°C accuracy requirement.

In-situ temperature records can be accessed from the Coral Reef Research Foundation's Water Temperature Catalog at http://wtc.coralreefpalau.org/.

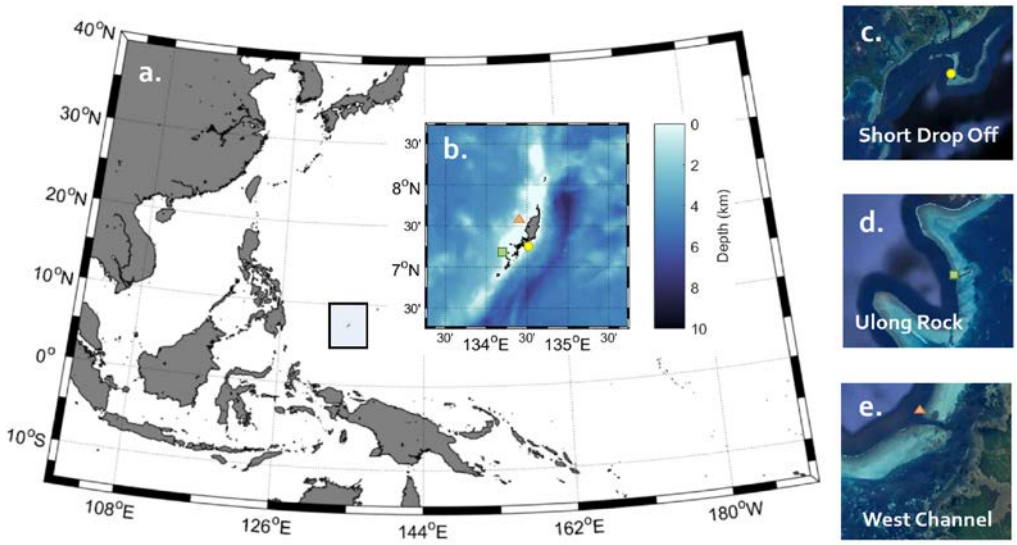

Figure 1.S1: **a.** Regional map showing the location of Palau in the western Tropical Pacific. **b.** A bathymetric map of Palau where the land is masked in gray and the locations of the three vertical temperature arrays, named Short Drop Off (SDO) (yellow circle square, Google Earth satellite image **c**), Ulong Channel (green square, satellite image **d**) and West Channel (orange triangle, satellite image **e**). Satellite images of each location (**c, d, e**) help to provide spatial context for the observations.

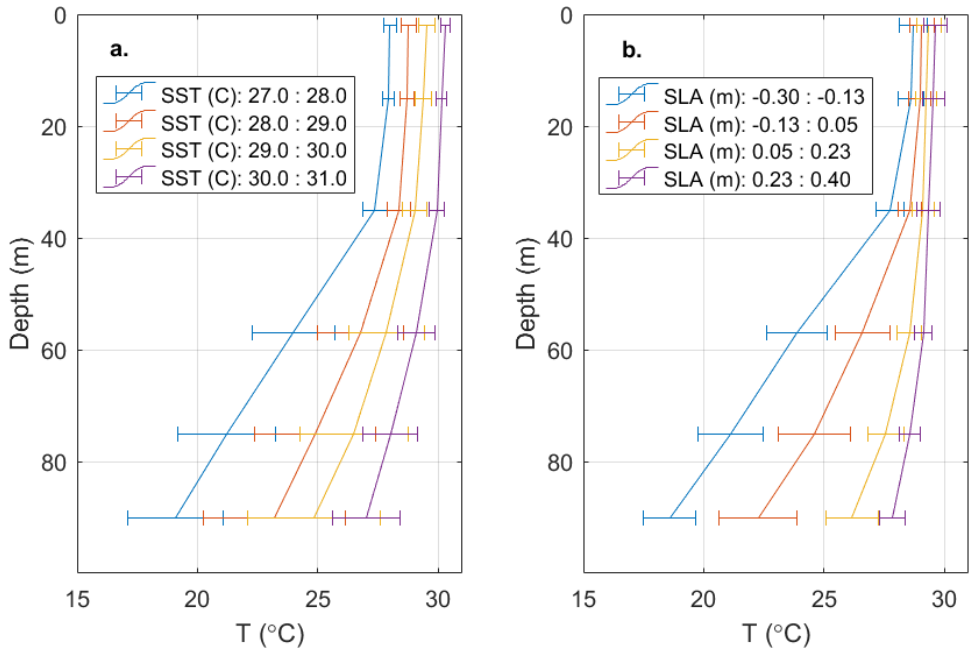

Figure 1.S2: Mean profiles of temperature records from Short Drop Off (Figure 1.S1.c), binned by (**a**) SST and (**b**) SLA.

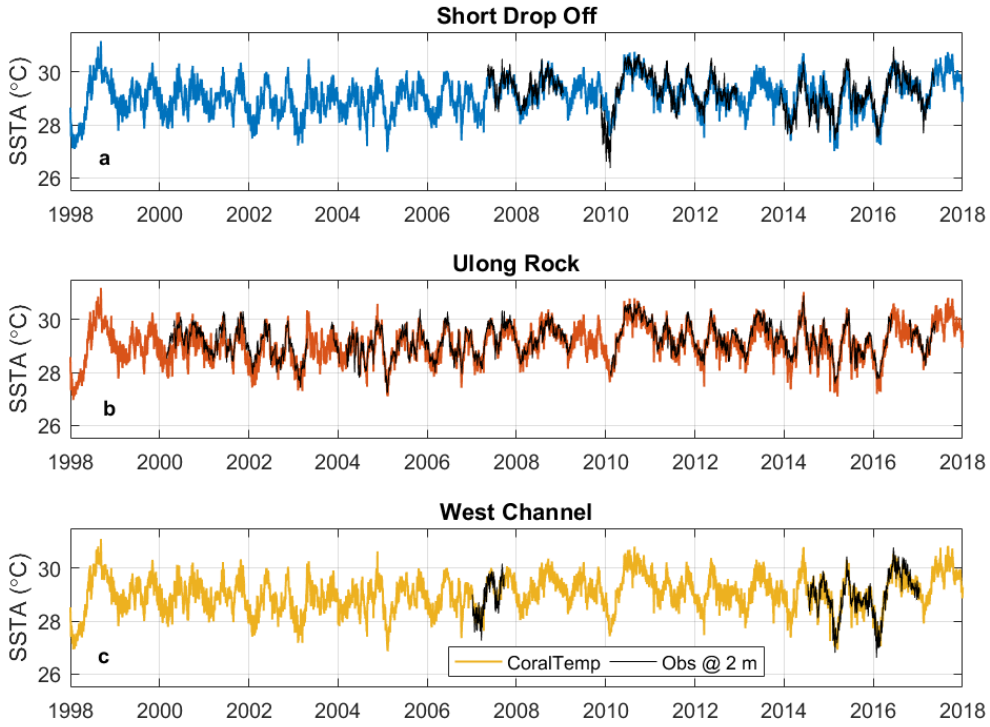

Figure 1.S3: NOAA Coral Reef Watch – CoralTemp 5km weekly averaged sea surface temperatures (a. Short Drop Off - blue, b. Ulong Rock - orange, c. West Channel - yellow) obtained from the NOAA Coral Reef Watch – CoralTemp product compared to the observations at 2 m depth (black) at each of the respective locations.

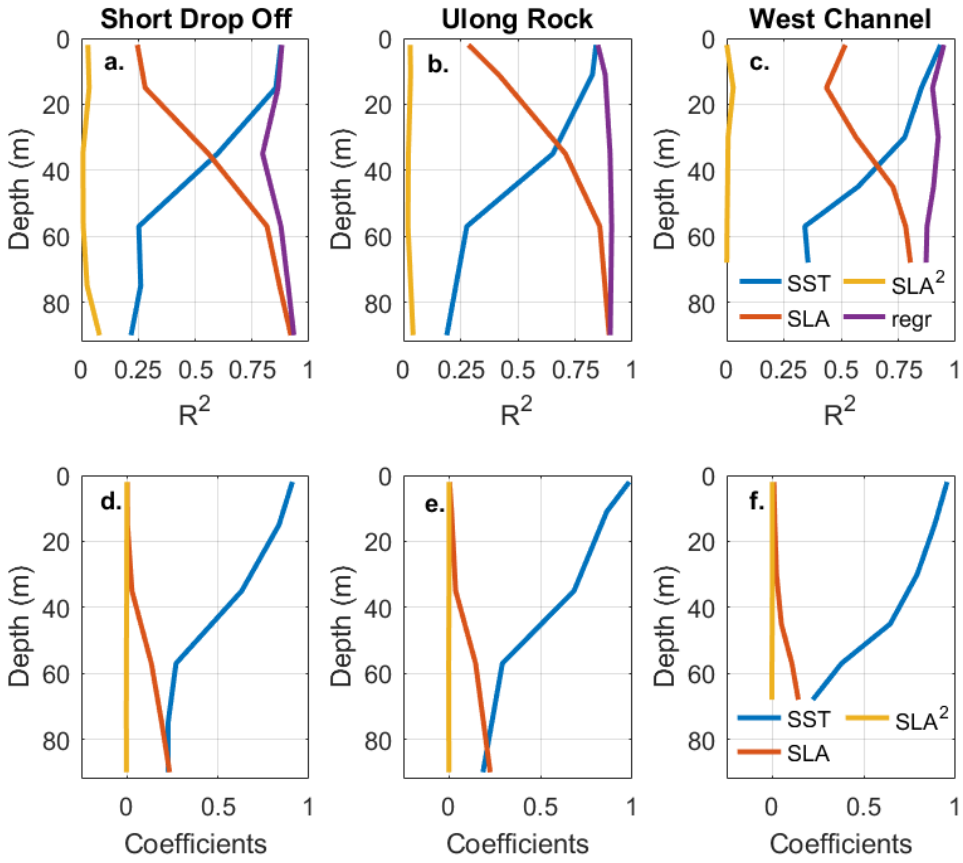

Figure 1.S4: The results of the multiple linear regression analysis at Short Drop Off (**a & d**), Ulong Rock (**b & e**), and West Channel (**c & f**) using weekly averaged data. The fraction of variance predicted by each input variable in the multiple linear regression (**a, b & c**) all exibit a depth dependent relationship, where the fraction of variance predicted by SST decrease in magnitude with depth (blue lines) and SLA increase with depth (orange lines). SLA^2 contains a small portion of the variance (yellow lines) and accounts for the nonlinearrity in the relationship, not accounted for by a linear regression. The values of the coefficients for the multiple regression model (**d, e & f**) is plotted in depth.

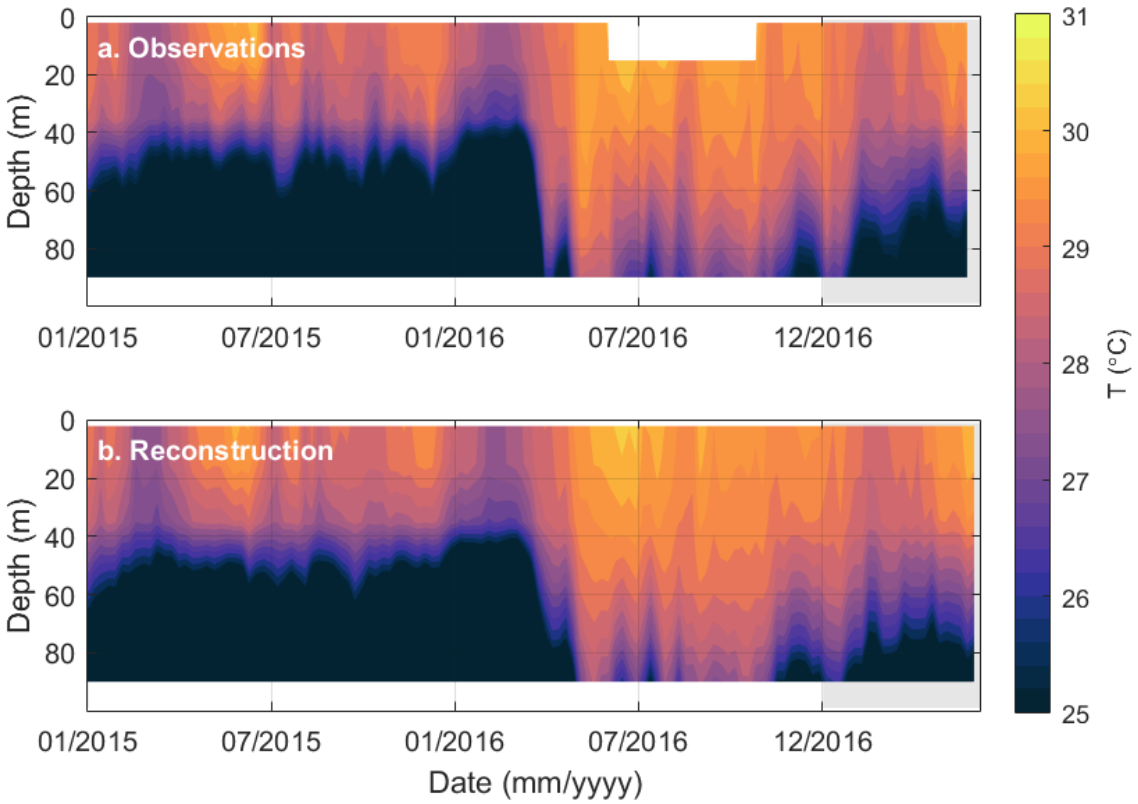

Figure 1.S5: **a.** Weekly-averaged in-situ temperature observations are shown between Jan 2015 and Jun 2017. Observations from 2017 (gray background) were withheld from the modeling training sets to allow for comparision. **b.** MLR modeled temperatures throughout the upper water column are shown for depths between 0 and 90 m and for the same time period as in **a**. The model outputs agree well with the observed temperature structure over the first 6 months of 2017 (gray background). Correlation coefficients between the temperature observations and temperature reconstructions range from 0.83 to 0.95 with a depth averaged value of 0.90 over this period.

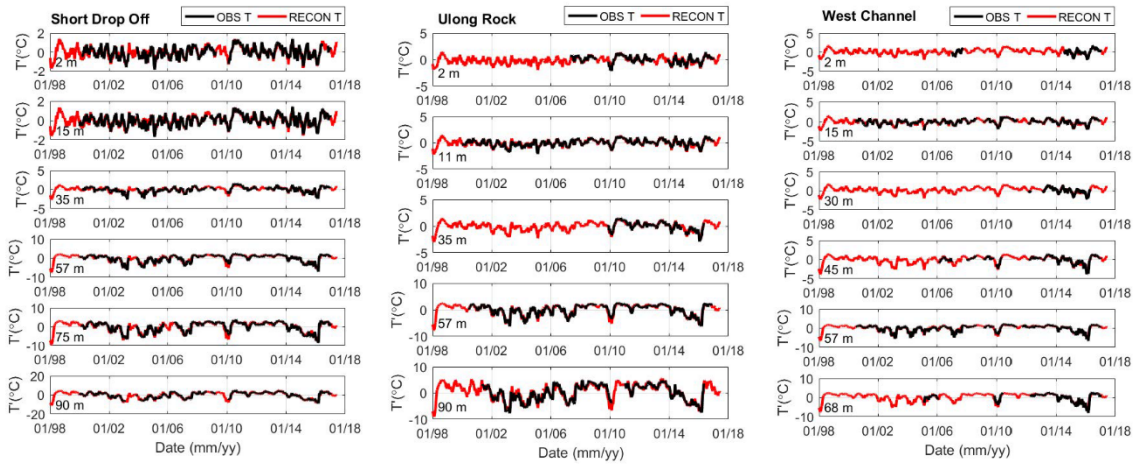

Figure 1.S6: Temperature records (black) and the corresponding reconstruction (red) using SLA and SST in the multiple linear regression techniques are displayed for the three sites, Short Drop Off (**a-f**), Ulong Rock (**e-i**) and West Channel (**j-o**).

Table 1.S1: Locations of each vertical array of thermographs mounted on the bottom around Palau and the associated depth stations at each location. The manufacturer, model, and sampling period are listed for each deployment time period and correspond to the information in Text S2.

ID	Latitude	Longitude	Depth (m)	Time Manufacturer Model Sampling	Time Manufacturer Model Sampling	Time Manufacturer Model Sampling	Time Manufacturer Model Sampling
Short Drop Off	7º 16.418' N	134º 31.440' E	2	2000-2010 Onset Hobo H8 Pro 30 min	2010-present Onset U22 30 min		
			15	2000-2010 Onset Hobo H8 Pro 30 min	2010-present Onset U22 30 min		
			35	2000-2010 Onset Hobo H8 Pro 30 min	2010-present Onset U22 30 min		
			57	2000-2010 Onset Hobo H8 Pro 30 min	2010-2012 Onset U22 30 min	2012-2015 Seabird Scientific SBE 56 1 min	2015-present RbR Inc. Solo t 1 min
			75	2000-2010 Onset Hobo H8 Pro 30 min	2010-2012 Onset U22 30 min	2012-present Seabird Scientific SBE 56 1 min	
			90	2000-2010 Onset Hobo H8 Pro 30 min	2010-2012 Onset U22 30 min	2012-2015 Seabird Scientific SBE 56 1 min	2015-present RbR Inc. Solo t 1 min
Ulong Rock	7º 17.453' N	134º 14.442' E	2	2000-2010 Onset Hobo H8 Pro 30 min	2010-present Onset U22 30 min		
			11	2000-2010 Onset Hobo H8 Pro 30 min	2010-present Onset U22 30 min		
			35	2000-2010 Onset Hobo H8 Pro 30 min	2010-present Onset U22 30 min		
			57	2000-2010 Onset Hobo H8 Pro 30 min	2010-2012 Onset U22 30 min	2012-2015 Seabird Scientific SBE 56 1 min	2015-present RbR Inc. Solo t 1 min
			90	2000-2010 Onset Hobo H8 Pro 30 min	2010-2012 Onset U22 30 min	2012-present Seabird Scientific SBE 56 1 min	
West Channel	7º 32.560' N	134º 28.059' E	2	2000-2010 Onset Hobo H8 Pro 30 min	2010-present Onset U22 30 min		
			15	2000-2010 Onset Hobo H8 Pro 30 min	2010-present Onset U22 30 min		
			30	2000-2010 Onset Hobo H8 Pro 30 min	2010-present Onset U22 30 min		
			45	2000-2010 Onset Hobo H8 Pro 30 min	2010-present Onset U22 30 min		
			57	2000-2010 Onset Hobo H8 Pro 30 min	2010-2012 Onset U22 30 min	2012-2015 Seabird Scientific SBE 56 1 min	2015-present RbR Inc. Solo t 1 min
			68	2000-2010 Onset Hobo H8 Pro 30 min	2010-2012 Onset U22 30 min	2012-present Seabird Scientific SBE 56 1 min	

Table 1.S2: Relevant parameters for the DHW computations in Figure 1.4. The MMM, Bleaching Threshold (BT), and overall Threshold were the same for both subplots 1 and 2. MMM were computed independently for each depth station using the temperature reconstructions. The degree offset (Deg Off) used in each bleaching threshold were also computed for each temperature reconstruction. Bleaching thresholds were the result of the MMM and Deg Off computed for each depth station.

Subplot	**Depth (m)**	**MMM**	**Deg Off**	**BT**
1,2	all	29.231	1	30.231
3	2	29.467	0.866	30.333
3	15	29.344	0.815	30.158
3	35	28.94	1.021	29.961
3	57	27.868	2.913	30.781
3	75	26.584	4.018	30.601
3	90	24.895	4.858	29.753

1.6 References

Bak, R. P. M., Nieuwland, G., & Meesters, E. H. (2005). Coral reef crisis in deep and shallow reefs: 30 years of constancy and change in reefs of Curaçao and Bonaire. *Coral Reefs*, *24*(3), 480–480. https://doi.org/10.1007/s00338-005-0060-y

Baker, E. K., Puglise, K. a., & Harris, P. T. (2016). Mesophotic Coral Ecosystems - A Lifeboat for Coral Reefs? In *The United Nations Environment Programme and GRID-Arendal Nairobi and Arendal* (Vol. 98, pp. 31–36).

Berkelmans, R., & Willis, B. L. (1999). Seasonal and local spatial patterns in the upper thermal limits of corals on the inshore Central Great Barrier Reef. *Coral Reefs*, *18*(3), 219–228. https://doi.org/10.1007/s003380050186

Bongaerts, P., Riginos, C., Brunner, R., Englebert, N., Smith, S. R., & Hoegh-Guldberg, O. (2017). Deep reefs are not universal refuges: Reseeding potential varies among coral species. *Science Advances*, *3*(2), e1602373. https://doi.org/10.1126/sciadv.1602373

Bridge, T. C., Hughes, T. P., Guinotte, J. M., & Bongaerts, P. (2013). Call to protect all coral reefs. *Nature Climate Change*, *3*(6), 528–530.

Bridge, T. C., Hoey, A. S., Campbell, S. J., Muttaqin, E., Rudi, E., Fadli, N., & Baird, A. H. (2014). Depth-dependent mortality of reef corals following a severe bleaching event: implications for thermal refuges and population recovery. *F1000Reseach*, *2*.

Bruno, J., Siddon, C., Witman, J., Colin, P., & Toscano, M. (2001). El Niño related coral bleaching in Palau, Western Caroline Islands. *Coral Reefs*, *20*(2), 127–136. https://doi.org/10.1007/s003380100151

Caldwell, P. C., Merrifield, M. A., & Thompson, P. R. (2017). Sea level measured by tide gauges from global oceans as part of the Joint Archive for Sea Level (JASL) from 1846-01-01 to 2015-07-31. *National Oceanographic Data Center, NOAA.* https://doi.org/10.7289/V5V40S7W

Chaen, M., & Wyrtki, K. (1981). The 20C isotherm depth and sea level in the western equatorial pacific. *Journal of the Oceanographical Society of Japan*, *37*(4), 198–200. https://doi.org/10.1007/BF02309057

Chatterjee, S., & Hadi, A. S. (1986). Influential Observations, High Leverage Points, and Outliers in Linear Regression. *Statistical Science*, *1*(3), 379–393.

Colin, P. L. (2009). *Marine environments of Palau*. Taiwan: Indo-Pacific Press. Retrieved from http://coralreefpalau.org/wp-content/uploads/2017/04/Colin-PL-2009-Marine-Environments-of-Palau.pdf

Couch, C. S., Burns, J. H. R., Liu, G., Steward, K., Gutlay, T. N., Kenyon, J., et al. (2017). Mass coral bleaching due to unprecedented marine heatwave in Papahānaumokuākea Marine National Monument (Northwestern Hawaiian Islands). *PLOS ONE*, *12*(9), e0185121. https://doi.org/10.1371/journal.pone.0185121

Donner, S. D. (2009). Coping with Commitment: Projected Thermal Stress on Coral Reefs under Different Future Scenarios. *PLoS ONE*, *4*(6), e5712. https://doi.org/10.1371/journal.pone.0005712

Eakin, C. M., Morgan, J. A., Heron, S. F., Smith, T. B., Liu, G., Alvarez-Filip, L., et al. (2010). Caribbean Corals in Crisis: Record Thermal Stress, Bleaching, and Mortality in 2005. *PLoS ONE*, *5*(11), e13969. https://doi.org/10.1371/journal.pone.0013969

Gleeson, M. W., & Strong, A. E. (1995). Applying MCSST to Coral Reef Bleaching. *Advances in Space Research*, *16*(10), 151–154. https://doi.org/10.1016/0273-1177(95)00396-V

Glynn, P. W. (1993). Coral reef bleaching: ecological perspectives. *Coral Reefs*, *12*(1), 1–17. https://doi.org/10.1007/BF00303779

Glynn, P. W., & D'croz, L. (1990). Experimental evidence for high temperature stress as the cause of El Nino-coincident coral mortality. *Coral Reefs*, *8*(4), 181–191.

Golbuu, Y., Victor, S., Penland, L., Idip, D., Emaurois, C., Okaji, K., et al. (2007). Palau's coral reefs show differential habitat recovery following the 1998-bleaching event. *Coral Reefs*, *26*(2), 319–332. https://doi.org/10.1007/s00338-007-0200-7

Heron, S F, Liu, G., Rauenzahn, J. L., Christensen, T. R. L., Skirving, W. J., Burgess, T. F. R., et al. (2014). Improvements to and continuity of operational global thermal stress monitoring for coral bleaching. *Journal of Operational Oceanography*, *7*(2), 3–11. https://doi.org/10.1080/1755876X.2014.11020154

Heron, S F, Liu, G., Eakin, C M, Skirving, W J, Muller-Karger, F. E., Vega-Rodriguez, M., et al. (2015). *Climatology development for NOAA Coral Reef Watch's 5-km product suite* (NOAA Technical Report NESDIS 145) (p.). College Park, MD: NOAA/NESDIS. https://doi.org/10.7289/V59C6VBS

Heron, Scott F., Johnston, L., Liu, G., Geiger, E. F., Maynard, J. A., De La Cour, J. L., et al. (2016). Validation of Reef-Scale Thermal Stress Satellite Products for Coral Bleaching Monitoring. *Remote Sensing*, *8*(1), 59. https://doi.org/10.3390/rs8010059

Hoegh-Guldberg, O. (1999). Climate change, coral bleaching and the future of the world's coral reefs. *Marine and Freshwater Research*, *50*(8), 839. https://doi.org/10.1071/MF99078

Hughes, T. P., Anderson, K. D., Connolly, S. R., Heron, S. F., Kerry, J. T., Lough, J. M., et al. (2018). Spatial and temporal patterns of mass bleaching of corals in the Anthropocene. *Science*, *359*(6371), 80–83.

Kahng, S. E., Garcia-Sais, J. R., Spalding, H. L., Brokovich, E., Wagner, D., Weil, E., et al. (2010). Community ecology of mesophotic coral reef ecosystems. *Coral Reefs*, *29*(2), 255–275. https://doi.org/10.1007/s00338-010-0593-6

Kalnay, E., Kanamitsu, M., Kistler, R., Collins, W., Deaven, D., Gandin, L., et al. (1996). The NCEP/NCAR 40-year reanalysis project. *Bulletin of the American Meteorological Society*, *77*(3), 437–471.

Langlais, C. E., Lenton, A., Heron, S. F., Evenhuis, C., Sen Gupta, A., Brown, J. N., & Kuchinke, M. (2017). Coral bleaching pathways under the control of regional temperature variability. *Nature Climate Change*, *7*(11), 839–844. https://doi.org/10.1038/nclimate3399

Lesser, M. P., Slattery, M., & Leichter, J. J. (2009). Ecology of mesophotic coral reefs. *Journal of Experimental Marine Biology and Ecology*, *375*(1–2), 1–8. https://doi.org/10.1016/j.jembe.2009.05.009

Liu, G., Strong, A. E., Skirving, W., & Arzayus, L. F. (2006). Overview of NOAA coral reef watch program's near-real time satellite global coral bleaching monitoring activities. In *Proc 10th Int Coral Reef Symp* (Vol. 1, pp. 1783–1793).

Liu, G., Heron, S., Eakin, C., Muller-Karger, F., Vega-Rodriguez, M., Guild, L., et al. (2014). Reef-Scale Thermal Stress Monitoring of Coral Ecosystems: New 5-km Global Products from NOAA Coral Reef Watch. *Remote Sensing*, *6*(11), 11579–11606. https://doi.org/10.3390/rs61111579

Liu, G., Skirving, W. J., Geiger, E. F., & La, J. L. D. (2017). NOAA Coral Reef Watch's 5km Satellite Coral Bleaching Heat Stress Monitoring Product Suite Version 3 and Four-Month Outlook Version 4, *32*(1), 7.

McClanahan, T., Ateweberhan, M., Graham, N., Wilson, S., Sebastián, C., Guillaume, M., & Bruggemann, J. (2007). Western Indian Ocean coral communities: bleaching responses and susceptibility to extinction. *Marine Ecology Progress Series*, *337*, 1–13. https://doi.org/10.3354/meps337001

Neal, B. P., Condit, C., Liu, G., dos Santos, S., Kahru, M., Mitchell, B. G., & Kline, D. I. (2014). When depth is no refuge: cumulative thermal stress increases with depth in Bocas del Toro, Panama. *Coral Reefs*, *33*(1), 193–205. https://doi.org/10.1007/s00338-013-1081-6

Nir, O., Gruber, D. F., Shemesh, E., Glasser, E., & Tchernov, D. (2014). Seasonal Mesophotic Coral Bleaching of Stylophora pistillata in the Northern Red Sea. *PLOS ONE*, *9*(1), e84968. https://doi.org/10.1371/journal.pone.0084968

Rebert, J. P., Donguy, J. R., Eldin, G., & Wyrtki, K. (1985). Relations between sea level, thermocline depth, heat content, and dynamic height in the tropical Pacific Ocean. *Journal of Geophysical Research*, *90*(C6), 11719. https://doi.org/10.1029/JC090iC06p11719

Reynolds, R. W., Smith, T. M., Liu, C., Chelton, D. B., Casey, K. S., & Schlax, M. G. (2007). Daily High-Resolution-Blended Analyses for Sea Surface Temperature. *Journal of Climate*, *20*(22), 5473–5496. https://doi.org/10.1175/2007JCLI1824.1

Riegl, B., & Piller, W. E. (2003). Possible refugia for reefs in times of environmental stress. *International Journal of Earth Sciences*, *92*(4), 520–531. https://doi.org/10.1007/s00531-003-0328-9

Rocha, L. A., Pinheiro, H. T., Shepherd, B., Papastamatiou, Y. P., Luiz, O. J., Pyle, R. L., & Bongaerts, P. (2018). Mesophotic coral ecosystems are threatened and ecologically distinct from shallow water reefs. *Science*, *361*(6399), 281–284. https://doi.org/10.1126/science.aaq1614

Safaie, A., Silbiger, N. J., McClanahan, T. R., Pawlak, G., Barshis, D. J., Hench, J. L., et al. (2018). High frequency temperature variability reduces the risk of coral bleaching. *Nature Communications*, *9*(1). https://doi.org/10.1038/s41467-018-04074-2

Shlesinger, T., Grinblat, M., Rapuano, H., Amit, T., & Loya, Y. (2018). Can mesophotic reefs replenish shallow reefs? Reduced coral reproductive performance casts a doubt. *Ecology*, *99*(2), 421–437. https://doi.org/10.1002/ecy.2098

Strong, A. E., Liu, G., Meyer, J., Hendee, J. C., & Sasko, D. (2004). Coral reef watch 2002. *Bulletin of Marine Science*, *75*(2), 259–268.

Wellington, G. M., Glynn, P. W., Strong, A. E., Navarrete, S. A., Wieters, E., & Hubbard, D. (2001). Crisis on coral reefs linked to climate change. *Eos, Transactions American Geophysical Union*, *82*(1), 1–5.

van Woesik, R., Houk, P., Isechal, A. L., Idechong, J. W., Victor, S., & Golbuu, Y. (2012). Climate-change refugia in the sheltered bays of Palau: analogs of future reefs. *Ecology and Evolution*, *2*(10), 2474–2484. https://doi.org/10.1002/ece3.363

Wolanski, E., Colin, P., Naithani, J., Deleersnijder, E., & Golbuu, Y. (2004). Large amplitude, leaky, island-generated, internal waves around Palau, Micronesia. *Estuarine, Coastal and Shelf Science*, *60*(4), 705–716. https://doi.org/10.1016/j.ecss.2004.03.009

Chapter 2:

Coastally Trapped Waves around Palau

Observations from around the island group of Palau, located in the tropical Western Pacific, exhibit a persistent presence of baroclinic coastally trapped waves. The signals are found in records of temperature that were sustained on the fore-reef for seven months, May to December 2013, with the strongest signal from Typhoon Haiyan which passed over Kayangel Atoll, along with the northern most Palauan islands, in November of 2013. This strong forcing led to a large near- and sub-inertial response both in temperature and nearshore currents. We use semi-analytical models, such as the vertical structure equation and Brink and Chapman's (1985) model, to compute propagating modes for this oceanographic region to provide a benchmark for comparison with the observations. These models provided a framework to account for the influence of local stratification, topography and the local Coriolis parameter on the wave guide around Palau. We found the maximum vertical displacements over the course of a 22-day period that included Typhoon Haiyan were 35.5 m and 45.7 m at the 57 m and 90 m isobaths, respectively, where temperatures ranged by 4.1°C and 9.0°C over that same period at those respective depths. The apparent omnipresence of coastally trapped waves throughout the observational window provide a regular cycling of temperature at depth, potentially conditioning benthic communities living on the outer reef slope to temperature swings.

2.1 Introduction

The physical framework for understanding Coastally Trapped Waves (CTWs) has advanced from simplified straight coast geometries to regions with complex bathymetry and curved coastlines. CTWs propagate with the coast to the right (left) in the Northern (Southern)

hemisphere, rotating around basins in a cyclonic direction, and around islands in an anti-cyclonic direction(K H Brink, 1991). The special case of CTWs around islands was first approached with theory from Longuet-Higgins (1967, 1969) followed by observational studies conducted around Bermuda by Hogg (1980) and Brink (1999) . Substantial effort has been focused on determining the physics of CTWs along the continental shelf (K H Brink, 1991; Buchwald & Adams, 1968; D C Chapman, 1983; John M Huthnance, 1975, 1978; L A Mysak, 1980). Extension of the theory to regions with nearshore trenches such as Japan and Peru has brought insight to regional conditions with steeper topographies or with small, opposing trench walls (Lawrence A Mysak et al., 1979). Narrow shelves have been approached as quasi-vertical walls and are dominated by Kelvin wave-like structure (J M Huthnance et al., 1986; Wang & Mooers, 1976). Semi-analytical models now exist that are capable of determining modal structure due to the influence of Coriolis, topography, and stratification while being able to account for curved coastlines of islands by employing radial geometries (K H Brink, 1999; Brink & Chapman, 1985). The slope of an island's bottom topography creates a semi-geostrophic balance where horizontal motions are constrained causing vertical displacements (K H Brink, 1991). Due to this, CTWs around islands should be clear in observations of water temperature along the coastline while the nearshore current response will be subdued in comparison to the offshore response maintaining the semi-geostrophic balance (K H Brink, 1991; Hogg, 1980).

There are a number of parameters that define the wave-guide which control the existence and type of CTW in a region. Static properties include the local topography and coastline shape as well as the latitude band. Typical continental shelf topographic profiles are shallow for an extended distance offshore with an abrupt steepening, called the shelf break. This shape is often modeled as an exponentially decaying offshore profile ending in a flat bottom ocean (Buchwald & Adams,

1968). Stratification and along-coast flow control the time-varying properties of the wave-guide. For example, the depth of the thermocline and where it interacts with the local offshore bathymetric profile can dictate the wave type.

Changes in the properties of the wave-guide, such as pycnocline depth, can dictate the wave types that are present. If the pycnocline consists of a sharp gradient and is deeper than the shelf break the major response in deep water will be equivalent to the motion along a steep wall and show characteristics of internal Kelvin waves (J M Huthnance et al., 1986; Wang & Mooers, 1976). Shelf or edge waves can be present in the shallow region of the shelf when the pycnocline is above the shelf break (David C Chapman, 1984). Variations in along-coast profiles, especially headlands, cause dissipation due to interaction between modes and radiation away from the land mass (Wilkin & Chapman, 1990).

Forcing of CTWs can be done by a variety of atmospheric and oceanographic phenomenon such as along-coast wind stress events (K H Brink, 1991) and equatorial Rossby or Kelvin waves radiating up the coast (Suginohara, 1981). While studies have examined typhoon-generated CTWs along continental shelves (Dukhovskoy et al., 2009; Kakinuma & Nakayama, 2007; Zamudio et al., 2002), there are few observations of these events around islands and those that do exist (Kakinuma & Nakayama, 2007) do not capture CTWs propagating around islands.

The physical oceanographic environment of the outer-reef slope around Palau has gone largely uncharacterized outside of one study (Wolanski et al., 2012). The purpose of this study is to better understand a driver of temperature cycling for the benthic slope communities of Palau and the influence of tropical systems on the nearshore oceanographic environments around an island group. Here, we assess the CTW activity along the barrier reef of Palau's main island group,

with the aim to characterize both their generation and propagation using an observational array deployed around the barrier reef.

The main island group of Palau is a single island shelf with steep barrier and fringing reefs around its perimeter (Colin, 2009). The Palau Trench sits directly off of the east coast of Palau and has depths exceeding 8000 m (Figure 2.1) while other coasts have depths of a few thousand m within 5-10 km of the reef. The meridional length scale of the main island group is ~160 km, if Velasco Reef in the north is considered, and has a total circumference along the fore-reef of ~350 km.

The atmospheric conditions around Palau are dominated by the southwesterly monsoon through the summer and fall and the trade winds in the winter and spring (Kubota et al., 2005). Typhoon Haiyan passed over Palau (6 - 7 November 2013) during the observational window of this experiment with maximum sustained winds reported by the Joint Typhoon Warning Center (JTWC) of 87.5 m/s. The effects of the storm altered the water temperature profile in the region for at least 3 weeks after the storm passed. This strong forcing provided ample forcing conditions for the generation of coastal trapped waves. This event was compared to a multi-month window during the monsoonal season, considered here to be representative of the background state.

2.2 Methods

2.2.1 Observational array

An array of 17 in-situ sensors were maintained as a part of a campaign to observe the variability in the coastal environment of Palau. The array consisted of recordings thermographs and bottom pressure sensors, supported with a current meter and meteorological sensors. The suite

of instruments were deployed May to December 2013 and positions can be seen in Figure 2.1 with depths indicated in Table 2.1. All reported times are in UTC.

Nearshore flows were observed by a single bottom mounted, upward-looking 1 MHz Nortek AWAC Acoustic Doppler Current Profiler (Boston, MA) deployed on the east coast of Palau in 15 m of water on the edge of the fore-reef (Figure 2.1). The ADCP was configured with 1 m bins and recorded 12 minute ensembles to provide a measurement uncertainty of approximately 1 cm/s. Five Richard Brancker & Associates (Ottawa, Canada) Duo pressure sensors were mounted on the seafloor at depths ranging from 2 m to 17 m around the barrier reef in the southern half of Palau. These pressure sensors recorded data for 17 minutes every hour and had a sampling frequency of 1 Hz (Figure 2.1 and Table 2.1). This scheme sampled rapidly enough for the processing of surface gravity wave statistics, tides, and mean bottom pressure disturbances. The RBR Duos' thermographs have an accuracy of ±0.002°C and pressure sensors have an accuracy of ±2.5 cm. An array of ten Seabird Scientific (Seattle, WA) SBE56 thermographs was deployed on the seafloor around the island group at the nominal 57 m and 90 m isobaths and were configured to sample at 30 minute intervals (Figure 2.1). SBE56 thermographs have an accuracy of ± 0.002 °C with a response time of 5 minutes. The 57 m and 90 m isobaths were chosen because previous observations showed a large amount of variance and it is feasible for suitably equipped and trained diver deployments (Wolanski et al., 2004). A Scripps Institution of Oceanography-built meteorological station configured with a Vaisala WXT520 (Vantaa, Finland) weather sensor was stationed on a small island on the western barrier reef (Figure 2.1). The collected data are reported hourly to the Coastal Research and Development Center at the Scripps Institution of Oceanography using Iridium.

2.2.2 Statistical Techniques

A variety of filters were applied to the data to extract the ocean response at the CTW bands of interest. Subtidal signals were extracted using a Godin filter (Godin, 1972) consisting of three sequentially applied moving averages of 24, 24, and 25 hours. This method removes the variability that persists through a single 25 hour box car filter within dominant tidal bands (Foreman et al., 1995). The inertial period ranges between 3.6 – 4.1 days within the meridional extent of Palau, ranging (7°N to 8°N). A 4th-order Butterworth band-pass filter was used to examine signals with periods of 3.5 – 20 days. This acts as a subtidal low pass filter and removes longer term variability present in the temperature records, which are not of interest in this study. Time-lagged cross-correlation was used to determine the time delay between signals observed at two fixed stations allowing for the estimation of these signals propagation speeds.

We also examined these data in the frequency domain to see how individual events excite the wave-guide in this space. Rotary spectra were computed on ADCP records of vector currents using the method developed by Gonella (1972). The Matlab toolbox T_Tide (Pawlowicz et al., 2002) was used to remove the tidal signal from the pressure gauges so the Typhoon's effect on water level could be determined.

2.2.3 Modeling the Wave-Guide

The one-dimensional vertical structure equation (VSE) (Pedlosky, 1982), also known as the vertical eigenvalue problem (Cushman-Roisin & Beckers, 2010), was used as a simple framework to assess the role of stratification on the modal response and phase speeds of the baroclinic variability of the ocean region around the Palau island group. (Chelton et al., 1998) and (Picaut & Sombardier, 1993) applied variants of the discretized VSE to determine the first baroclinic gravity wave speed and Rossby radii across the world's oceans and found Mode-1 phase

speeds of 2.8 m/s and 2.6 m/s respectively within the vicinity of Palau. This model assumes a flat bottom, free-wave case where the vertical and horizontal structure are separable. The formulation gives an eigenvalue problem that uses the N^2 profile to compute a set of eigenvalues (phase speeds) and eigenvectors (vertical mode shapes) corresponding to free waves. The rigid lid approximation constrains the free surface for this problem thus barotropic phase speed is not properly characterized. As it assumes no lateral boundaries, this simplified computation is used only for insight on the CTW modal response. Admittedly this model does not correctly capture the bathymetry around Palau that is obviously not perfectly vertical or homogenous along-shore. This simplified model is, however, a useful first-pass diagnostic in identifying CTWs (Kajiura, 1974; Kawabe, 1982).

Advancing beyond the VSE the role of topography and latitude band in CTWs have been accounted for in the two-dimensional model developed by (Kenneth H Brink & Chapman, 1985), henceforth BC85. BC85 can compute trapped frequencies for particular coastal geometries and physical conditions. This incorporation of a bathymetric profile with the potential for trapping differs substantially from the simplified flat bottom boundary condition used in the VSE. The model domain is considered to be bounded in x (across-shore) and z (depth). For this case, the boundary conditions consist of the rigid lid approximation at the surface, no flow through the bottom, no flow at the outer boundary and no flow normal to the coast. The model's cross-shore width was 150 km with a horizontal grid resolution of 1530.6 m and 30 vertical sigma-grid layers. The no flow boundary condition at the outer extent of the model domain was used to maintain generality for multiple regional circulation scenarios. The flow patterns in this region have been shown to have both seasonal and inter-annual variability (Heron et al., 2006; Hsin & Qiu, 2012; Jun et al., 2016). The model's predictions are spurious when ω, the frequency of the CTW,

approaches f, the inertial frequency, as it tends to find resonant conditions at f. BC85 recommends to trust results up to $\omega = 0.9f$ which at the lowest latitude of Palau's main island group, 7°N, is 1.5996e-05 rad/s (T = 4.5 days).

2.3 Results

2.3.1 Background State of the Local Waters around Palau

Response of the local waters to strong forcing is predicted to be strongly baroclinic by looking at the Stratification Parameter

$$S = \frac{NH}{fL} \sim 5.6, \qquad 1$$

where N is the maximum Brunt-Viasala frequency in the profile, H is the water depth, L is the shelf width, and f is the Coriolis parameter (Wang & Mooers, 1976). These values were determined using a mean ARGO profile (Roemmich & Gilson, 2009) off of the East coast of Palau (Figure 2.2) and spatial scales were determined by mean offshore topographic profiles taken off of the East and West coasts from the (Smith & Sandwell, 1997) 1 minute global bathymetric model (Figure 2.3). Both coasts show steep slopes, with max depths of 8000 m within 35 km of the East coast, and max depths of 4200 m within 60 km offshore off of the West coast. The distance between the coastline and the maximum offshore depth is used as the offshore length scale, L. The stratification parameter indicates the role of stratification in relation to the local length scale of the offshore topography. When $S > 1$ the ocean's response to perturbations should be dominated by baroclinic motion (J M Huthnance et al., 1986). This relation should be adjusted for a two layer system, as the original formulation assumes near linear stratification (David C Chapman, 1984). This adjustment accounts for both the layer depth and density gradient through reduced gravity

$$\hat{S} = \frac{\sqrt{g' \bar{h}}}{fL} \quad (2)$$

where

$$\bar{h} = \frac{H_1 H_2}{H_1 + H_2} \text{ and } g' = g \frac{\rho_2 - \rho_1}{\rho_2}, \quad (3)$$

and shows a stratification-dominated system for this case with a $\hat{S}$ value of 4.5 when the depth of layer-1 is considered to be 200 m.

Throughout the majority of the observational time period, May through December 2013, winds were dominated by the summer southwesterly monsoonal flow pattern (Figure 2.4a) which is typical for Palau during this period (Kubota et al., 2005). Time tagged cross-correlations were computed between the meridional components of the winds observed at both meteorological stations, M1 and M2 (Table 2.1), between 21 May and 31 October 2013. Peak cross-correlation were at a time lag of 0 days with a correlation coefficient of 0.73 ($P < 0.001$). Wind fronts propagating along-coast would produce a peak within this time-lagged cross-correlation curve, but we do not expect this was the case because of the 0 day time lag in these data. This cannot be more thoroughly examined without a spatially dense set of meteorological observations.

Temperature records showed large subtidal variability along with structure that exceeded a 20-day period which is consistent with seasonal and inter-annual variability (Figure 2.4b). Filtering methods eliminated these spectral ranges and maintained the super-tidal period signals. The temperature range at site T1 was between 25°C and 30°C (Figure 2.4b), but the array did

capture temperatures down to 18°C at other sites during the observational window, likely due to internal waves.

Time-lagged cross-correlation of temperature records from around the island group gave averaged values of wave speed between observation sites confirming the presence of a propagating feature with variable speed (Table 2.2). For along-coast distances between each observational site (T1-T6) see Table 2.1. Cross-correlations were computed between pairs of temperature records (T1 vs T*) for a range of time lags, $\pm$500 hours (Figure 2.5), to determine the peak correlation between records. To assess the background state this analysis was performed on both the Godin filtered and band-passed data over the 6 month observation period (01 May – 31 October, 2013) proceeding Typhoon Haiyan's impact on 6 November 2013. Time lags were determined by choosing the first peak in cross-correlation when the signal at T1 leads the signal in the record from the next along-coast record (Figure 2.5). Apparent propagation speeds computed using these time lags and the associated along-coast distances between observational sites (Table 2.1) were of the same order of magnitude between the two filtering techniques with values of 0.88 ± 0.07 m/s for Godin filtered temperature records and 0.57 ± 0.21 m/s for band-passed temperature records. Results between sites T1 and T2 for the Godin filtered data were excluded since they had had a time lag of 0.5 hours, giving unrealistic propagation speeds for coastal trapped waves of 26.11 m/s. Simplified modeling cases of the expected phase speeds in the region will be discussed in Section 3.3 showing why these are unrealistic.

The peak in cross-correlation between site T1 and sites T2 and T6 was small compared to site T1 and T3 – T5 during the May – October period (Figure 2.5). While all sites are connected by a continuous 500 m isobath around the island group there are channels with depths exceeding

100 m at both the northern and southern extends of Palau's main island group. These deep channels result in discontinuous isobaths (both 57 m and 90 m) between site T1 and T6. Site T2 sits at the northern end of the southern channel. Waves propagating near T2 will be affected by dynamics occurring within this channel, such as the strong flows that were measured to be greater than 2 m/s in later observational campaigns in 2015 and 2016.

2.3.2 A Strong Forcing Event – Typhoon Haiyan

Typhoon Haiyan provided a large perturbation to local waters, allowing us to record and study data with potentially larger signals. As the storm system passed Kayangel Atoll, to the north of the main island group, at 18:00:00 UTC on 6 November 2013 the Joint Typhoon Warning Center (JTWC) reported maximum wind speeds of 87.5 m/s. This corresponded with a reported minimum sea level pressure of 895 mb.

Local meteorological observations were made throughout the storm at a station roughly 100 km south of the storm track (Figure 2.1, M1 in Table 2.1) and an additional station was maintained just North of Kayangel Atoll (Figure 2.1, M2 in Table 2.1), but was destroyed by Typhoon Haiyan hours before passage of the eye of the storm. Wind speeds measured at the M1 station, reported as 3 hour averages, showed vector averaged wind speeds of only 18.8 m/s with maximum winds within the 3 hour averaging window of 24.4 m/s (Figure 2.6). Measurements of sea level pressure showed the atmospheric low-pressure signal dropped by 12 mb from the 30 day mean value to 992 mb. Due to the M1 station being in the southern extent of the storm it recorded significantly lower wind speeds than those reported for the system by the JTWC.

Nearshore currents observed by the ADCP (Figure 2.1), where the inertial period is 3.8 days, showed a large near-inertial response after Typhoon Haiyan (Figure 2.7). Due to the

proximity of the measurements to the coastline the currents were linearly polarized alongshore with the major axis of variance having a rotation angle 4.39 degrees clockwise from true north and containing 78% of the variance. This topographic steering of the flow altered the likely circularly polarized nature of these near-inertial currents. Ringing in the Godin filtered currents persisted for over one month after Typhoon Haiyan. Computed rotary spectra (Gonella, 1972) over a 60 day windows before and after the storm showed significant excitation in the near-inertial band after the storm, which was not excited preceding the storm (Figure 2.7).

Bottom pressure records collected around the barrier reef showed little relationship with the propagating features seen in water temperature (Figure 2.8). Due to the deployment depths of the pressure sensors being shallower than the thermocline we use the pressure data to compute Sea Surface Height (SSH) assuming small variability in density at those stations. To see the residual subtidal variability driven by the storm the records were de-tided and Godin filtered. The apparent lack of storm surge response in the array along the southern half of the island group was likely due to the relatively weak onshore local winds (Figure 2.6) in areas that might have allowed build-up of such a surge. Anomalies in Sea Surface Height (SSH) of -0.05 m and -0.1 m coincident with Typhoon Haiyan are present for P1 and P2 (Figure 2.8). This local minimum in Sea Surface Height anomaly (SSH') on 8 November was coincident with the peak in southerly winds and the subsequent change in the direction (Figure 2.6). SSH' and nearshore currents showed a maximum correlation of 0.83 between 04 November and 20 November 2013 when a time lag of 1.26 days was applied to the pressure record. In nearshore waters along-shore velocity, u, should be 90 degrees out of phase with η and η', which is seen in these records (Figure 2.S4) (J M Huthnance et al., 1986).

After Typhoon Haiyan passed Palau a progressive perturbation was seen propagating along-coast in the temperature records (Figure 2.9). Lines of constant phase used in both the 57 m and 90 m T-X diagrams show the perturbation extended throughout the upper layer of the water column. Computed apparent propagation speeds for these phase lines were 0.84 m/s. Evidence that the trapped signals made at least one more complete trip around the island group can been seen in the temperature records from 90 m (Figure 2.9).

Vertical displacements in the water column, η, due to the temperature anomalies were determined by computing the vertical temperature gradient, $T_z(z_j)$ at a given depth z_j, from the offshore mean ARGO profile (Figure 2.2e) and the demeaned temperature records (Figure 2.4b), $T(z_j, t)$, using the relation (Alford, 2003; Gregg, 1987)

$$\eta\,(z_j, t) = T(z_j, t) * T_z^{-1}(z_j). \qquad 4$$

This assumes that the density field is being driven by temperature (Gregg, 1987). At site T1 maximum vertical displacements, η, computed from band-passed temperature records were 10.9 m and 10.4 m at the 57 m and 90 m isobaths, respectively. As expected, the unfiltered temperature records, with a sampling period of 30 minutes, from site T1 showed much higher vertical displacements of 35.5 m and 45.7 m at the 57 m and 90 m isobaths, respectively. These displacements were sustained for 2.5 hours at the 57 m isobath.

The same time-lagged cross-correlation method that was used to assess the background state was applied to the temperature records from a 22-day period around Typhoon Haiyan, 01 – 22 November 2013 (Figure 2.5). There is a decay in correlation as the perturbations traverse away from T1 (Figure 2.5). We detected a signal propagation in Godin filtered temperature records at 57 m around the island group, which had apparent propagation speeds of 0.85 ± 0.23 m/s, similar

to what was seen in the T-X diagrams, 0.84 m/s (Figure 2.9). These propagation speeds were determined using filtered data. We tested two different filters (Godin and band-pass) and both produced similar results with differences of 1.1% (Table 2.2). We conclude that the wave-guide, governed by both the local stratification and topographic variability, allowed for coherent signals to propagate both in the 6 months preceding the storm and the following month. The measured propagation speeds for these two time periods were within a factor of two of each other.

2.3.3 Modeling Results

We use of the vertical structure equation to obtain first order estimates of the phase speeds for free wave baroclinic motion using the local stratification. Through the use of the scaling relation in the Stratification Parameter adjusted for a two-layer system, $\hat{S}$, (David C Chapman, 1984; J M Huthnance et al., 1986) the role of stratification was expected to be dominant for this area and suggests that variability in the water column should be baroclinic. The climatological ARGO profile (Figure 2.2) and profiles provided by local glider observations (Schönau & Rudnick, 2015) show the stratification to be non-linear, thus the N^2 profile was not constant. The N^2 profile was extended to the sea floor by linearly interpolating between the deepest ARGO value at 1975 m to 1% of that value at the sea floor. The depth used for this calculation was 4500 m as used in (Picaut & Sombardier, 1993). Here, the rigid lid approximation is adequate since we are not examining the barotropic response, thus Mode-0 results are not realistic.

Results from the VSE show baroclinic Mode-1 phase speeds of 2.81 m/s which were substantially faster than those observed around Palau. The baroclinic Mode-2 through Mode-9 data show phase speeds ranging between 1.83 m/s and 0.37 m/s, more closely matching the observations (Figure 2.10c). Our VSE Mode-1 phase speeds of 2.81 m/s are consistent with

previous estimates of the first baroclinic gravity wave phase speed for this region of 2.8 m/s (Chelton et al., 1998) and 2.6 m/s (Picaut & Sombardier, 1993). The displacement modes (Figure 2.10) show that Modes-1-3 have the same sign at 55 and 90 m. The Mode-2 and Mode-3 displacement values are 99% and 97% of the Mode-1 value at 55 m and 94% and 79% at 90 m. These percentages were determined on the non-normalized profiles in Figure 2.10. Due to this similarity in modal structure and sign the phase of the temperature records cannot be used to determine a specific modeled mode. The displacement modes were also converted to pressure anomaly profiles so projections of Sea Surface Height anomaly (SSH') could be made using the vertical displacements predicted from the observed bandpass filtered temperature anomalies in Section 3.2. This projected a SSH' for Mode-1 of 0.159 m, relating $\eta(57\text{ m}) = 10.9$ m, and 0.092 m, relating $\eta(90\text{ m}) = 10.2$ m. As expected the projected surface displacements were smaller for each successive mode. SSH perturbations that had been de-tided and Godin filtered (Figure 2.8) were smaller than these values at each of the pressure gauges. The largest observed SSH' post Haiyan were seen at P1 and P2 (Figure 2.8). As stated in Section 3.2, we think these are likely a response to the local wind field (Figure 2.6).

We next assess the combined role of topography and Coriolis using a two-dimensional model, BC85, with length scales derived from average topographic profiles taken from both the East and West coasts (Figure 2.3). These profiles lack a shelf and show considerably steeper topography than other large coastal trench cases such as along Japan or Peru (K H Brink, 1982; Igeta et al., 2007; Kajiura, 1974; Pietri et al., 2014). Assuming the length scales stated in Sections 1 and 3.1, BC85 solves for ω numerically via resonance iterations for our two topographic profiles (K H Brink, 1982). Phase speeds were computed using the MATLAB package bigc*.m. This is an updated version of the original FORTRAN software freely available online from Dr. Kenneth

Brink (Kenneth H Brink & Chapman, 1985). This variant is for a straight coast case and allows for complex frequencies, and thus dissipation in the offshore direction. The straight coast model was hypothesized to be applicable due to the long (120 km – 160 km) straight nature of the coastline on the east coast of Palau. Results of the BC85 application are shown through quasi dispersion curves (Figure 2.11). These are quasi dispersion curves due to the fact that BC85 solves for discrete values of frequency thus they do not represent a continuous dispersion relationship (K H Brink, 1999). Group velocity can be computed with an approximate dispersion relationship using these quasi dispersion curves. The highest frequency quasi dispersion curves for both the east and west coasts give group velocities of 0.10 and 0.20 m/s, respectively. Due to the assumptions made in BC85 and the discontinuous nature of these curves we do not attempt to analyze them further.

The model assumes an infinite coast while requiring an along-coast wave number as an input. BC85 iterates towards solution for a single ω. The internal Rossby radius

$$R_{internal} = \frac{1}{f}\sqrt{g'\bar{h}} \sim 195\ km \qquad 5$$

allowed for an initial estimate of a maximum along-shore wavelength (Cushman-Roisin & Beckers, 2011). The application of the VSE gave a smaller estimate for the internal Rossby radius, 147.5 km (Figure 2.10). The VSE estimate was preferred as it accounts for the full Brunt Vaisala frequency profile and is not a simplified two-layer approximation. The maximum along-shore wavelength was set at 160 km since the maximum meridional length scale of Palau is ~160 km, corresponding well with the first baroclinic Rossby radius determined with the VSE. The minimum along-coast wavelength used when forcing BC85 was 20 km. Model runs forced with along-coast wavelengths less than 90 km produced spurious results. The along-coast wavelengths

used to force BC85 were much less than the full circumference of the island group, ~350 km, thus we are not concerned with the first azimuthally quantized mode, but higher order modes do fall within the range of applicable along-coast wavelengths.

2.4 Conclusion and Discussion

Our results from data collected during our observation period, May through December 2013, indicate that the observed baroclinic CTWs are a feature of the background. These baroclinic CTWs were detected with an array of thermographs located near the 57 m and 90 m isobath after filtering out both the diurnal variability and signals with periods greater than 20 days. Time-lagged cross-correlation of temperature records at different observational sites were used to estimate apparent propagation speeds that showed spatial variability, but were all within a range of 1 m/s (Table 2.2). Results were similar between the Godin and band-pass filtering methods. The forcing of the background state was not determined, i.e. if waves were locally wind-forced or remotely-generated features. These estimates were limited in quality by the strength of the signal, particularly for the distant stations.

Typhoon Haiyan provided a large, broadband atmospheric forcing to the local water around Palau. Due to the track location and intensity of the storm, reported by the JTWC, Typhoon Haiyan likely produced a significant along-shore wind pulse in the vicinity of the northeast coast of Palau before passing Kyangel Atoll (Figure 2.1). Measurements of nearshore currents on the East coast showed a broad near-inertial response that persisted for one month after the event (Figure 2.7). A sub-inertial propagating coastally-trapped baroclinic wave was recorded in the temperature data around Palau at both 57 m and 90 m (Figure 2.9). The large value of the stratification parameter and a lack of corresponding water level perturbations supports this being a dominantly baroclinic response. The wave's frequency was near to sub-inertial as supported by rotary spectra. The results

of the time-lagged cross-correlation estimated apparent propagation speeds of the CTWs to be 0.85 $\pm$ 0.23 m/s (Table 2.2). We hypothesize that the large intensity along-shore wind burst along the northeast coast of Palau was the generation mechanism for the CTWs seen in the temperature records upwards of a week after Typhoon Haiyan impacted the area. This generation mechanism was described by (Thomson, 1970). Capture of these propagating waves, which over went a full 180 degree heading change as the propagated around Palau, proved to be a unique set of observations. Remarkably, these waves drove large temperature fluctuations at locations over 240 km along-coast from their generation site after propagating through multiple deep channels and passed headlands.

The CTWs observed around Palau help to increase the variation and rapidity of the previously documented (Wolanski et al., 2004) temperatures impacting benthic slope communities. During El Nino Southern Oscillation (ENSO) neutral conditions, there is almost certainly moderate cycling of sub thermocline water to shallow depths (less than 60 m) on outer reef slopes (Baker et al., 2016), which is beneficial for corals that occur in this section of the reef slope. During La Nina periods, however, the thermoclines are too deep (100 m or more for sub 20^{o}C water) for CTWs to bring cold, sub-thermocline waters onto reefs to provide relief from heat stress inducing coral bleaching. During El Nino's the opposite occurs and the thermocline moves to shallower depths and CTWs can bring water of sufficiently low temperature to induce "cold water bleaching" (Glynn, 1993) to deeper corals (40-75 m depth).

Our two semi-analytical models provide phase speed solutions that are comparable with the observed phase speeds. These models are intended to provide insight into the role of static and temporally varying properties of the nearshore region that regulate wave-guide physics. However, the results and model structure output should be interpreted with caution, as they do not contain

the range of ocean scales and dynamics that exist in nature (e. g. bathymetric variation, ocean state variability). Mode-1 phase speeds computed with the vertical structure equation, 2.81 m/s, are a factor of 2-3 faster than the observed phase speeds, and the Mode-2 through Mode-9 results, ranging between 1.83 m/s and 0.37 m/s, are on the order of the observations. The CTWs found by BC85, with phase speeds between 0.07 m/s and 0.40 m/s, are slower than the observed propagation speeds and the lower mode results just noted from the VSE. With the steepness of the offshore topographic profiles in the vicinity of Palau and the dominant role of stratification these waves fit with the theory of coastally trapped internal Kelvin waves along a vertical wall. For $\omega < f$ and $S >> 1$, (J M Huthnance et al., 1986)] defined this to be the likely propagating wave type. Differences may be due to inhomogeneity in alongshore bathymetry and oversimplified modeling.

More advanced numerical modeling could provide insight in to the wave-guide's along-coast variability and offshore structure. We expect the headlands and variations in coastal morphology cause modal interactions that could not be examined without a more spatially dense array of instrumentation that would not be feasible to maintain without large cost. Simulations of the changing oceanographic environment would allow for a data-rich test bed to probe for these characteristics.

2.5 Acknowledgements

We are thankful for the efforts of the staff from the Coastal Research and Development Center at the Scripps Institution of Oceanography, including S Scott, W Middleton, J Hazard and M Ortero, who led the preparation and implementation for both the current meter, water level and meteorological data collection. We thank the staff at the Coral Reef Research Foundation, including L Colin, M Mesubed, and E Basilius, for their assistance with this work as they helped to established and maintain the thermograph arrays in Palau. We thank both M Hendershott and K

Winters for their thoughtful feedback on this manuscript. Finally, we thank both the editor and the two reviewers for their insightful feedback on this work. This work was funded by the Office of Naval Research under the FLEAT DRI (Grant Number N000141512304). Oceanographic and meteorological observations presented in this paper are available from the authors upon request (eterrill@ucsd.edu). The Roemmich and Gilson ARGO climatology can be accessed at http://sioargo.ucsd.edu/RG_Climatology.html.

Chapter 2, in full, is under review at Continental Shelf Research, 2018, Schramek, Travis A.; Terrill, Eric J.; Colin, Patrick L.; Cornuelle, Bruce D. The dissertation author was the primary investigator and author of this paper.

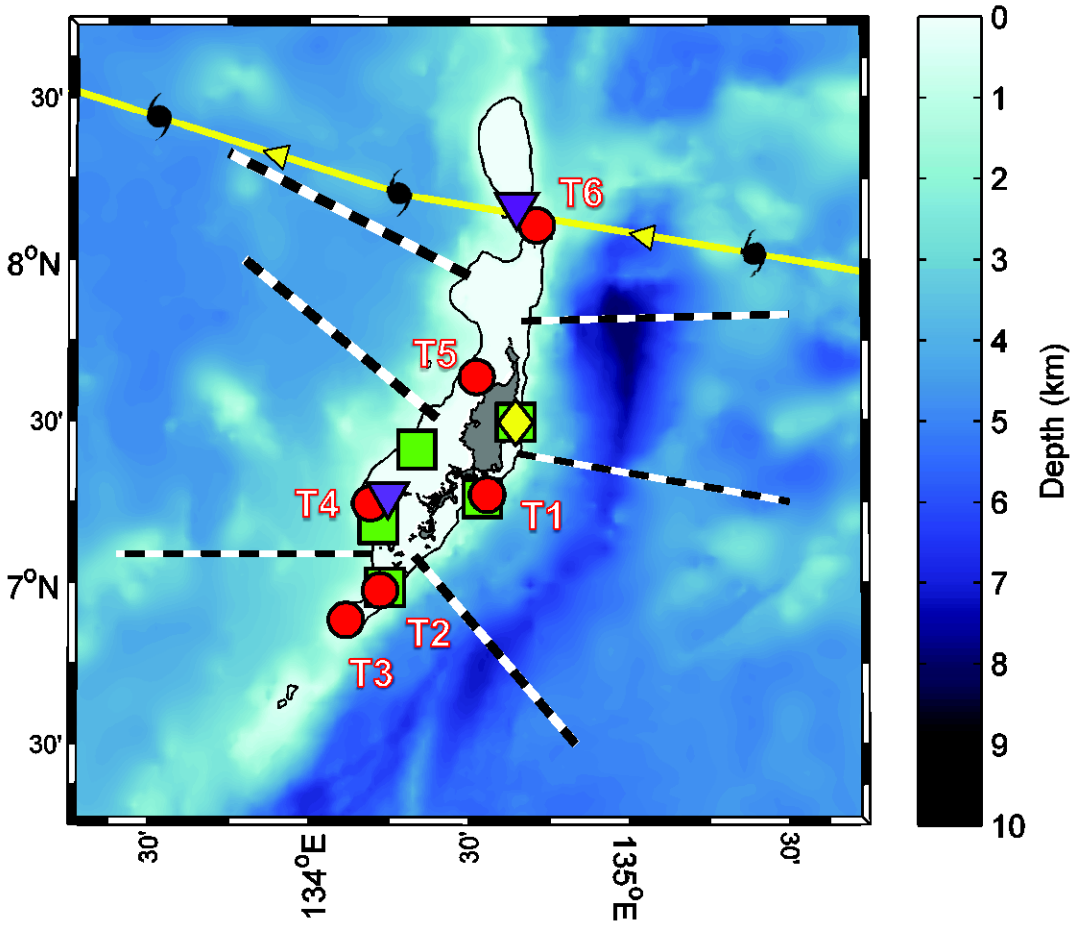

Figure 2.1: Positions of observational instrumentation deployed around Palau during May – December 2013 including thermographs (red-circles, with labels), water level gauges (green-squares), an ADCP (yellow-diamond), and the meteorological station (purple-triangles). Offshore bathymetric transects (white and black dashed line) were taken to generate a mean offshore profile for the East and West coasts (Figure 3) with three profiles from the East and West coasts. The 500 m isobath is shown to demark the major island mass. Note that there are large channels within this contour both in the northern and southern extents of Palau. Typhoon Haiyan's track is denoted by a yellow line and direction of movement indicated by yellow arrows.

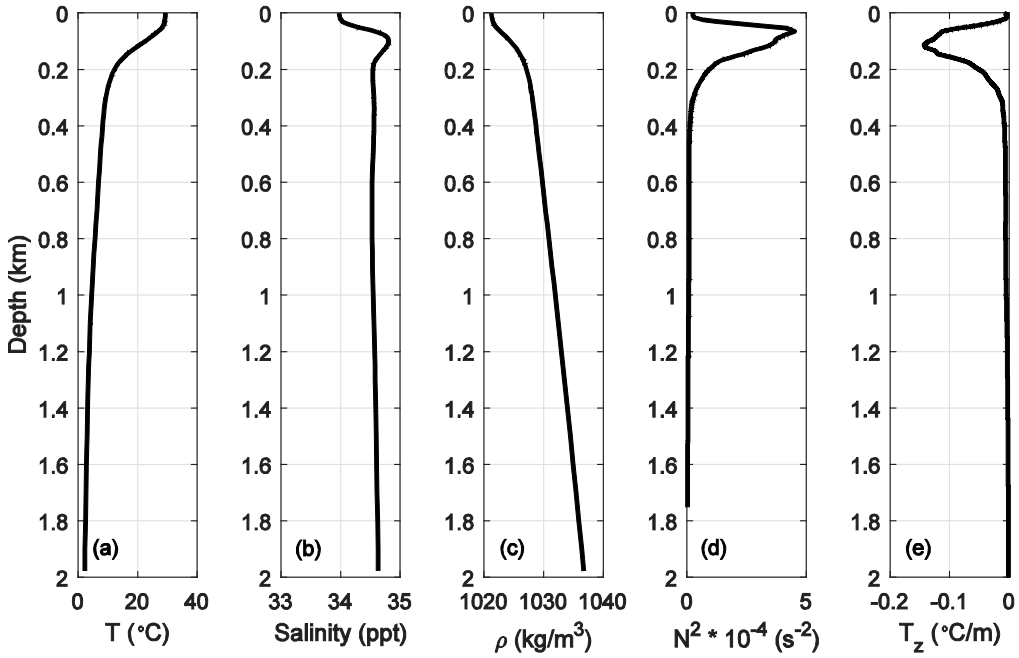

Figure 2.2*:* Mean ARGO profile for 2004-2014 taken from grid point 7° 25.00N, 134° 45.00E. (a) Temperature, (b) Salinity, (c) Density, (d) Brunt-Visalia Frequency, (e) Vertical Temperature Gradient.

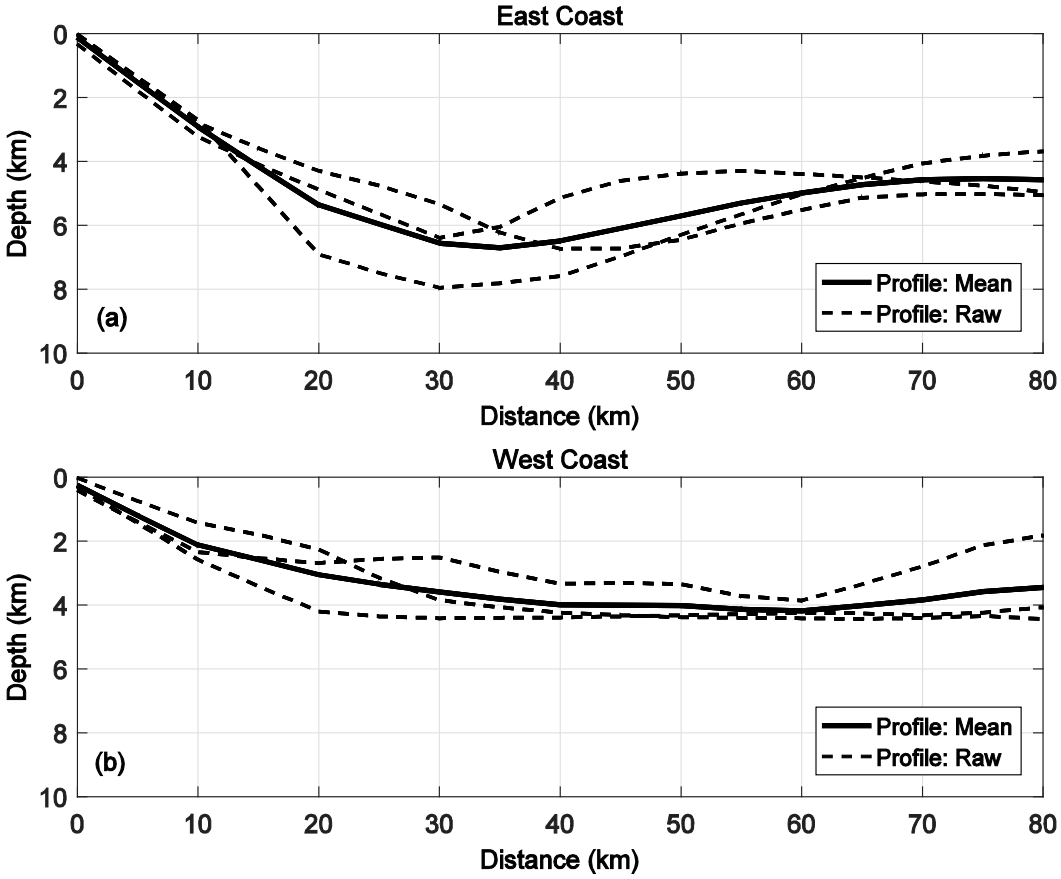

Figure 2.3: Offshore bathymetric profiles taken from the (a) East and (b) West coasts shown in Figure 1. Mean offshore profiles, solid lines, were computed from the three representative profile, dashed lines, from each region.

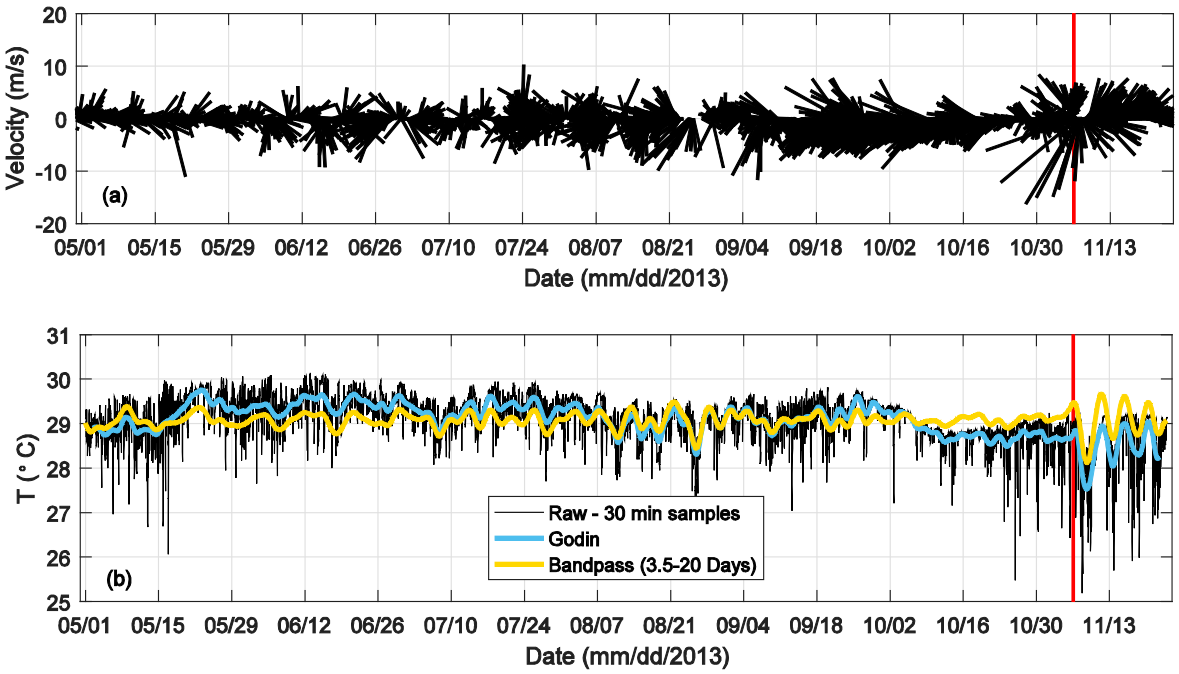

Figure 2.4: Wind vectors from M1 (Table 2.1 and Figure 1) show the monsoonal wind busts throughout the observational period. The vertical red line in both (a) and (b) indicate when Typhoon Haiyan passed through Palau on 6 November 2013. (b) Temperature records from 57 m deep at Station T1 with both the Godin filter (blue line) and 4th order Butterworth Band-pass filter (yellow line) applied with a pass band of 3.5-20 Days.

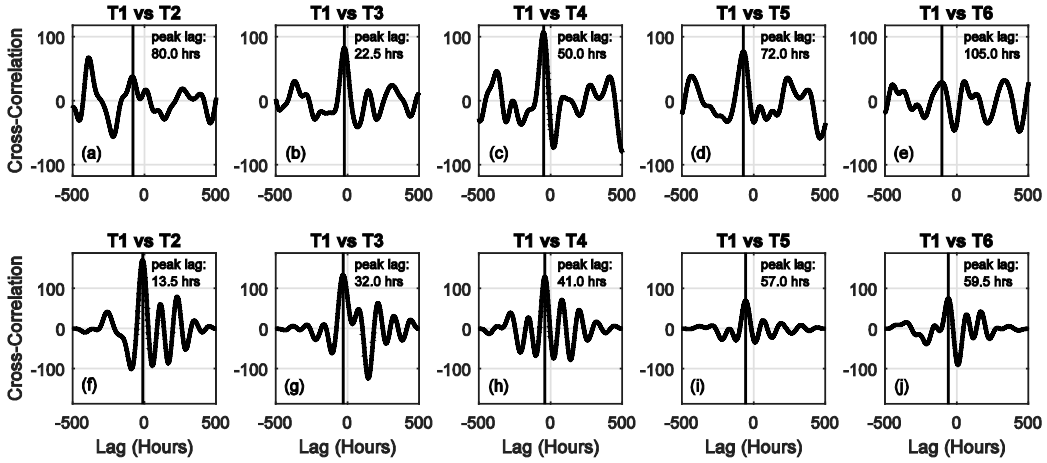

Figure 2.5: Cross-correlations between the band-passed (3.5-20 Days) temperature records for a range of time lags (hours) between T1 and T2-T6. The cross-correlations have not been normalized to their max value to allow for comparison between successive sites. Values were computed for a time period representing the background state, 01 May – 31 October 2013 (a-e). These are shown in comparison with those from a 22-day window around Typhoon Haiyan, 1 November – 22 November 2013 (f-j). The first peak in cross-correlation where T1 leads T* is shown with a vertical black line denoting the time lag, noted in the subplots.

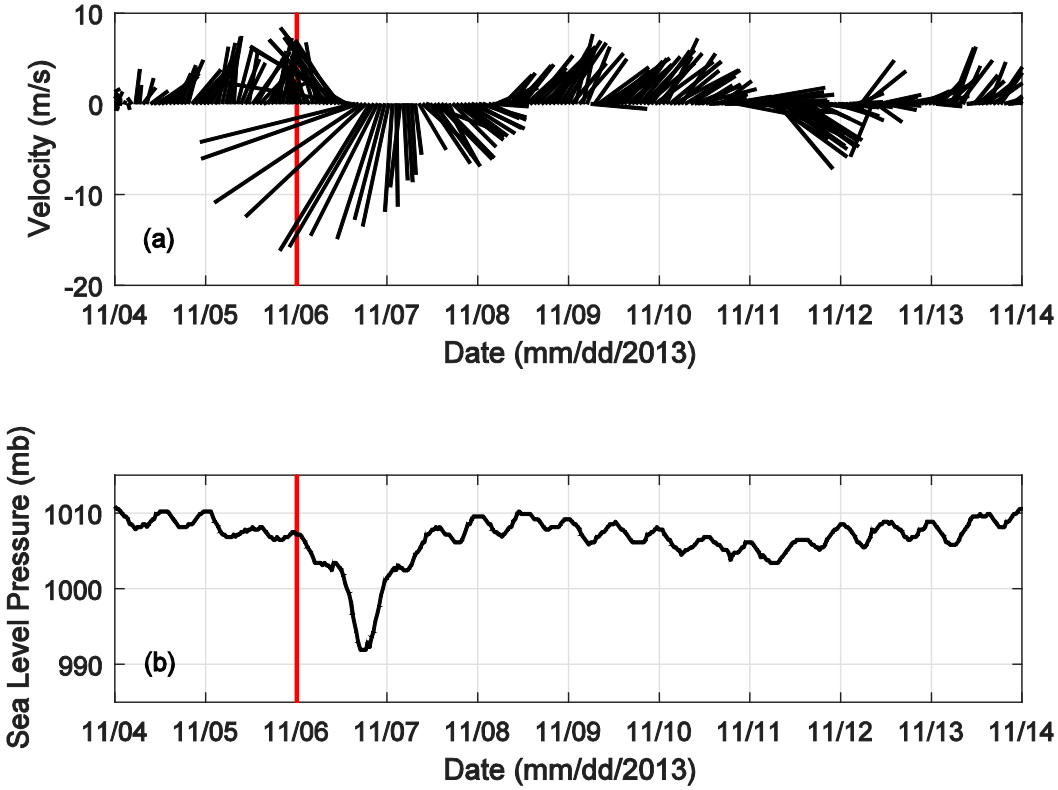

Figure 2.6: Meteorological Data recorded between 04 – 14 November 2013 at site M1 (Figure 1and Table 2.1). Typhoon Haiyan's impact can be seen on 6 November in the wind vectors (a) and sea level pressure (b). The vertical red lines in these subplots indicate when Typhoon Haiyan passed through Palau on 6 November 2013.

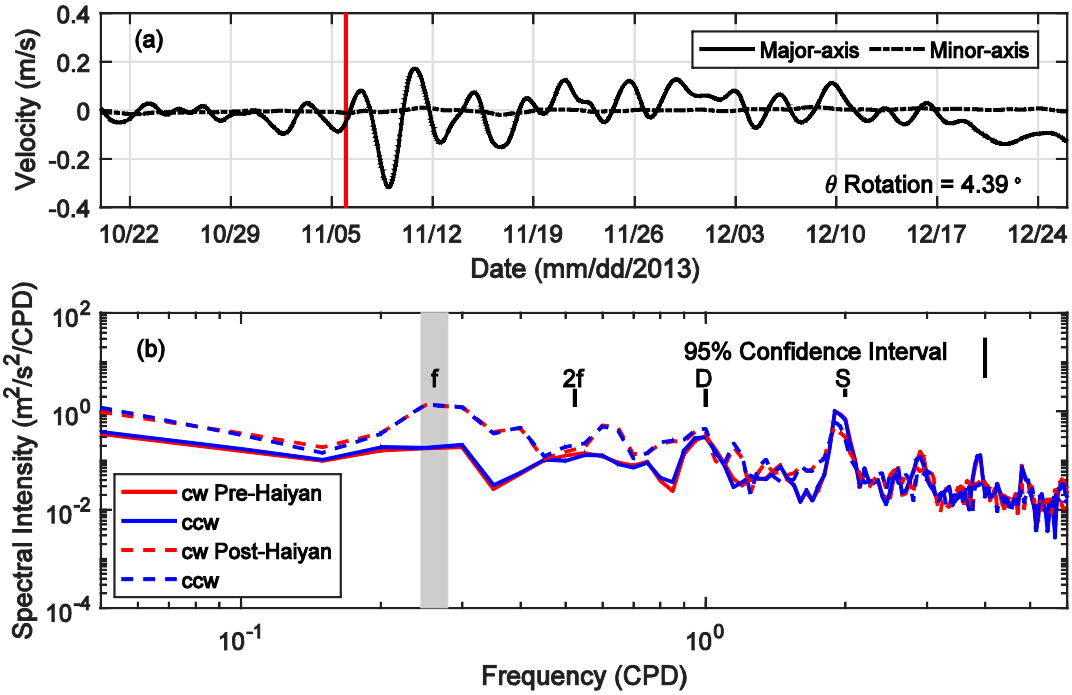

Figure 2.7: ADCP observations at C1 (Figure 1 and Table 2.1) in the central region of the East coast of Palau between 17 October – 26 November 2013. (a) Depth averaged, and Godin filtered current velocities. These data are rotated into principal axis where major is along-coast and minor is cross shore. The red line indicates when Typhoon Haiyan passed through Palau on 6 November 2013. (b) Rotary spectra computed for two separate time windows, 60 days before the storm's impact on 6 November, solid lines, and 60 days after the storms impact, dashed lines. Labels on the plot include f denoting the inertial band, 2f denoting 2* the inertial band, D as the diurnal band and S as the semidiurnal b, D as the diurnal band. The vertical black line in the upper right denotes the 95% confidence interval.

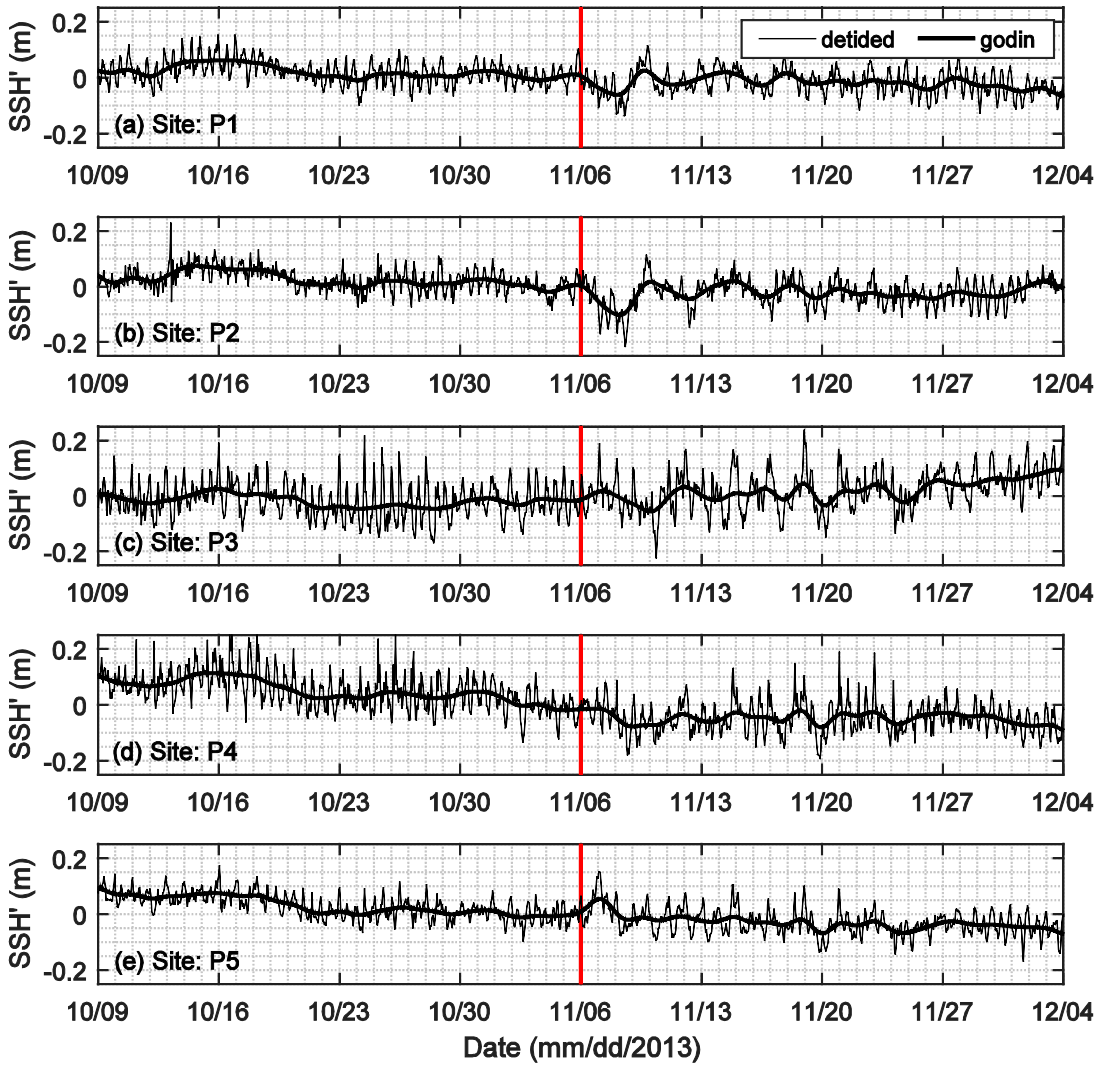

Figure 2.8: De-tided pressure gauge observations from sites P1-P5 (a-e). Each of these pressure records were used as input in the Matlab program t_tide and the predicted tidal components of SSH were removed from the record leaving the residual water level (thin line). These data were also Godin filtered (thick line) to see the subtidal variability. The red line indicates when Typhoon Haiyan passed through Palau on 6 November 2013.

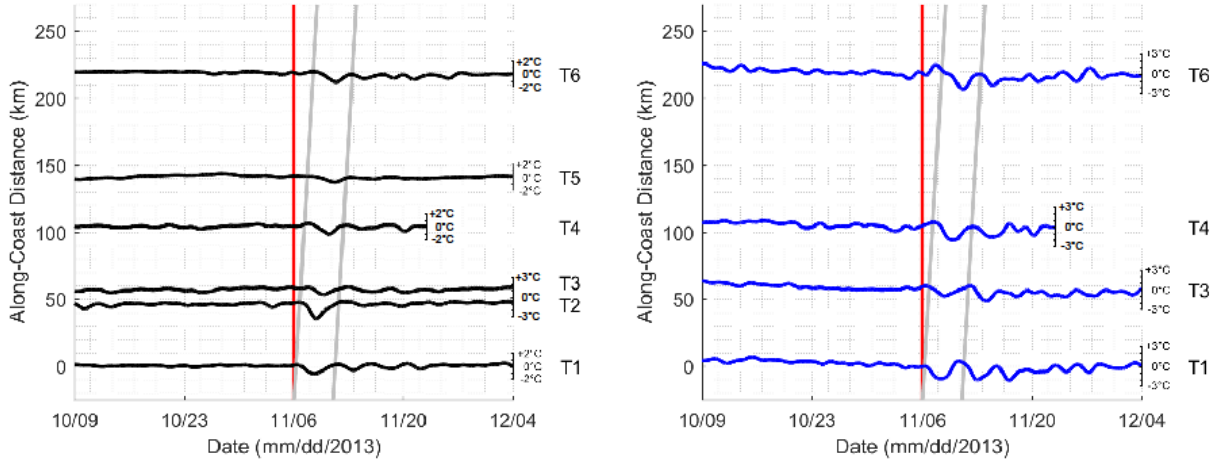

Figure 2.9*:* (a) T-X diagram of demeaned temperature records from T1 to T6 (Figure 1) at 57m, black, placed at their respective distances from observation point T1. Distance between sites is measured clockwise around the island chain, as noted in Table 2.1. The red line indicates when Typhoon Haiyan passed through Palau on 6 November 2013. Data was normalized by their respective variances for visualization purposes. Individual y-axis on the right side each time series show the temperature anomaly. Gray lines indicate lines of constant phase with an apparent propagation speed of 0.84 m/s. (b) Demeaned temperature records from 90 m, blue. As in (a) gray lines indicate lines of constant phase with an apparent propagation speed of 0.84 m/s.

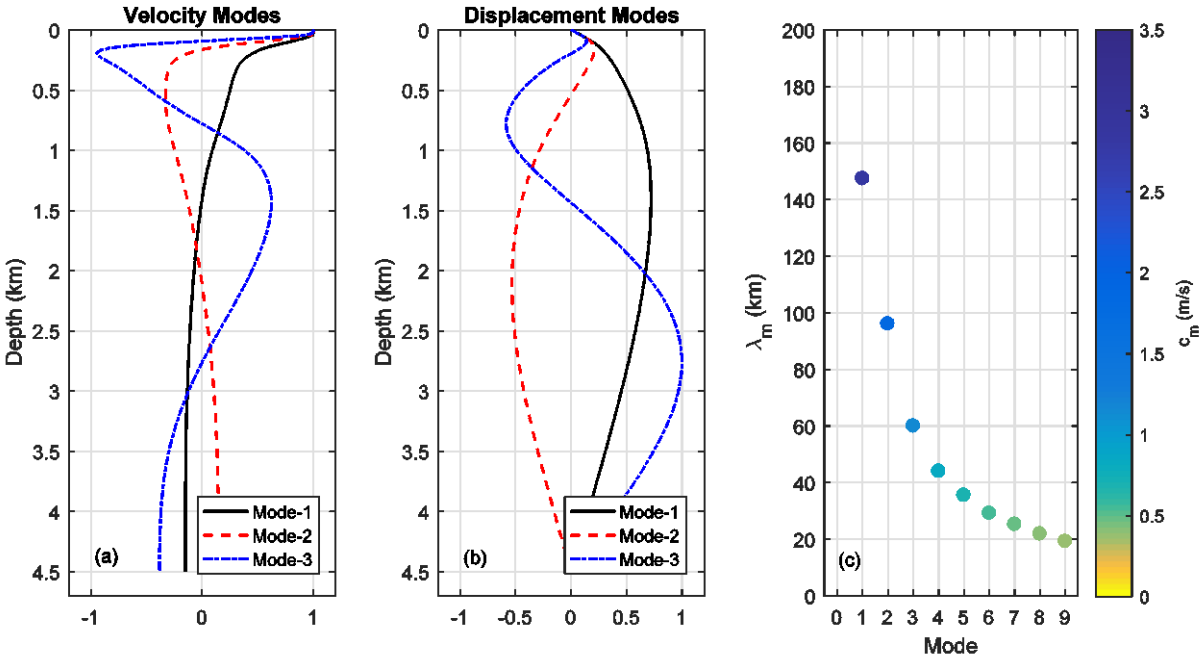

Figure 2.10: (a) Velocity mode structure for the first three baroclinic modes computed using the vertical structure equation applied to the mean ARGO profile in Figure 2. The profile was extended to a depth of 4500 m via linear interpolating from the deepest ARGO derived N2 value to 1% of that value at the bottom. (b) Displacement modes derived by integrating the velocity modes. (c) The associated phase speeds for each of the modes shown in (a) and (b) as well as the higher computed modes. Phase speeds for Mode-1, Mode-2, and Mode-3 are 2.81 m/s, 1.83 m/s, and 1.14 m/s, respectively. Rossby radii were computed by dividing the phase speeds by the local Coriolis parameter. The color bar is consistent with the one shown in Figure 11.

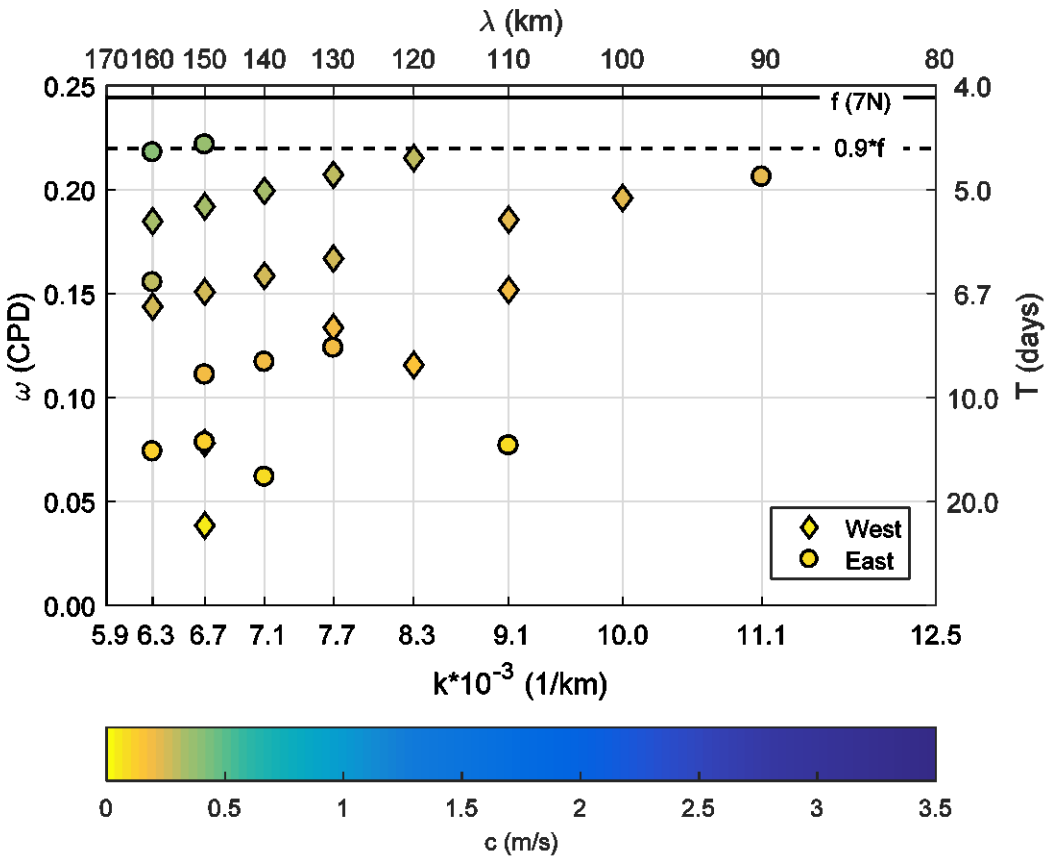

Figure 2.11: Trapped waves computed by BC85 for a range of user provided along-coast wave numbers. Quasi dispersion curves can be visualized extending through a range of frequency wave number pairings. Modeled phase speeds range between 0.07 m/s and 0.40 m/s. BC85 was run for the two sets of topographic length scales representing the East (circles) and West (diamonds) coasts in Figure 3. The color bar is consistent with the one in Figure 9. Lines showing the local inertial period f at 7N is shown (solid line) as well as 0.9*f (dashed line) which denotes where results from BC85 should be trusted.

Table 2.1: Positions, labels and depths of all referenced instruments depicted in Figure 1. The distances were computed starting at T1 and following the 500 m contour clockwise around the main island group, matching the expected propagation direction for CTWs in the Northern hemisphere.

Type	ID	Latitude	Longitude	Depth (m)	Along-coast Dist. from T1 (km)
Temperature	T1	7º 16.418' N	134º 31.440' E	57 & 90	-
	T2	6º 58.612' N	134º 13.330' E	57	47
	T3	6º 54.754' N	134º 07.635' E	57 & 90	63
	T4	7º 17.453' N	134º 14.442' E	57 & 90	117
	T5	7º 32.560' N	134º 28.059' E	57	163
	T6	8º 03.572' N	134º 41.027' E	57 & 90	242
Pressure	P1	7º 29.797 N	134º 38.780' E	13	-30
	P2	7º 15.667 N	134º 32.515' E	9	6
	P3	6º 59.204' N	134º 14.341' E	17	45
	P4	7º 10.869' N	134º 13.016' E	11	103
	P5	7º 24.336' N	134º 20.668' E	2	138
Current	C1	7º 29.797 N	134º 38.780' E	13	-30
Meteorological	M1	7º 16.260 N	134º 14.820' E	-	-
	M2	8º 10.318 N	134º 38.579' E	-	-

Table 2.2*:* Propagation speeds computed by dividing the time lag associated with the maximum cross-correlation of the two-time series and the distance between the respective thermographs. These calculations were performed using two different data sets: 01 May – 31 October, 2013, and a 22-day window in November 2013 to see the response to Haiyan. The 6-month time series was used to assess the background state. Two filtering methods were used to verify the subtidal signals, a Godin de-tiding running average and a Butterworth band-pass filter for periods of 3.5 - 20 days.

Phase Speed (m/s) of Maximum Correlation Between Stations				
Locations	**Godin**		**Band-pass**	
	May-Oct	**Nov (Haiyan)**	**May-Oct**	**Nov (Haiyan)**
T1-T2	-	0.97	0.16	0.97
T1-T3	0.97	0.49	0.78	0.54
T1-T4	0.76	0.79	0.65	0.79
T1-T5	0.85	0.79	0.63	0.79
T1-T6	0.92	1.20	0.64	1.12
Mean	**0.88**	**0.85**	**0.57**	**0.84**
Std	**0.08**	**0.23**	**0.21**	**0.20**

2.6 Appendix - Supplemental Information

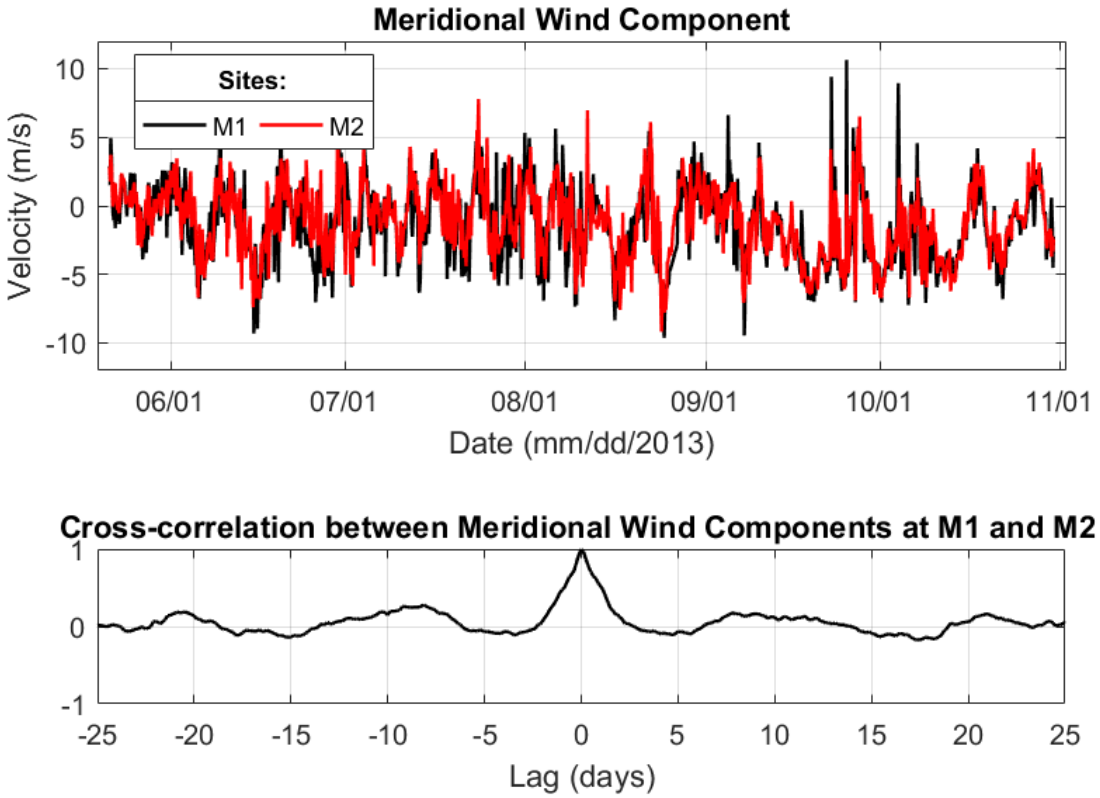

Figure 2.S1: (a) The meridional component of the wind field observed at M1 (black line) and M2 (red line) are presented for the period between 21 May and 31 October 2013. (b) Cross-correlations between the two wind time series presented in (a) over a range of lags in days. The peak cross-correlation was at 0 days.

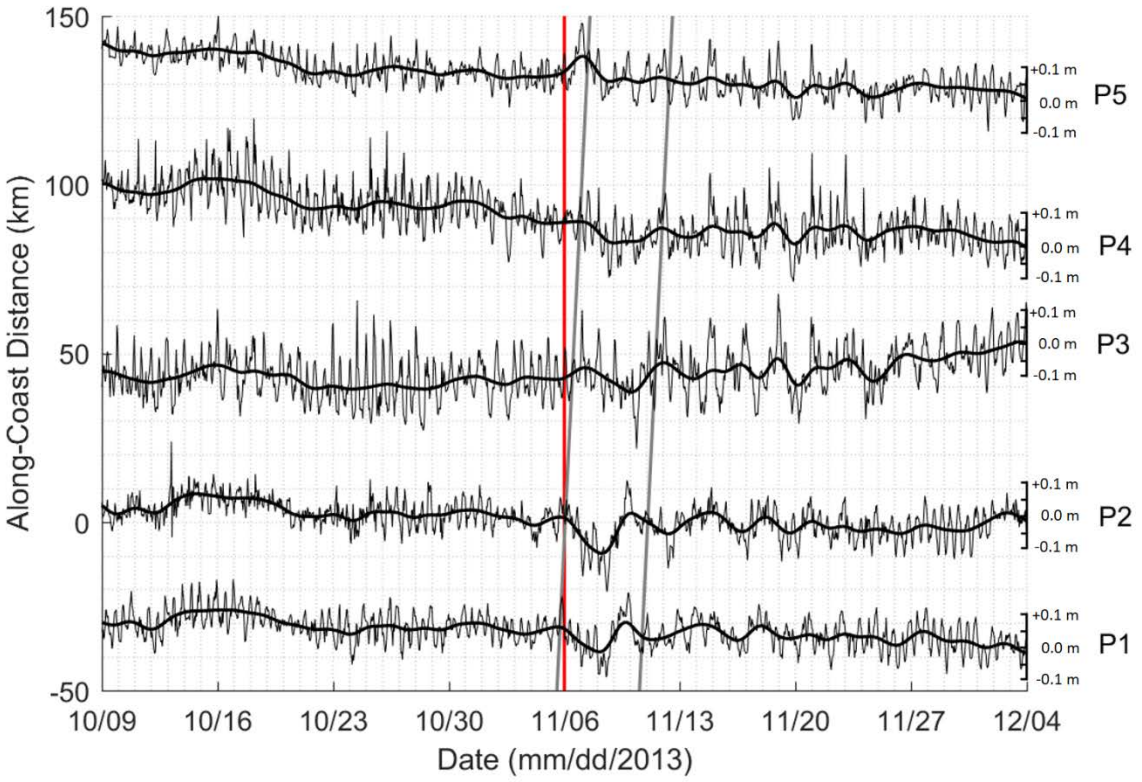

Figure 2.S2: T-X diagram of de-tided water level records (thin line – demeaned and de-tided, thick line – demeaned, de-tided and godin filtered) from P1 to P5 (Figure 2.1) at depths ranging from 2 m to 17 m, black, placed at their respective distances from observation point T1. Distance between sites is measured clockwise around the island chain and are noted in Table 2.1. The red line indicates when Typhoon Haiyan passed through Palau on 6 November 2013. Data was normalized by their respective variances for visualization purposes. Individual y-axis on the right side of the figure show the residual surface displacement in meters. Gray lines indicate lines of constant phase with a phase speed of 0.84 m/s.

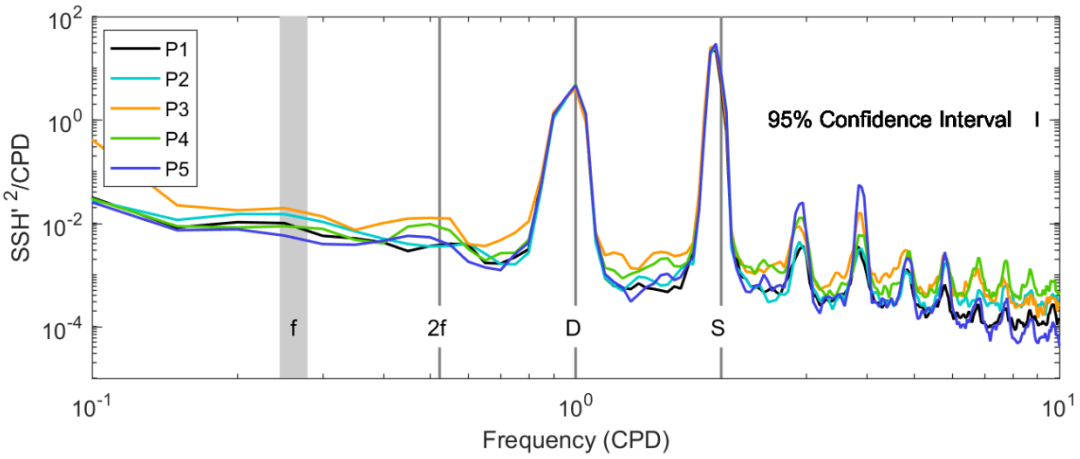

Figure 2.S3: Spectra computed over 60-day period around Typhoon Haiyan (using 20 day windows). The gray lines indicate (left to right) the inertial band, 2*internal band, diurnal band and semidiurnal band. Locations of P1 through P5 are listed in Table 2.1 and are shown in Figure 2.1.

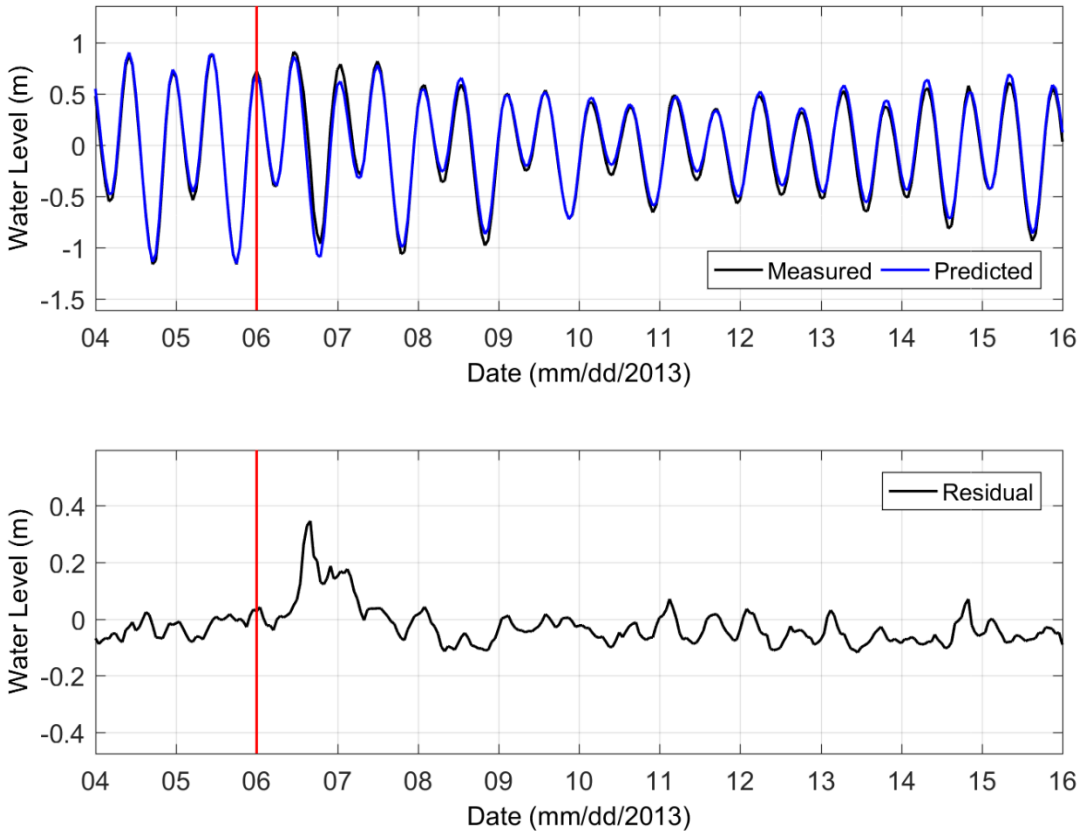

Figure 2.S4: (a) Water level (black) observed by the Malakal Harbor NOAA station and the predicted tides (blue) computed using the Matlab package t_tide. The red line indicates when Typhoon Haiyan passed through Palau on 6 November 2013. (b) Residual water levels (black line), found by subtracting the two-time series shown in (a), observed by the NOAA tide station in Malakal Harbor was 0.33 m. The residual water level peaked on 06 November, the same day as the storm's arrival, and dissipated within 24 hours of the maximum being recorded.

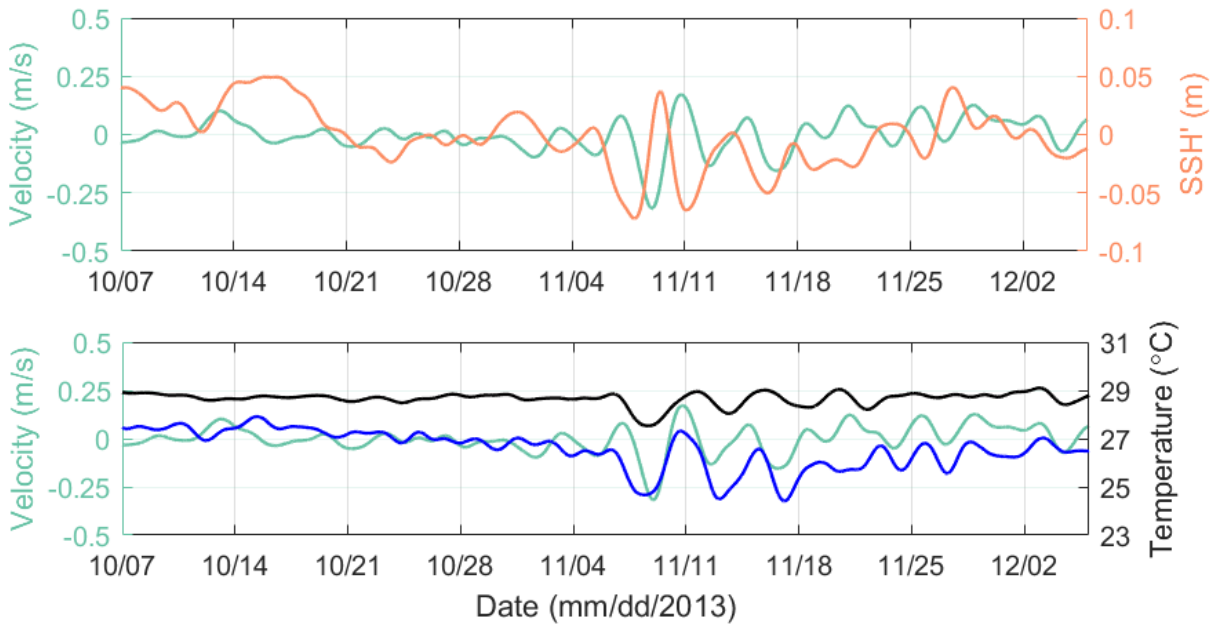

Figure 2.S5: (a) Depth averaged meridional velocity (left axis) from C1/P1 (same sight) versus pressure record that has been de-tided (right axis). Both records have been godin filtered. (b) Temperature records from both 57 m (black) and 90 (m) stations at T1 (right axis) versus the same velocity field shown in (a). Temperature records have also been godin filtered.

2.7 References

Alford, M. H. (2003). Redistribution of energy available for ocean mixing by long-range propagation of internal waves. *Nature*, *423*(March), 159–162. https://doi.org/10.1038/nature01628

Baker, E. K., Puglise, K. a., & Harris, P. T. (2016). Mesophotic Coral Ecosystems - A Lifeboat for Coral Reefs? In *The United Nations Environment Programme and GRID-Arendal Nairobi and Arendal* (Vol. 98, pp. 31–36).

Brink, K H. (1982). A Comparison of Long Coastal Trapped Wave Theory with Observations off Peru. *Journal of Physical Oceanography*. https://doi.org/10.1175/1520-0485(1982)012<0897:ACOLCT>2.0.CO;2

Brink, K H. (1991). Coastal-Trapped Waves and Wind-Driven Currents Over the Continental Shelf. *Annual Review of Fluid Mechanics*, *23*(1), 389–412. https://doi.org/10.1146/annurev.fl.23.010191.002133

Brink, K H. (1999). Island-trapped waves, with application to observations off Bermuda. *Dynamics of Atmospheres and Oceans*, *29*(2–4), 93–118. https://doi.org/10.1016/S0377-0265(99)00003-2

Brink, Kenneth H, & Chapman, D. C. (1985). *Programs for computing properties of coastal-trapped waves and wind-driven motions over the continental shelf and slope*. Woods Hole, MA: Woods Hole Oceanographic Institution. https://doi.org/10.1575/1912/5363

Buchwald, V. T., & Adams, J. K. (1968). The Propagation of Continental Shelf Waves. *Proceedings of the Royal Society A: Mathematical, Physical and Engineering Sciences*, *305*(1481), 235–250. https://doi.org/10.1098/rspa.1968.0115

Chapman, D C. (1983). On the Influence of Stratification and Continental Shelf and Slope Topography on the Dispersion of Subinertial Coastally Trapped Waves. *Journal of Physical Oceanography*. https://doi.org/10.1175/1520-0485(1983)013<1641:OTIOSA>2.0.CO;2

Chapman, David C. (1984). A note on the use of two-layer models of coastally trapped waves. *Dynamics of Atmospheres and Oceans*, *8*(1), 73–86. https://doi.org/10.1016/0377-0265(84)90005-8

Chelton, D. B., deSzoeke, R. a., Schlax, M. G., El Naggar, K., & Siwertz, N. (1998). Geographical Variability of the First Baroclinic Rossby Radius of Deformation. *Journal of Physical Oceanography*, *28*(3), 433–460. https://doi.org/10.1175/1520-0485(1998)028<0433:GVOTFB>2.0.CO;2

Colin, P. L. (2009). *Marine environments of Palau*. book, Taiwan: Indo-Pacific Press.

Cushman-Roisin, B., & Beckers, J.-M. (2010). *Introduction to Geophysical Fluid Dynamics. Physical and Numerical Aspects*. *Analysis* (Vol. 101). https://doi.org/10.1016/B978-0-12-088759-0.00022-5

Cushman-Roisin, B., & Beckers, J.-M. (2011). Stratification. In R. Dmowska, D. Hartmann, & H. T. Rossby (Eds.), *Introduction to Geophysical Fluid Dynamics* (Vol. 101, pp. 347–364). Elsevier. https://doi.org/10.1016/B978-0-12-088759-0.00011-0

Dukhovskoy, D. S., Morey, S. L., & O'Brien, J. J. (2009). Generation of baroclinic topographic waves by a tropical cyclone impacting a low-latitude continental shelf. *Continental Shelf Research*, *29*(1), 333–351. https://doi.org/10.1016/j.csr.2008.01.007

Foreman, M. G. G., Crawford, W. R., & Marsden, R. F. (1995). De–tiding: Theory and practice. In *Quantitative Skill Assessment for Coastal Ocean Models* (pp. 203–239). https://doi.org/10.1029/CE047p0203

Glynn, P. W. (1993). Coral reef bleaching: ecological perspectives. *Coral Reefs*, *12*(1), 1–17. https://doi.org/10.1007/BF00303779

Godin, G. (1972). *The Analysis of Tides* (Vol. 1). Toronto, Buffalo: University of Toronto Press.
Gonella, J. (1972). A rotary-component method for analysing meteorological and oceanographic vector time series. *Deep Sea Research*, *19*(12), 833–846. https://doi.org/10.1016/0011-7471(72)90002-2

Gregg, M. C. (1987). Diapycnal mixing in the thermocline: A review. *Journal of Geophysical Research*, *92*(6), 5249. https://doi.org/10.1029/JC092iC05p05249

Heron, S. F., Metzger, E. J., & Skirving, W. J. (2006). Seasonal Variations of the Ocean Surface Circulation in the Vacinity of Palau. *Journal of Oceanography*, *62*(1992), 413–426.

Hogg, N. G. (1980). Observations of Internal Kelvin Waves Trapped Round Bermuda. *Journal of Physical Oceanography*, *10*(9), 1353–1376. https://doi.org/10.1175/1520-0485(1980)010<1353:OOIKWT>2.0.CO;2

Hsin, Y. C., & Qiu, B. (2012). Seasonal fluctuations of the surface North Equatorial Countercurrent (NECC) across the Pacific basin. *Journal of Geophysical Research: Oceans*, *117*(6). https://doi.org/10.1029/2011JC007794

Huthnance, J M, Mysak, L. A., & Wang, D.-P. (1986). Coastal trapped waves. In *Baroclinic Processes on Continental Shelves. Coastal and Estuarine Sciences* (Vol. 3, pp. 1–18). https://doi.org/10.1029/CO003p0001

Huthnance, John M. (1975). On trapped waves over a continental shelf. *Journal of Fluid Mechanics*, *69*(04), 689. https://doi.org/10.1017/S0022112075001632

Huthnance, John M. (1978). On Coastal Trapped Waves: Analysis and Numerical Calculation by Inverse Iteration. *Journal of Physical Oceanography*, *8*(1), 74–92. https://doi.org/10.1175/1520-0485(1978)008<0074:OCTWAA>2.0.CO;2

Igeta, Y., Kitade, Y., & Matsuyama, M. (2007). Characteristics of coastal-trapped waves induced by typhoon along the southeast coast of Honshu, Japan. *Journal of Oceanography*, *63*(5), 745–760. https://doi.org/10.1007/s10872-007-0064-z

Jun, Z., Yuanlong, L. I., & Fan, W. (2016). Seasonal variation of the surface North Equatorial Countercurrent (NECC) in the western Pacifi c Ocean *. *Chinese Journal of Oceanology and Limnology*. https://doi.org/10.1007/s00343-016-5119-9

Kajiura, K. (1974). Effect of stratification on long period trapped waves on the shelf. *Journal of the Oceanographical Society of Japan*, *30*(6), 271–281. https://doi.org/10.1007/BF02109670

Kakinuma, T., & Nakayama, K. (2007). A numerical study on internal waves induced by a typhoon around a continental shelf. *SUISUI Hydrological Research Letters*, *1*(April), 1–4. https://doi.org/10.3178/suisui.1.1

Kawabe, M. (1982). Coastal Trapped Waves in a Two-layer Ocean. *Journal of Oceanographical Society of Japan*, *38*, 115–124. https://doi.org/10.1175/1520-0485(1975)005<0326:CTWIAB>2.0.CO;2

Kubota, H., Shirooka, R., Ushiyama, T., Chuda, T., Iwasaki, S., & Takeuchi, K. (2005). Seasonal Variations of Precipitation Properties Associated with the Monsoon over Palau in the Western Pacific. *Journal of Hydrometeorology*, *6*(4), 518–531. https://doi.org/10.1175/JHM432.1

Longuet-Higgins, M. S. (1967). On the trapping of wave energy round islands. *Journal of Fluid Mechanics*, *29*(04), 781–821. https://doi.org/10.1017/S0022112067001181

Longuet-Higgins, M. S. (1969). On the trapping of long-period waves round islands. *Journal of Fluid Mechanics*, *37*(04), 773. https://doi.org/10.1017/S0022112069000875

Mysak, L A. (1980). Topographically Trapped Waves. *Annual Review of Fluid Mechanics*. https://doi.org/10.1146/annurev.fl.12.010180.000401

Mysak, Lawrence A, Leblond, P. H., & Emery, Wi. J. (1979). Trench Waves. *Journal of Physical Oceanography*, *9*(5), 1001–1013. https://doi.org/10.1175/1520-0485(1979)009<1001:TW>2.0.CO;2

Pawlowicz, R., Beardsley, B., & Lentz, S. (2002). Classical tidal harmonic analysis including error estimates in MATLAB using T_TIDE. *Computers & Geosciences*, *28*(8), 929–937. https://doi.org/10.1016/S0098-3004(02)00013-4

Pedlosky, J. (1982). *Geophysical fluid dynamics*. *New York and Berlin, Springer-Verlag,*.

Picaut, J., & Sombardier, L. (1993). Influence of density stratification and bottom depth on vertical mode structure functions in the tropical Pacific. *Journal of Geophysical Research, 98*(C8), 14727. https://doi.org/10.1029/93JC00885

Pietri, A., Echevin, V., Testor, P., Chaigneau, A., Mortier, L., Grados, C., & Albert, A. (2014). Impact of a coastal-trapped wave on the near-coastal circulation of the Peru upwelling system from glider data. *Journal of Geophysical Research: Oceans, 119*(May), 2109–2120. https://doi.org/10.1002/2013JC009270

Roemmich, D., & Gilson, J. (2009). The 2004-2008 mean and annual cycle of temperature, salinity, and steric height in the global ocean from the Argo Program. *Progress in Oceanography, 82*(2), 81–100. https://doi.org/10.1016/j.pocean.2009.03.004

Schönau, M. C., & Rudnick, D. L. (2015). Glider observations of the North Equatorial Current in the western tropical Pacific. *Journal of Geophysical Research: Oceans, 120*(5), 3586–3605. https://doi.org/10.1002/2014JC010595

Smith, W. H., & Sandwell, D. T. (1997). Global Sea Floor Topography from Satellite Altimetry and Ship Depth Soundings. *Science, 277*(5334), 1956–1962. https://doi.org/10.1126/science.277.5334.1956

Suginohara, N. (1981). Propagation of Coastal-Trapped Waves at Low Latitudes in a Stratified Ocean with Continental Shelf Slope. *Journal of Physical Oceanography, 11*(8), 1113–1122. https://doi.org/10.1175/1520-0485(1981)011<1113:POCTWA>2.0.CO;2

Thomson, R. E. (1970). On the generation of Kelvin-type waves by atmospheric disturbances. *Journal of Fluid Mechanics, 42*(04), 657–670. https://doi.org/10.1017/S0022112070001532

Wang, D.-P., & Mooers, C. N. K. (1976). Coastal-Trapped Waves in a Continuously Stratified Ocean. *Journal of Physical Oceanography, 6*(6), 853–863. https://doi.org/10.1175/1520-0485(1976)006<0853:CTWIAC>2.0.CO;2

Wilkin, J. L., & Chapman, D. C. (1990). Scattering of Coastal-Trapped Waves by Irregularities in Coastline and Topography. *Journal of Physical Oceanography, 20*(3), 396–421. https://doi.org/10.1175/1520-0485(1990)020<0396:SOCTWB>2.0.CO;2

Wolanski, E., Colin, P., Naithani, J., Deleersnijder, E., & Golbuu, Y. (2004). Large amplitude, leaky, island-generated, internal waves around Palau, Micronesia. *Estuarine, Coastal and Shelf Science, 60*(4), 705–716. https://doi.org/10.1016/j.ecss.2004.03.009

Wolanski, E., Nhan, N. H., & Spagnol, S. (2012). Sediment Dynamics during Low Flow Conditions in the Mekong River Estuary, Vietnam. *Journal of Coastal Research, 14*(2), 472–482.

Zamudio, L., Hurlburt, H. E., Metzger, E. J., & Smedstad, O. M. (2002). On the evolution of coastally trapped waves generated by Hurricane Juliette along the Mexican West Coast. *Geophysical Research Letters*, *29*(23), 54–56. https://doi.org/10.1029/2002GL014769

Chapter 3:

Channel flow through an island group driven by geostrophic flows and topographic effects

Subtidal flows through a shallow (20-500 m), narrow (~10 km) channel in the Palau island group are described and related to large-scale currents impinging on the island topography. The observations used in this analysis include bottom pressure collected at 20-28 m depth around Palau, a current profiler at 20 m depth in the channel and High Frequency (HF) radar currents measured off of the eastern side of the island group. A high resolution (1/120° x 1/120°) regional circulation model is used to examine the space-time characteristics of the flow in the channel in comparison to the large-scale currents near Palau. A balance between the along-channel pressure difference and bottom friction in the channel was inferred based on the current and pressure observations and the high-resolution model simulations. A drag coefficient for the channel, computed using in situ observations, is $O(10^{-3}\text{-}10^{-4})$. Variations in large-scale zonal currents correlate with the pressure difference across the channel as well as the along-channel flow. The model simulations indicate that as the large-scale flow impinges on the island group, topographic blocking results in a pressure difference on either side of the island which causes a pressure gradient along the channel. Although the observations suggest a balance between bottom friction in the channel and the pressure gradient, a seven hour time lag of the channel current relative to the pressure gradient suggests other terms in the momentum balance, such as acceleration and advection, which was not directly measured, may contribute to the momentum balance. The findings suggest that the influence of large-scale circulation can penetrate across isobaths in to shallow coastal zones around islands and

through island gaps, and that topographic blocking and resulting small-scale pressure gradients are important considerations in determining near-island flows.

3.1 Introduction

Islands in the tropical Pacific typically have narrow coastal zones (~1 km) compared to continental margins. These narrow strips of nearshore waters around islands therefore are in close proximity, *O*(10) km, to deep water flow fields, but are not often examined with them in mind. Flows near islands are known to be driven by the local surface tide (Ulloa et al., 2018), internal waves (Smith et al., 2016), local winds (Lowe & Falter, 2015), coastally trapped waves (Chapter 2 of this dissertation), as well as surface wave driven setup (Becker et al., 2014) and alongshore pressure gradients (Ruessink et al., 2001). The influence of regional-scale, deep ocean flow fields in the nearshore of islands has not been widely reported, although Jarvis Island, in the direct path of strong equatorial flow, features strong pressure perturbations on the upstream and downstream side of the island (Gove et al., 2006; Roemmich, 1984).

Islands can influence regional large-scale geostrophic flows through wakes and standing eddies (Dong et al., 2007), lee waves (Nikurashin & Ferrari, 2011), and internal tides (Wolanski et al., 2004), as well as other processes leading to energy dissipation (Leichter et al., 2012). The energy dissipation and conversion driven by steep ocean topography influence the spatial structure of mixing in the world's oceans (Alford, 2003).

The Republic of Palau is an island group in the tropical western Pacific centered at 7.5°N and 134.5°E. Observations were made in the nearshore (< 30 m depth) environments of Palau between March 2014 and June 2018 to determine the relationship between oceanographic variability both in deep-water and on the fore reefs of a remote island group. Bottom pressure was

observed around the perimeter of Palau's barrier reef system between 20 and 28 m, while channel flow in a gap between Peleliu and Angaur islands was observed at the southern edge of the main island group (Figure 3.1). A submerged bank known as Hydrographers Bank lies in the middle of this channel rising from the channel floor at 500 m to 20 m depth. Flows in this channel are known to exceed 2 m/s and pose an unpredictable navigation hazard to the local community.

This chapter will attempt to answer two main questions: 1. what is the force balance in the channel? And, 2. what is the relationship between the channel flow and mesoscale and larger-scale circulation?

To answer these questions the momentum equations are scaled for the channel setting to estimate the order of magnitude of each term (3.3.1). The pressure field at the southern extent of Palau is compared to the channel flow, and, the along-channel pressure gradient is estimated to understand the frictional balance of the channel (3.3.2). A high resolution (1/120° x 1/120°) regional model is used to examine flow interaction with the island for comparison with the results obtained from the observations (3.3.3). In addition, the pressure difference and channel flow will be compared to geostrophic flows in the vicinity of Palau and local HF radar observations of surface currents to understand the extent of flows that may drive the channel flow (3.3.4). Finally, the force balance in the channel is used to estimate a bottom drag coefficient, C_D (3.3.5). A conclusion and discussion follow (3.4).

3.2 Data and Methods

3.2.1 Observational array and gridded products

In-situ pressure observations were made on the outer fore reef slopes around the main island group of Palau between March 2015 and June 2018 using RBR Inc Duo pressure loggers,

deployed in 2-28 m of water depth. The loggers sampled at 1-4 Hz for 17 minutes every hour. Pressure anomalies from mean depth have been converted to sea level, denoted as η, assuming constant density in this depth range based on temperature measurements made concurrently. Currents were measured with a bottom-mounted, upward facing TRDI Workhorse Acoustic Doppler Current Profilers (ADCP) at a single location on Hydrographers Bank at 6.9°N and 134.6°E at 1 m depth. Observations were collected at this station between March 2014 and June 2018 with recovery and redeployment of the ADCP at approximately 12 month intervals. Hydrographers Bank is a fully submerged plateau with a minimum depth of 20 m, extending 3 km north to south and 0.8 km east to west.

Daily sea level gauge records were obtained from the Malakal Harbor tide gauge station for 2014 through 2018 from the University of Hawaii Sea Level Center (http://uhslc.soest.hawaii.edu/data/;Caldwell et al., 2017). The tide gauge is located in the north east portion of Malakal Harbor adjacent to the main shipping port. Regional sea surface height and surface geostrophic currents were specified using the global ocean gridded L4 output, 0.25° × 0.25° resolution, from Copernicus Marine Environment Monitoring Service (CMEMS; marine.copernicus.eu/services-portfolio/access-to-products/). CMEMS has taken over data delivery and management for the products previously maintained by AVISO.

3.2.2 Statistical Techniques

The tidal component of the flow fields were examined and removed using t_tide (Pawlowicz et al., 2002). Low-pass filtering was done using a Hanning window maintaining periods longer than 7 days, leaving only sub-inertial variability.

3.2.3 High resolution ocean model

The Regional Ocean Modeling System (ROMS) was applied to a domain encompassing the main island group of Palau with a 1/120° x 1/120° resolution (Shchepetkin & McWilliams, 2005). The model domain extended from 5.5°-10°N and 131.5°-136.5°E, using bathymetric observations made by the RV Revelle starting in 2013, merged with ETOPO2 fields. This run, henceforth denoted as PALAU_120B, began on June 1st, 2016 and was run through July 1st, 2016, with output saved on an hourly increment. The model was run with tides and was nested in a regional state estimate (B. Powell & S Zedler, Personal communication) which assimilated altimetry, shipboard observations, spray glider observations, and other measurements collected during the experimental time period as part of the Office of Naval Research Flow Encountering Abrupt Topography (FLEAT) directed research initiative.

3.3 Results

3.3.1 The along-channel momentum balance

The dominant terms in the force balance for the channel flow at the southern extent of Palau are estimated by scaling the size of the terms of the x-momentum equation, which is denoted by

$$u_t + uu_x + vu_y - fv = -\frac{1}{\rho}\frac{dp}{dx} + C_D u|u|. \quad (1)$$

The terms of the x-momentum equation can be scaled as

$$\frac{U}{T} \quad \frac{U^2}{L_x} \quad \frac{U^2}{L_y} \quad fU \quad \frac{\rho g \Delta h}{\rho L_x} \quad C_D U^2, \quad (2)$$

where relevant length scales for this case are assumed to be

$$U \sim 10^{-1} \quad T \sim 10^5 \quad L_x \sim 10^3 \quad L_y \sim 10^4 \quad f \sim 10^{-5} \quad \Delta h \sim 10^{-2} \quad C_D \sim 10^{-2}. \quad (3)$$

The balance is being considered for subtidal flows through a zonal channel that is wide. The estimated order of magnitudes for each term in the x-momentum equation,

$$u_t + uu_x + vu_y - fv = -\frac{1}{\rho}\frac{dp}{dx} + C_D u|u|$$

$$10^{-6}\ \ 10^{-5}\ \ 10^{-6}\ \ 10^{-6} \qquad 10^{-4} \qquad 10^{-4}, \tag{4}$$

suggest that the pressure gradient and bottom friction term balance dominate. This balance will be tested using in situ observations and model output.

3.3.2 Pressure gradient related channel flow

Sea level obtained from the shallow bottom pressure observations from the fore reefs of the main island group of Palau (Figure 3.1) show a well-correlated subtidal response across the array over the course of one year of observations between March 2016 and March 2017 (Figure 3.2). Subtidal sea level variability at Malakal Harbor (Figure 3.3 MKH - gold line) agrees well with the spatial mean of subtidal sea level from the bottom pressure array (Figure 3.3, OBS – orange line). Regional sea surface height, taken at the closest point in CMEMS to the Malakal Harbor station, shows a slightly different magnitude of subtidal variability in contrast to the in situ measurements over the same time period (Figure 3.3, CMEMS – blue line). Subtidal variations in sea level at Palau are related to wind-driven, westward propagating Rossby waves (Chapter 1). Differences in sea level across the island are *O*(0.01-0.1) m (Figure 3.2).

The depth-averaged flow (0-20 m depth) in the channel captured with the bottom-mounted ADCP between March 2014 and June 2018 has speeds exceeding 2 m/s, with a significant tidal component (Figure 3.4a) and subtidal flows that are on the order of 0.5 m/s (Figure 3.4b) These flows are more energetic in the East-West (E-W) direction, representing along-channel flow,

compared to the North-South (N-S) direction, representing cross-channel flow. The tidal components of these observed flows are more thoroughly examined in Chapter 4 of this dissertation.

The sea level difference, $\Delta\eta$, E-W across the southern end of Palau covaries with the E flow, $u_{channel}$, at subtidal frequencies (Figure 3.5a-c). $\Delta\eta$ was computed between P12 on the southeast coast of Palau and P01 on the southwest coast (Figure 3.1). The correlation coefficients between $\Delta\eta$ and $u_{channel}$ are -0.66, -0.79, and -0.77 for the three separate deployments spanning from March 2015 to March 2016, March 2016 to September 2016, and March 2017 to March 2018, respectively. The sensor at P01 saw a drift starting in October 2016 during the 2016 deployment, thus the correlation was only computed over the first 7 months of the record.

3.3.3 1/120° x 1/120° modeling application

The high resolution ROMS simulation is used to assess the difference in sea surface height across the island group, $\Delta\eta$, and flow through the channel over the 1 month model run (Figure 3.7a). Daily averages of model-surface variables show illustrative periods of high westward flow in the channel, which corresponding to higher sea levels on the eastern, or "upstream", side compared to the western side of the island (June 19th, 2016, Figure 3.8a), with opposite sign sea level difference during high eastward channel flow (July 1st, 2016, Figure 3.8b). The spatial mean sea level is removed to better understand the spatial variability. Composite fields were computed based on the sign of the along-channel flow, as shown in Figure 3.7a, to determine if the pressure difference-channel flow relationship is robust throughout the month of model output. The output from the period of June 9th to June 14th shows the pressure-friction balance breaking down (Figure 3.7a). Generally, nearshore sea level anomalies occur in a narrow, 1-5 km, band directly adjacent

to the coast on the upstream side of the flow through the channel, although the pattern is weaker than what was seen in the synoptic fields, possibly due to the inclusion of periods with minimal zonal flow in the computation. The along-channel flow speed was large (~ 1 m/s) for easterly flow, both in the daily-averaged and composite fields. The North Equatorial Counter Current (NECC) flows west to east and is typically centered on 5°N, south of Palau. This major current system intermittently interacts with the main island group of Palau, driving the local flow fields, as seen in these synoptic and composite fields.

Along- and cross-channel sea level gradients are computed in the model to determine if the flow through the channel is locally geostrophic. The local sea level differentials in the along-channel (Figure 3.6c – orange squares) and cross-channel (Figure 3.6c – gold diamonds) direction are computed (Figure 3.9, orange line, gold line, respectively). Mean E and N velocities in the middle of the channel are from the grid points denoted by blue circles (Figure 3.6c). Velocities are rotated by 35.74° clockwise from 0 north to better represent along- and cross-channel conditions. The correlation coefficient between the along-channel flow and the along-channel pressure differential is -0.74, higher than the correlation determined for $\Delta\eta$ using grid points farther to the north (Figure 3.7). Correlation coefficients between the velocity components and the different pressure differentials are noted in the legend on Figure 3.9, in their respective order. The correlation between the cross-channel sea level difference across the channel and the along-channel flow is 0.57. The positive correlation between the meridional sea level gradient and zonal flow is opposite to the expected for geostrophic balance. Flows through the channel in the synoptic and composite fields (Figure 3.8) appear to be directed down the pressure gradient, which indicates the flow is not locally geostrophically balanced through the channel.

In the plot of model time series, $\Delta\eta$ appears to lead $u_{channel}$ slightly in time (Figure 9). The maximum lagged cross-correlation (-0.54) occurs at $\Delta\eta$ leading $u_{channel}$ by 7 hours (Figure 3.7b). $\Delta\eta$ leading $u_{channel}$ suggests that additional terms in the momentum balance play a role beyond the pressure gradient and bottom friction.

3.3.4 Relationship between channel current and the regional flows

The zonal pressure difference across the southern extent of Palau ($-\Delta\eta$ between P01 and P12) is shown to have a relationship with both the mesoscale, *O*(100) km, and regional scale, *O*(1000) km geostrophic currents in the vicinity of the main island group of Palau. Correlation coefficients between $\Delta\eta$ and CMEMS geostrophic flows, computed from observations and shown between March and September 2016, are positive and significantly different than zero over a broad region around the southern end of the islands group (Figure 3.10a,b). Correlations between the observed along-channel current and CMEMS zonal currents between March 2016 and March 2017 had a similar spatial pattern of correlation with $\Delta\eta$, but with reduced magnitudes (Figure 3.10c,d). Assessing the full four-year record of channel flows, a similar positive maxima in correlation between $u_{channel}$ and CMEMS zonal currents is found over the southern extent of Palau (Figure 3.10e,f).

Observations of surface currents off of Palau's east coast made by HR Radar show the downstream response of flow encountering the island group from the west during the summer of 2016 (Figure 3.11). Monthly mean surface currents show large amplitude zonal flows to the south east of Palau for June, July, and August of 2016 (Figure 3.11a-c, respectively). For July and August 2016, the flow appears to reconnect in the lee of Palau in this region coincident with peak

correlations between the CMEMS geostrophic flow fields and the in situ Δη (Figure 3.10a,b), and $u_{channel}$ (Figure 3.10a,b) during roughly the same time period.

3.3.5 Reassessing the force balance

A putative drag coefficient can be computed by equating the pressure term in the x-momentum equation and the $u|u|$ component of the friction term (Figure 3.12). The resultant C_D computed as a regression coefficient is 0.0006, in the range of 10^{-4} to 10^{-3}. This C_D was computed using observations made between March and September of 2016, the period with the highest subtidal zonal velocities in the record. The pressure measurements are made ~20 km north of the channel, making the gradient in sea level across the channel likely lower that that observed farther north. Comparison of the pressure differential in the model, both near the observation stations and directly adjacent to the channel, show a factor of two drop over this meridional spatial scale. Accounting for a reduction in the amplitude of the gradient close to the channel and large range in velocities experienced, does not change the computed drag coefficient beyond an order of magnitude.

The original scaling arguments done in 3.3.1 assumed a $C_D \sim 10^{-2}$. If the scaling is adjusted using a $C_D \sim 10^{-3} - 10^{-4}$ the advective terms can play an *O*(1) role in the balance. The acceleration term is also relevant if time scales of less than 1 day are being considered, as shown by the time lag between the pressure and friction terms. The correlation coefficients between Δη and $u_{channel}$, both in the observations and model, range from -0.52 to -0.79, leaving a portion of the variance in the zonal channel velocity unexplained. The relatively weak drag coefficient and the remaining variance unexplained by the pressure friction balance, suggests that other terms likely play an *O*(1) role in the balance.

3.4 Conclusion and Discussion

Our initial scaling of the x-momentum equation for the case of the channel flow around Hydrographer Bank predicted that the force balance would be dominated by the pressure and friction terms. Observations from the nearshore of Palau show that sea level varies coherently around the island group at subtidal frequencies, with amplitude differences on either side of the island suggestive of blocking of the large-scale flows by the island topography. The pressure gradient established by the east-west pressure differences in the southern region of Palau correlate with zonal flows through the channel between Angaur and Peleliu islands. The correlation suggests that a balance exists between the zonal sea level gradients and dissipation of the flow over the bank and through the channel.

A high resolution model simulation, nested in a regional state estimate, is used to characterize the spatial structure related to this mechanism over the course of a 1 month model run. Mean synoptic and composite fields show upstream sea level elevated around the topography corresponding to impinging flow, consistent with those found in the pressure observations. A local analysis of the pressure and flow fields across the channel show a consistent relationship between the $\Delta\eta$ computed zonally across the channel and the zonal channel flow, with a correlation coefficient of -0.55. A factor of two reduction is found in the $\Delta\eta$ computed zonally across the channel compared with the $\Delta\eta$ computed at the grid points close to the observation station farther north. Cross channel $\Delta\eta$ assessed in relation to the zonal flow in the channel, shows that the flows are not in local geostrophic balance.

The observed $\Delta\eta$ is shown to be related to the geostrophic flow fields at both the mesoscale scale, $O(100)$ km, and regional scale, $O(1000)$ km using altimetry derived products. Surface currents off of the east coast of Palau, observed by HR Radar systems maintained from the summer

2016 through the present, gave insight into what might drive the relationship between the local Δη, zonal channel flow and large scale fields during that time period. During the summer of 2016 the HF radar captured the reconnection of flows to the east of Palau, coincident in location with the maxima in the correlation between the channel flow and offshore geostrophic flows. This likely results due to the influence of the wake of Palau as the flow impinges on the island group from the west.

The assumed C_D was readdressed by comparing the observed pressure and friction terms of the x-momentum equation. This results in a C_D lower than initially assumed and lower than what would be required for pressure and friction to be the only dominant terms. Using the factor of two drop in pressure as seen in PALAU_120B from the near observation points to the channel would lead to a smaller C_D, but still on the order of 10^{-4}. We estimate a drag coefficient assuming that bottom friction balances the pressure gradient, but other acceleration terms likely are important as the flow moves in to a smaller cross-sectional area between islands. PALAU_120B also has a $C_D = 0.0025 \sim 10^3$, a factor of 2-5 higher than what was observed. The lower observed C_D could be due to their being depth of ~500 m to the north and south of Hydrographers Bank in the channel, limiting bottom drag at the depth of the observed flow. The time lag of ~7 hours between the pressure and drag terms as seen in PALAU_120B suggests that the acceleration terms likely play a role as the pressure gradient-bottom friction balance builds to an equilibrium state.

More generally, island topography alters impinging deep ocean flows by establishing anomalies in local sea level across the island. The model simulations suggest that the blocking effect alters the pressure field 5-10 km offshore (Figure 3.8a,c,d) which may have an associated influence on boundary currents (Figure 3.8a). The downstream impacts of the flow-topography

interaction are captured by the HF radar surface currents, which show that the relationship between the channel flow and the unimpeded offshore flows extend at least 100 km offshore.

The upstream scales of high pressure anomaly induced by the topography can have longer spatial scales than the channels or gaps between islands, forcing a hydraulic-like response in the channels. The channels act as a leaky boundary that sees a pressure head built around the topographically blocked flow. These scales are relevant when attempting to predict responses of nearshore flow to large scale flow fields and sea level variability.

Downscaling efforts, as have been made here with PALAU_120B nested in a coarser state estimate, when coupled with in situ observations give insight into how these scales interact. In coarser state estimates, which are becoming more common with the proliferation of observations and computational capabilities, channels such as the one studied here are still poorly resolved or not resolved at all. This leads to the question of how one might infer what the channel flow would be from the models of this scale. Our work here shows that local pressure gradients likely play a large role in driving flow. But an examination of the drag coefficient made with in situ observations suggests that the advective and acceleration terms likely play a role in balancing the flow in the channel at different time scales. Further observational campaigns, coupled with high resolution modeling efforts, are needed to better understand the dynamics that operate at these temporal and spatial scales.

3.5 Acknowledgements

We are thankful for the efforts of the staff from the Coastal Research and Development Center at the Scripps Institution of Oceanography, including J. S. Scott, and M. Jilka, who helped with the implementation for both the current meter and water level data collection and T. Cook, M. Syverud, and C. Garcia-Moreno for their efforts in both collecting, processing and visualizing

the HF Radar data. The State Estimate used for the model nest was run by B Powell and S Zedler at the University of Hawaii at Manoa and was an appreciated effort incorporating a wide range of efforts on the FLEAT DRI. We thank the staff at the Coral Reef Research Foundation for their assistance with this work in Palau. This work was funded by the Office of Naval Research under the FLEAT DRI (Grant Number N000141512304).

Chapter 3, in part is currently being prepared for submission for publication of the material. Schramek, Travis A.; Merrifield, Mark A.; Colin, Patrick L.; Simmons, Harper; Merrifield, Sophia; Terrill, Eric J. The dissertation author was the primary investigator and author of this material.

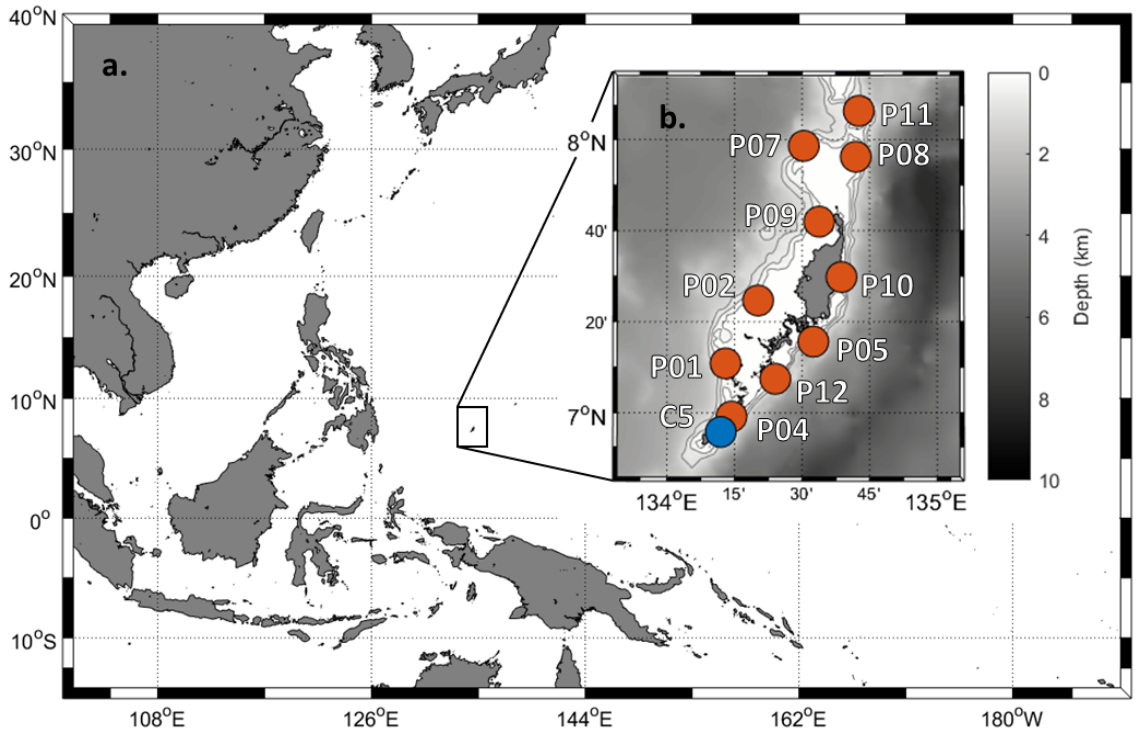

Figure 3.1: **a.** Palau is located in the tropical western Pacific at 7.5°N and 134.5°E, north of Papua New Guinea and east of the Philippines. **b.** The locations of the observation stations maintained by pressure loggers (P* - orange circles) and a current meter (C* - blue circle) on the fore reefs of Palau between March 2014 and June 2018 are shown. Contours of 100 m, 500 m, and 1000 m are displayed as solid gray lines.

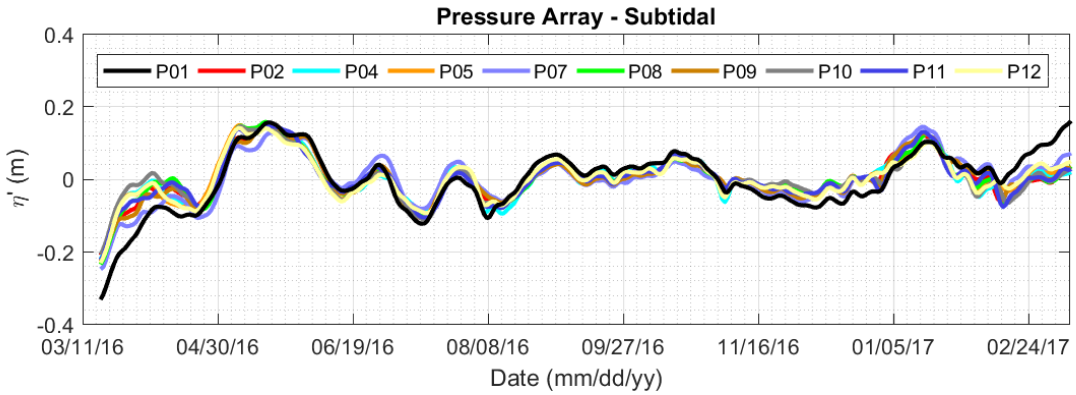

Figure 3.2*:* Subtidal water level, derived from observations of in situ bottom pressure between 20 and 28 m of water depth of the fore reefs encircling the major barrier reef of Palau. The mean water level over the course of the deployment, from March 2016 through March 2017, at each station has been removed from each record. The pressure logger at P01 had a drift that started in August 2016.

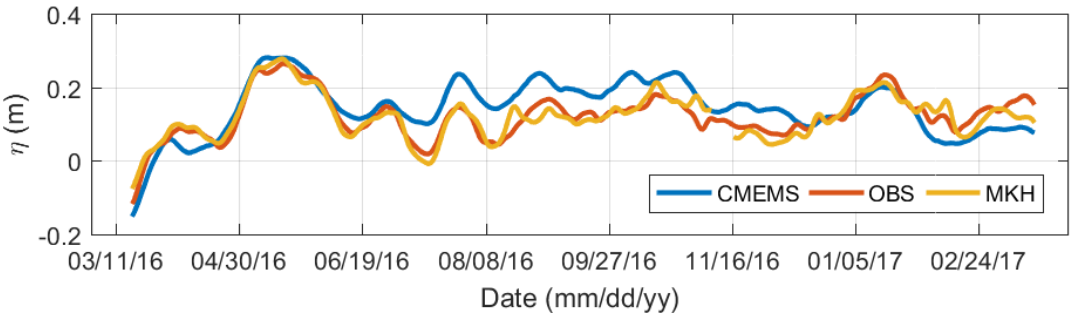

Figure 3.3*:* Mean sea level anomaly, computed using the observations of pressure from Palau's fore reefs (OBS - orange line), shown in Figure 3.2, is shown in comparison to the NOAA tide gauge station located in Malakal Harbor (MKH - gold line) and the CMEMS grid point of sea level located nearest to the MKH station (blue line) from March 2016 through March 2017. All data has been filtered to maintain subtidal signal.

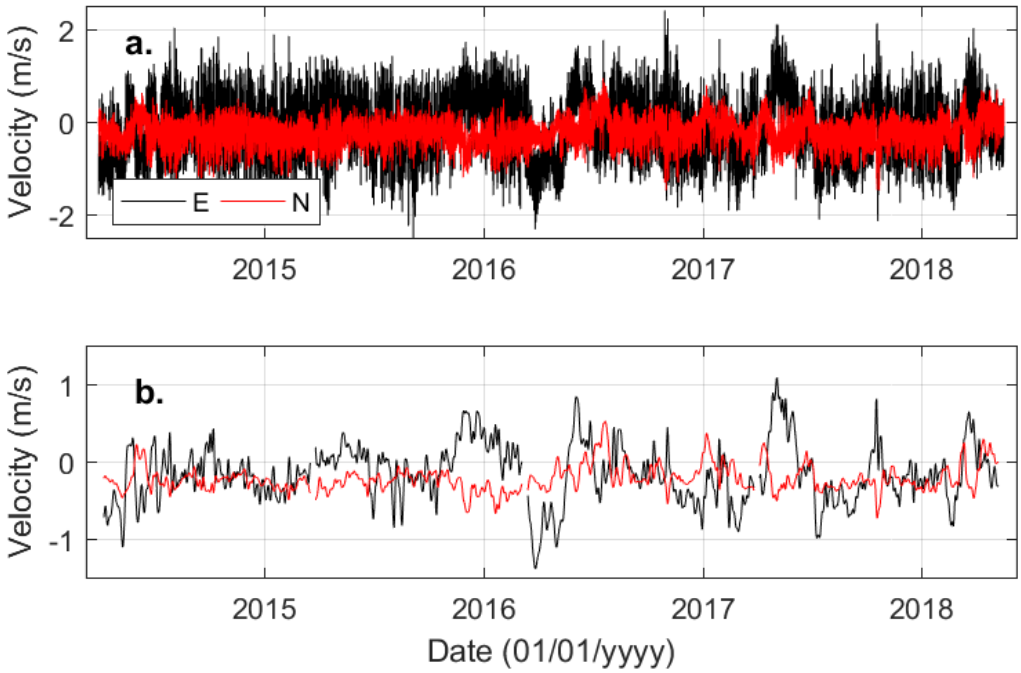

Figure 3.4*:* **a**. Depth averaged East (black) and North (red) current vectors shown between March 2014 and June 2018. **b**. Subtidal depth averaged current vectors show the subtidal signals observed through the 4-year observational record.

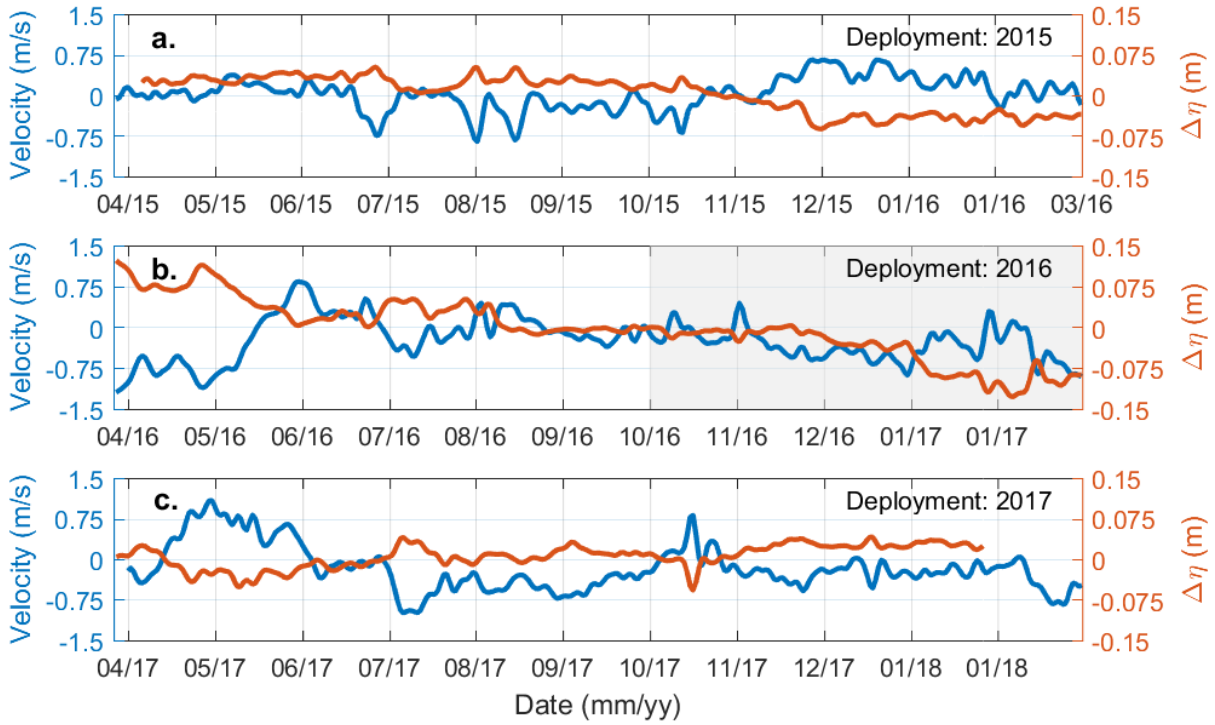

Figure 3.5*:* The relationships between the observed zonal flow through the channel (blue lines, left y-axes) and the differences in sea surface height, denoted as Δη, across the island (orange lines, right y-axes) is examined. Pressure records from P01 (west) and P12 (east) were used for this computation, which are the two stations both at similar latitudes and nearest the channel. Each deployment is displayed separately as a different subplot, as noted in the upper right hand corner of the plot. Correlation coefficients for the each of the successive deployments between the two plotted variables are -0.66, -0.79, and -0.77 for March 2015 to March 2016, March to September 2016, March 2017 to March 2018 deployments, respectively. The data for the period of October 2016 through March 2017 is displayed with a gray background and has been ignored for the computation of the correlation coefficient for that deployment. The pressure logger at P01 had a drift that started in October 2016, leading to its exclusion from statistical assessment.

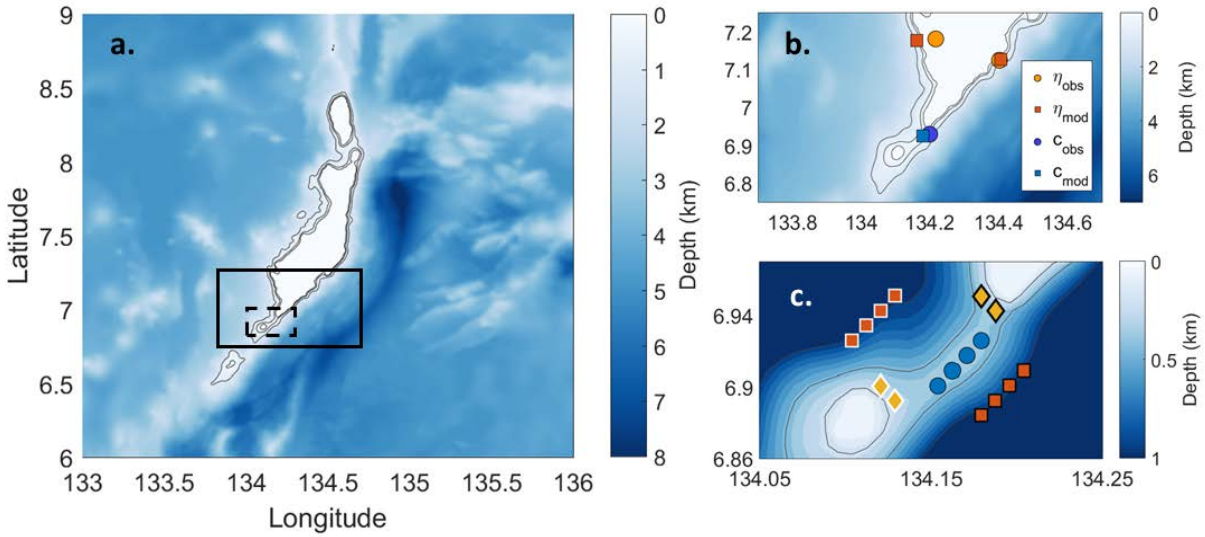

Figure 3.6: **a.** The full model domain is displayed for the ROMS run PALAU_120B, where the subdomains displayed in (b) and (c) are designated by the solid and dashed black lines, respectively. Contours are displayed for the 250 m, 500 m, and 1000 m isobaths with thick black lines. **b.** The southern extent of Palau in the model domain is shown with the observation points (circles) of pressure (gold) and currents (dark blue) are shown along with the closest model grid points (squares) that were used to compare η (orange) and currents (light blue). **c.** The subdomain directly around the channel in the southern extent of Palau is shown with a depth range of 0 m to 1 km shown with color breaks at every 100 m. Contours at 250 m and 500 m of depth are shown with thin black lines. Model grid points used to compute η computation are shown.

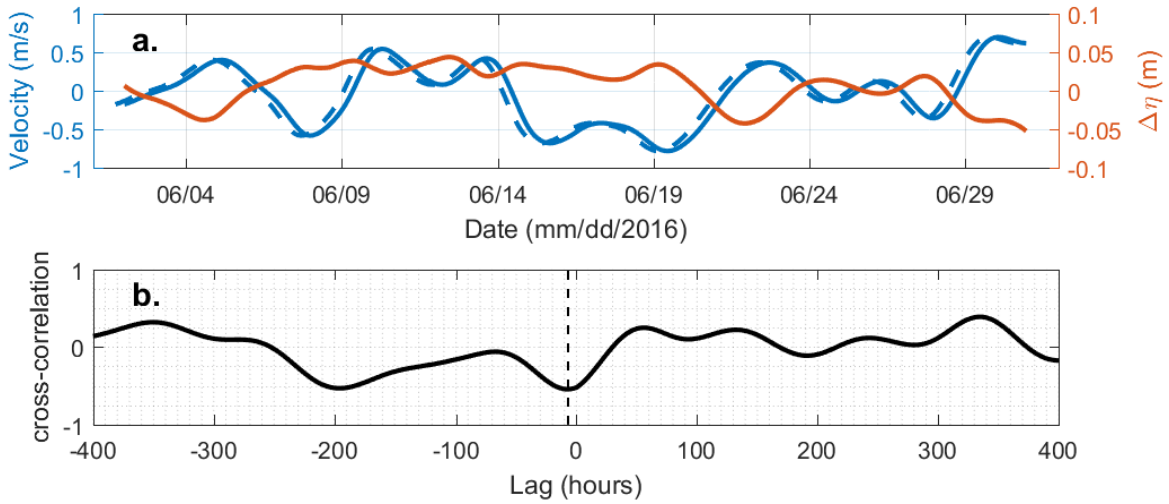

Figure 3.7: **a.** The relationships between the modeled zonal flow through the channel (blue solid line, left y-axes) and the differences in sea surface height across the island (orange line, right y-axes), shown as Δη, is examined. Velocities were taken from the grid points noted in Figure 3.6b by a blue circle. Pressure was taken at the grid points noted in Figure 3.6b by orange squares. The correlation coefficient between Δη and $u_{channel}$ at 0 lag is -0.52. **b.** Time lagged cross correlations showed a peak in correlation at a lag of 7 hours (noted with a vertical dashed line), where Δη lead $u_{channel}$, increasing the correlation from -0.52 to -0.54. The $u_{channel}$ time series has been shifted ahead by +7 hours in (a) with a dashed blue line.

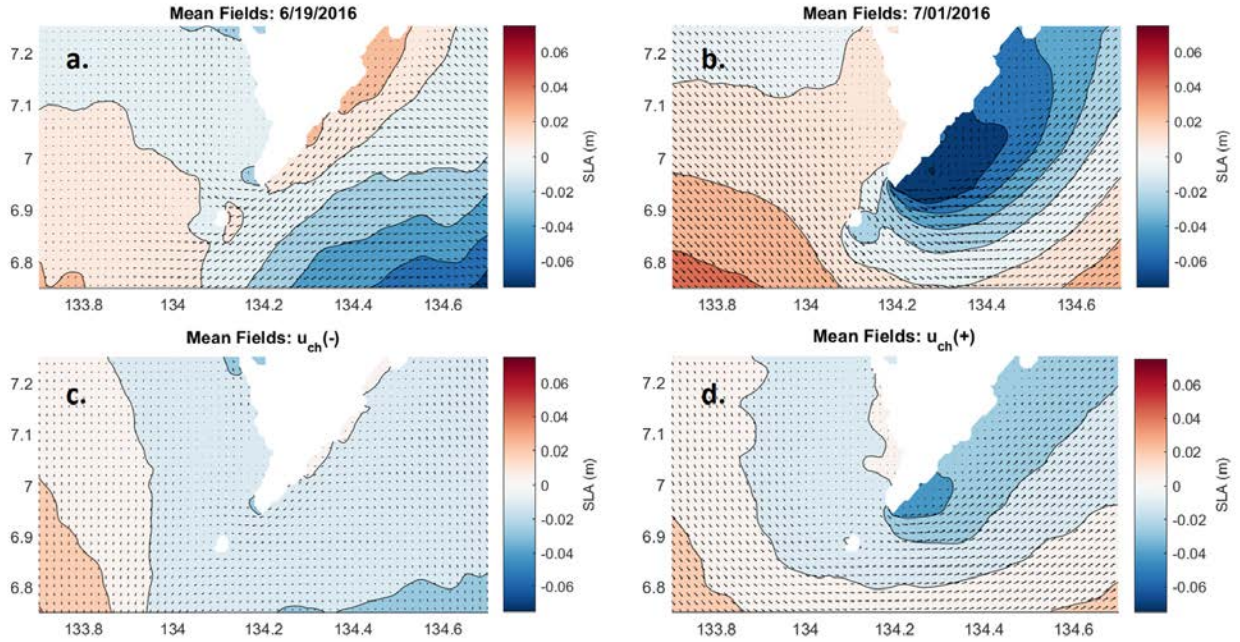

Figure 3.8*:* Daily mean output for (**a**) June 19th, 2016 and (**b**) July 1st, 2016 in the ROMS model run, denoted as Palau_120B, with 1/120° x 1/120° resolution is shown. Currents vectors, which are subsampled for display purposes, are shown as arrows, overlaid on sea level, where the spatial mean of the sea level in the visualized subdomain has been removed. A positive sea level anomaly can be seen on upstream coast of Palau for both days. The near-coast sea level anomaly and along coast flow has an offshore scale of ~10 km for June 19th. Composite fields were made for periods when the channel velocity was (**c**) negative, flowing westward and (**d**) positive, flowing eastward, based off of the velocity time series in Figure 3.7. The output form June 9 – June 14 has been ignored for the computation of these composites.

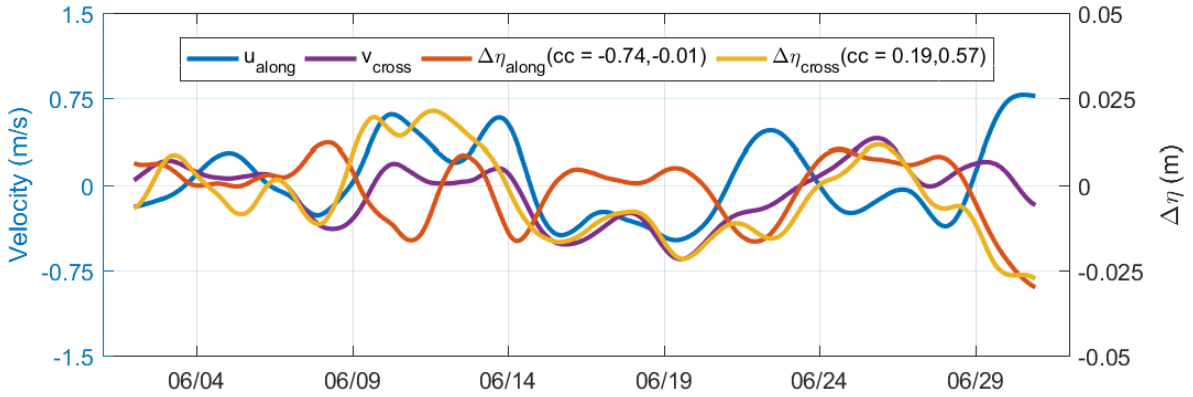

Figure 3.9*:* The relationships between the modeled along- and cross-channel flow (blue and purple lines, left y-axes) and differences in sea surface height (orange and gold lines, right y-axes), shown as $\Delta\eta$, is examined. Velocities were taken from the grid points noted in Figure 3.6c by blue circles and a mean was computed. The velocity values were rotated 35.74° clockwise from N so the u and v components were along- and cross-channel. Sea surface height was taken at the grid points noted in Figure 3.6c by orange squares for $\Delta\eta_{along}$ and gold diamonds for $\Delta\eta_{cross}$. Correlation coefficients between the pressure differences and the along and cross channel velocities are noted in the legend, in that respective order.

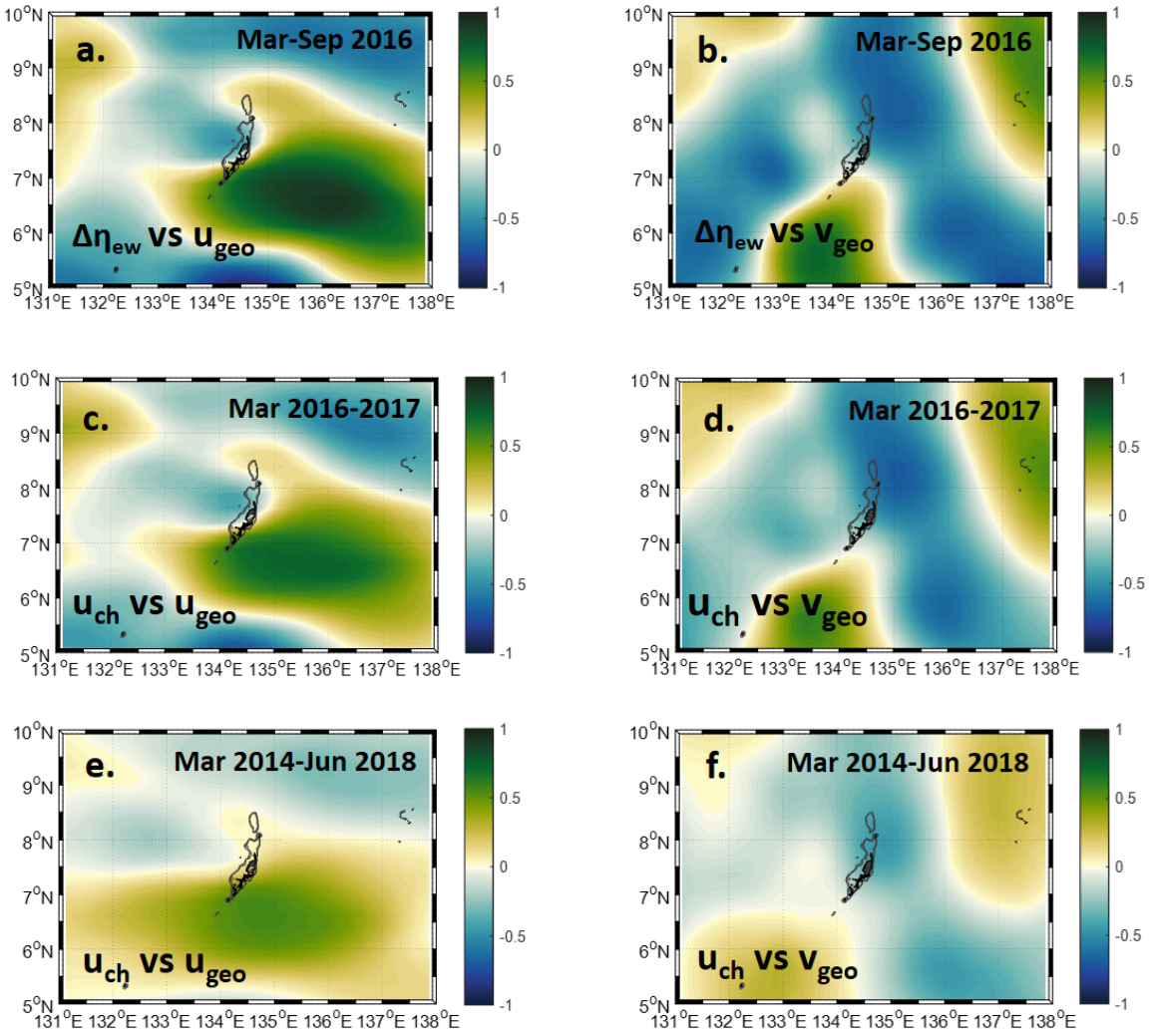

***Figure 3.10**:* Correlation coefficients computed between the observed zonal pressure gradient, Δη, (a, b), as shown in Figure 3.5b between March and September 2016, and the CMEMS geostrophic velocity output in both the u (left column) and v (right column). Correlation coefficients were also computed between the zonal velocity observed in channel and the CMEMS geostrophic velocity output in both the u (left) and v (right) over the period of March 2016 to March 2017 (c, d) and over the full observational record (e, f) from March 2016 to June 2018, as noted in the upper right corner of the subplots.

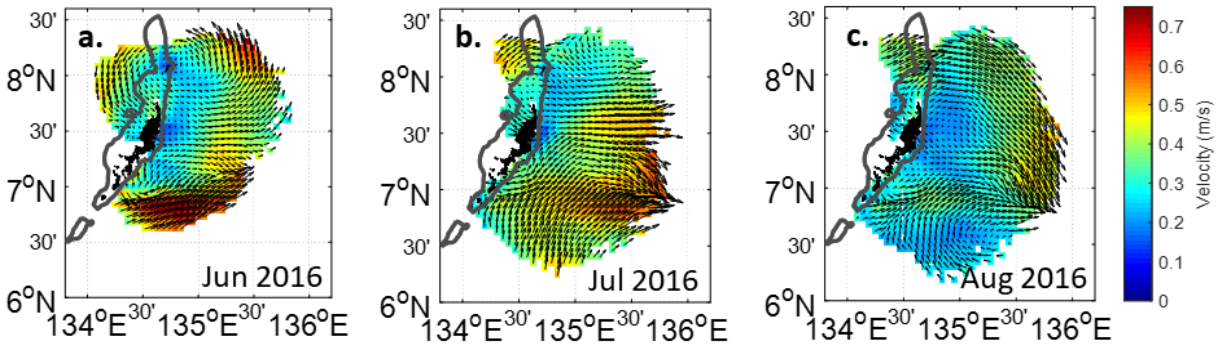

Figure 3.11*:* Monthly mean surface currents as observed by HF Radar off of the east coast of Palau during (a) June, (b) July, and (c) August 2016. Vectors show the direction of the flow and are auto scaled. Magnitude is shown by color.

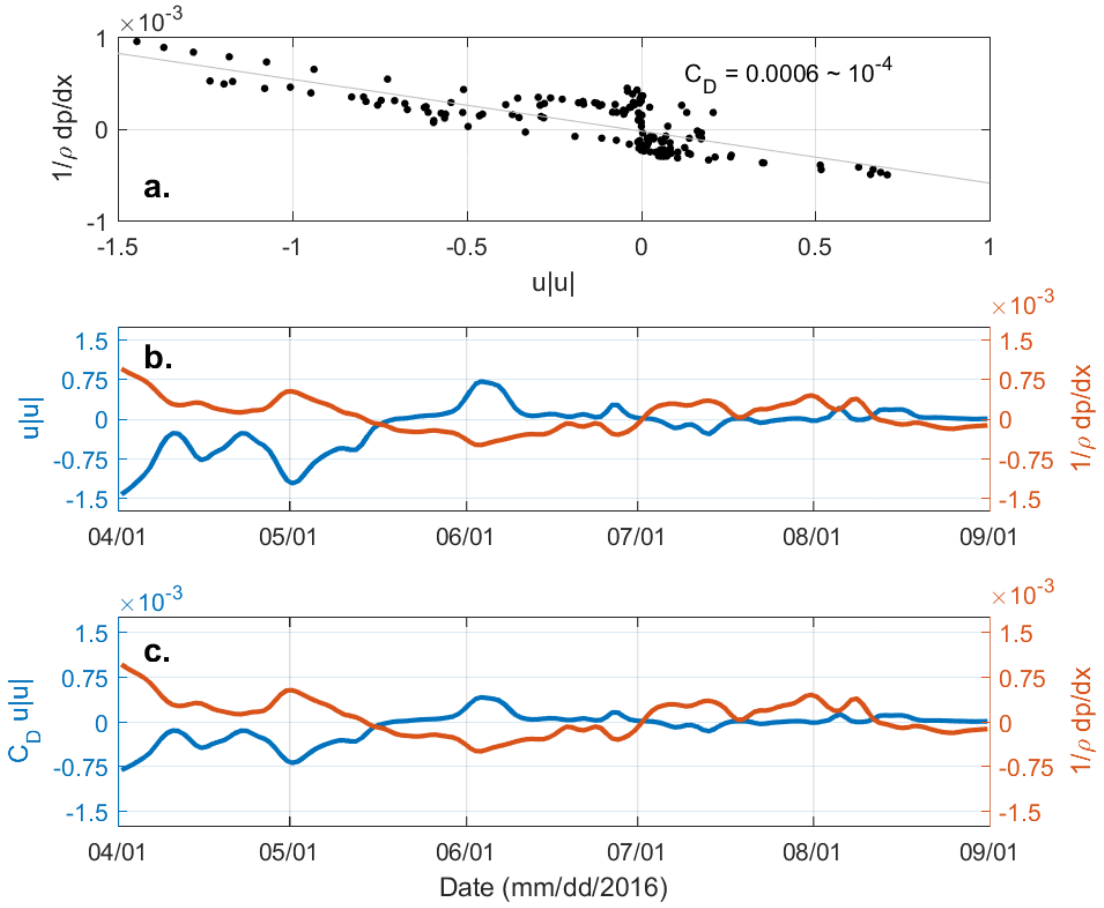

Figure 3.12: **a.** Equating the pressure term (y-axis) and friction term (x-axis), excluding the drag coefficient, allows the fitting of a slope to obtain a drag coefficient that relates the two terms. The slope for the linear fit between the two terms is noted in the figure as $C_D = 0.0009 \sim 10^{-4}$. **b.** The unscaled friction term (left – blue) is shown against the pressure gradient term (right – orange). **c.** The full friction term with the C_D solved for in (a) shown again the pressure gradient term as in (b).

3.6 References

Alford, M. H. (2003). Redistribution of energy available for ocean mixing by long-range propagation of internal waves. *Nature*, *423*(March), 159–162. https://doi.org/10.1038/nature01628

Becker, J. M., Merrifield, M. A., & Ford, M. (2014). Water level effects on breaking wave setup for Pacific Island fringing reefs. *Journal of Geophysical Research: Oceans*, *119*(2), 914–932. https://doi.org/10.1002/2013JC009373

Caldwell, P. C., Merrifield, M. A., & Thompson, P. R. (2017). Sea level measured by tide gauges from global oceans as part of the Joint Archive for Sea Level (JASL) from 1846-01-01 to 2015-07-31. *National Oceanographic Data Center, NOAA.* https://doi.org/10.7289/V5V40S7W

Dong, C., McWilliams, J. C., & Shchepetkin, A. F. (2007). Island Wakes in Deep Water. *Journal of Physical Oceanography*, *37*(4), 962–981. https://doi.org/10.1175/JPO3047.1

Gove, J. M., Merrifield, M. A., & Brainard, R. E. (2006). Temporal variability of current-driven upwelling at Jarvis Island. *Journal of Geophysical Research: Oceans*, *111*(C12), 1–10. https://doi.org/10.1029/2005JC003161

Leichter, J. J., Stokes, M. D., Hench, J. L., Witting, J., & Washburn, L. (2012). The island-scale internal wave climate of Moorea, French Polynesia. *Journal of Geophysical Research*, *117*(C6), C06008. https://doi.org/10.1029/2012JC007949

Lowe, R. J., & Falter, J. L. (2015). Oceanic Forcing of Coral Reefs. *Annual Review of Marine Science*, *7*(1), 43–66. https://doi.org/10.1146/annurev-marine-010814-015834

Nikurashin, M., & Ferrari, R. (2011). Global energy conversion rate from geostrophic flows into internal lee waves in the deep ocean. *Geophysical Research Letters*, *38*(8). https://doi.org/10.1029/2011GL046576

Pawlowicz, R., Beardsley, B., & Lentz, S. (2002). Classical tidal harmonic analysis including error estimates in MATLAB using T_TIDE. *Computers & Geosciences*, *28*(8), 929–937. https://doi.org/10.1016/S0098-3004(02)00013-4

Roemmich, D. (1984). Indirect Sensing of Equatorial Currents by Means of Island Pressure Measurements. *Journal of Physical Oceanography*, *14*(9), 1458–1469. https://doi.org/10.1175/1520-0485(1984)014<1458:ISOECB>2.0.CO;2

Ruessink, B. G., Miles, J. R., Feddersen, F., Guza, R. T., & Elgar, S. (2001). Modeling the alongshore current on barred beaches. *Journal of Geophysical Research: Oceans*, *106*(C10), 22451–22463. https://doi.org/10.1029/2000JC000766

Shchepetkin, A. F., & McWilliams, J. C. (2005). The regional oceanic modeling system (ROMS): a split-explicit, free-surface, topography-following-coordinate oceanic model. *Ocean Modelling*, *9*(4), 347–404. https://doi.org/10.1016/j.ocemod.2004.08.002

Smith, K. A., Rocheleau, G., Merrifield, M. A., Jaramillo, S., & Pawlak, G. (2016). Temperature variability caused by internal tides in the coral reef ecosystem of Hanauma bay, Hawai‘i. *Continental Shelf Research*, *116*, 1–12. https://doi.org/10.1016/j.csr.2016.01.004

Ulloa, H. N., Davis, K. A., Monismith, S. G., & Pawlak, G. (2018). Temporal Variability in Thermally Driven Cross-Shore Exchange: The Role of Semidiurnal Tides. *Journal of Physical Oceanography*, *48*(7), 1513–1531. https://doi.org/10.1175/JPO-D-17-0257.1

Wolanski, E., Colin, P., Naithani, J., Deleersnijder, E., & Golbuu, Y. (2004). Large amplitude, leaky, island-generated, internal waves around Palau, Micronesia. *Estuarine, Coastal and Shelf Science*, *60*(4), 705–716. https://doi.org/10.1016/j.ecss.2004.03.009

Chapter 4:

The role of the surface and internal tides in driving flow on the edge of an island

Surface and internal tides can be a dominant source of nearshore current variability around island groups. Flows through a channel (~10 km wide in the cross-channel and ~1 km in the along-channel) at the southern extent of the main island group of Palau were observed to be over 2 m/s and tidally modulated with a large degree of uncertainty in their phase relationship with the barotropic component of the tides. Amplitudes of the tidal band currents (M2 and K1) exceeded predictions based upon long term harmonic decomposition of the observations, indicative of the presence of internal tides. Phase relationships between these flows and the surface tide, as tracked by local sea surface height, were not locked and varied in time. These internal tide signals are indicative of a dominant forcing mechanism at this frequency band. Analysis of the phase relationship with other forcing variables indicates that the variability may be driven both locally and from remote sources, complicating the ability to derive prediction of currents within this frequency band. We hypothesize that the local stratification plays a role in both local tide generation, and in supporting the waveguide that allows for remotely generated internal tide signals to propagate into the region of observation.

4.1 Introduction

The surface tide is a dominant feature of nearshore island circulation driving lagoon flushing (Dumas et al., 2012) and modulating wave setup induced flows (Symonds et al., 1995) by controlling water depths over reef flats. Coastal currents and water level variability around islands are influenced by the barotropic tide (Wolanski et al., 1984). Baroclinic tides can be both generated

and dissipated at island groups (Eich, 2004; Nagai & Hibiya, 2015). Coastal circulation can be driven by these internal tides, which are at times incoherent with the surface tide (Zilberman et al., 2011).

While our ability to map the surface tide using satellite altimetry (Egbert et al., 1994; Egbert & Ray, 2001) has become a routine observational tool, internal tides remain an elusive phenomena to map and predict with any fidelity of their phase relationship with the surface tide (Chavanne et al., 2010; Ray & Zaron, 2011). Internal tides are generated at sites of rough topography across the world's oceans, converting energy from barotropic to baroclinic modes (Simmons et al., 2004). These internal waves are often generated and dissipated at different locations, sometimes propagating freely to meet their fate far from their generation site (Alford, 2003). The interaction of the barotropic tide with topography results in non-linear interactions diagnosable by a broadening of the spectral responds around the tidal bands (Munk et al., 1965; Munk & Cartwright, 1966).

The island nation of Palau sits in the tropical western Pacific and extends from 1 to 6 degrees latitude (Figure 1.a), with the main island group centered at 7°N and 134.5°E (Figure 1.b). Two major internal tide generation sites in the western Pacific basin, Luzon Straight and the eastern Celebes Sea, both to the west of Palau (Figure 1.a). Nearshore oceanographic conditions on the fore reefs of Palau have been shown to have highly active internal wave component (Colin, 2009; Wolanski et al., 2004) with excitation at the tidal bands. Observations in of in-situ pressure, temperature, and currents were taken from March 2014 through June of 2018 on Palau's fore reef slopes to better understand the role of the surface and internal tide in driving nearshore variability.

This chapter will describe: observations of the tidal flows in the southern extent of the main island group of Palau and their temporal variability (4.3.1); an analysis that illustrates the temporal variation of the amplitude and phasing of the tidal currents and lack of coupling to the local barotropic surface tide (4.3.2); and finally a description of how stratification might play a role in facilitating the influence of the internal tides on nearshore variability (4.3.3). A conclusion and discussion follow (4.4).

4.2 Data and Methods

4.2.1 Observational array

Currents were measured with a bottom mounted, upward looking TRDI Workhorse Acoustic Doppler Current Profiler (ADCP) at a single location on Hydrographers Bank at 6.9°N, 134.3°E at 20 m depth (Figure 1.b&c, blue circle). Both 300 kHz and 600 kHz ADCPs were used to maintain this station between March 2014 and June 2018. Sea level was also observed by this ADCP. Daily tide gauge records were obtained from Malakal Harbor station from 2014 through 2018, maintained by the University of Hawaii Sea Level Center (Figure 1.b, red circle, http://uhslc.soest.hawaii.edu/data/;Caldwell et al., 2017).

In-situ temperature at the seafloor was collected by CRRF at 7 depth stations at West Channel in Palau at depths ranging from 2 - 65 m (Figure 1.b, yellow circle). Seabird Scientific SBE 56s were used with sampling intervals ranged from 30 seconds to 30 minutes. The observational campaign with the thermographs began in 2000 and is ongoing at the time of publication.

4.2.2 Statistical techniques

Godin filters were applied to remove high frequency variability from the observations of current (Godin, 1972) while maintaining signals with period longer than 1.25 days, thus removing

tidal signals. The relevance of individual tidal constituents were examined using t_tide (Pawlowicz et al., 2002). Hilbert transforms were used to compute the envelope function of the signal and assess the amplitude of the tidal band energy beyond the daily time scale. This was done after band pass filtering around the desired tidal bands was performed on the time series. Wavelet coherence analysis was done using the Matlab wavelet toolbox (Daubechies et al., 2011).

4.3 Results

4.3.1 Characteristics of the flow field

Large amplitude tidal currents were observed in the channel over Hydrographers Bank (Figure 4.2 Top). The magnitudes of depth-averaged currents were observed to exceed 2 m/s in the time series made up of 12-minute ensemble means. These maxima in current magnitude occurred at multiple times of the year over the course of the four-year record, which spanned from March 2014 through June 2018. Currents were polarized in the east-west direction (Figure 4.2). This polarization matches the orientation of the channel in which the ADCP was stationed. Rotary spectra of the signal showed energy in the inertial band, as well as signatures of the diurnal and semi diurnal tides (Figure 4.3). The bandwidth of the excitation around the K1 and M2 tidal bands is not insignificant, likely due to non-linear interactions of the tides with the coastal topography (Munk et al., 1965; Munk & Cartwright, 1966). Energy in the tidal harmonics was also elevated (Figure 4.3) as was seen in the spectra of the sea surface height as observed by the ADCP pressure gauge (Figure 4.4).

4.3.2 Evidence of an internal tide in the tidal currents

Temporal variability of the magnitude of the tidal component computed with a 30 day window is present in time series of the frequency spectrum of the east and north depth-averaged

currents (Figure 4.5). A narrow-band response is seen around both the diurnal and semi diurnal frequencies (Figure 4.5, dash and dash-dot lines). The barotropic surface tide accounted for 35.1, 24.3, 39.7, and 37.7 percent of the annual variance predicted in relation to the total variance in the depth-averaged records for each of the four 12 month deployments starting in March of 2014, 2015, 2016, and 2017, respectively. The Matlab package t_tide (Pawlowicz et al., 2002) was used for this analysis. The influence of the baroclinic internal tide and its varying phase relationships were not accounted for in these percentages. Flow over the bank was observed to have little shear between the sensor location at ~20 m and the surface. The lack of shear argues for the use of the depth average to be an accurate representation of the flow field across the bank for further tidal decomposition analysis. Harmonic decomposition (t_tide) cannot distinguish between the baroclinic and barotropic components that drive the flow, and thus the internal tidal component is not contained in the estimate of the percentage of variance explained as it isn't phase locked with the surface component, and found to undergo phase changes on time scales of $O(5)$ days.

The amplitude of the currents in the diurnal and semidiurnal bands change throughout the record (Figure 4.6, red lines). Band pass filtered sea level observed in Malakal Harbor, the central lagoon system on Palau, shows temporal modulation consistent with a spring neap cycle (Figure 4.6, black lines) and has been shown elsewhere to be consistent with global tidal predictions (Mitchum, 1994) . Sustained periods of elevated current amplitudes in both K1 and M2 bands last for upwards of 1 month, but do not consistently modulate with the amplitudes of the surface tide in each respective band as observed in the tide gauge in Malakal Harbor (Figure 4.6, red lines).

The amplitude of observed tidal currents in the diurnal and semidiurnal bands were typically larger than the t_tide predicted tidal currents (Figure 4.7, Top), as generated using one

year of observed currents between March 2014 and March 2015 in t_tide. Observed currents were high passed, maintaining all periods shorter than 2 days. Elevated energy in each tidal band (Figure 4.7 middle, bottom) is indicative of the internal tides driving local flows.

The phase relationship between the surface tide and depth-averaged currents changes throughout the record. A current driven by the hydrostatic control of a surface tide will be 90 degrees out of phase with the sea level response. In contrast, at our observation site, the diurnal and semidiurnal bands of tidal currents exhibit phase relationships that vary between 0 and 180 degrees (Figure 4.8), all within the span of one month. Elevated levels of coherence are seen at the semidiurnal and diurnal bands as seen through wavelet coherence between the surface tide, represented by the SLA observed by the ADCP pressure sensor, and major axis velocity in the semidiurnal and diurnal bands between March 2014 and March 2015 (Figure 4.9). While a relationship between the coherence of the surface tide and observed tidal currents verses the amplitude of the observed tidal currents is present (Figure 4.10, left column), there is no clear relationship between the amplitude of the coherence of the surface tide and observed tidal currents versus the predicted tide (Figure 4.10, right column).

Wavelet coherence between sea level and the tidal band currents was compared to the amplitude of the tidal band currents, as shown in Figure 4.7. A relationship between the coherence of the sea level and tidal currents and amplitude of the observed tidal currents is apparent for both the semidiurnal and diurnal bands (Figure 4.11, left column). The amplitudes of the predicted tidal currents does not show the same relationship (Figure 4.11, right column).

4.3.3 The role of stratification

The depth structure of temperature seen on Palau's fore reefs was examined during periods when the correlation between the barotropic surface tide and observed currents were positive, negative, and not correlated. West Channel, on the west coast of Palau, is roughly 75 km from Hydrographers Bank and is the location of the thermograph array used for this comparison. The thermocline was located at the depth of our array for time windows when the surface tide and tidal currents were both positively (Figure 4.12) and negatively correlated (Figure 4.13). The thermocline was shallowest for this comparison during the period with a negative correlation. The thermocline was found to be deeper in the time period where the surface tide and the tidal currents showed little correlation Figure 4.14).

4.4 Conclusion and Discussion

Tidal flows in excess of 2 m/s were observed in the channel over Hydrographers Bank in the southern extent of Palau over the course of observations collected between 2014 and 2018. Temporal variability in tidal flows, both in amplitude and phase, were inconsistent with those of predicted tidal flows using t_tide indicating strong interactions, perhaps advective. Depth-averaged flows were analyzed for their influence by internal tide signals as the flow field over the bank had little shear. The amplitude of the tidal currents were found to change over time, but were not consistently related to the spring-neap cycle of the local sea level anomaly. Amplitude of the tidal currents are large compared to the t_tide prediction. We hypothesize that this is driven by internal tides, but are not able to make the distinction of that influence resulting from local or remotely generated internal tides. The phase relationship between surface tide and depth-averaged currents varies in time, possibly due to the influence of both remote and locally generated internal tides influencing the site. Coherence of SLA and flow over Hydrographers Bank in both the

semidiurnal and diurnal bands seem to be related to the amplitude of the tidal currents seen in the observations, while are seemingly unrelated to the temporal modulation of the predicted currents.

The depth of the thermocline varies from 10 to over 90 m in Palau on an interannual timescale (Schramek et al., 2018). The associated stratification can dictate the nearshore response to a remotely generated internal tide, and also aid in the local generation of internal tides. It is unclear from this analysis if the stratification is dictating a local response in internal tidal generation, but it prompts the question, is this channel in the southern extent of Palau an internal tide generation site? Elevated levels of energy in the tidal bands suggest this is a possibility. Multiple locations to the west of Palau, such as Luzon Straight and the Celebes Sea, are remote generation sites which could be influencing the local variability in Palau. Rays from these sites have been shown in numerical models to be directed towards our observation site (Simmons et al., 2004).

A challenge to addressing the problem observationally is the range of scales. At the local level, tides can induce baroclinic variability if the right combination of stratification, topographic, and background flow are present. Model grid resolution of at least 2.5 km is needed to resolve a 10 km wide channel, as in the channel described here, to allow for grid points to cover channel boundaries and allow for multiple grid points within the channel. This grid resolution would be required to resolve any cross-channel variability. Properly resolving topographic slopes, which in the case of Palau go from 8000 m to 20 m of depth in less than 40 km, is also of concern if local generation is to be properly simulated. Properly resolving similar topographic features only allows for the assessment of locally generated internal tides. This level of resolution must be coupled with full-physics models that encompass possible remote generation site at distances of $O(1000)$ km

away, running with tides. Outside the scope of this study would be the development of a numerical model that possesses the required resolution and spatial domain to simulate both local and remote sourcing to the observed signal within the study region.

4.5 Acknowledgements

We are thankful for the efforts of the staff from the Coastal Research and Development Center at the Scripps Institution of Oceanography, including S Scott, and M Jilka who assisted in the preparation and implementation for the current meter data collection. We thank the staff at the Coral Reef Research Foundation for their assistance with this work. This work was funded by the Office of Naval Research under the FLEAT DRI (Grant Number N000141512304).

Chapter 4, is coauthored by Merrifield, Mark A.; Colin, Patrick L.; Terrill, Eric J. The dissertation author was the primary investigator and author of this material.

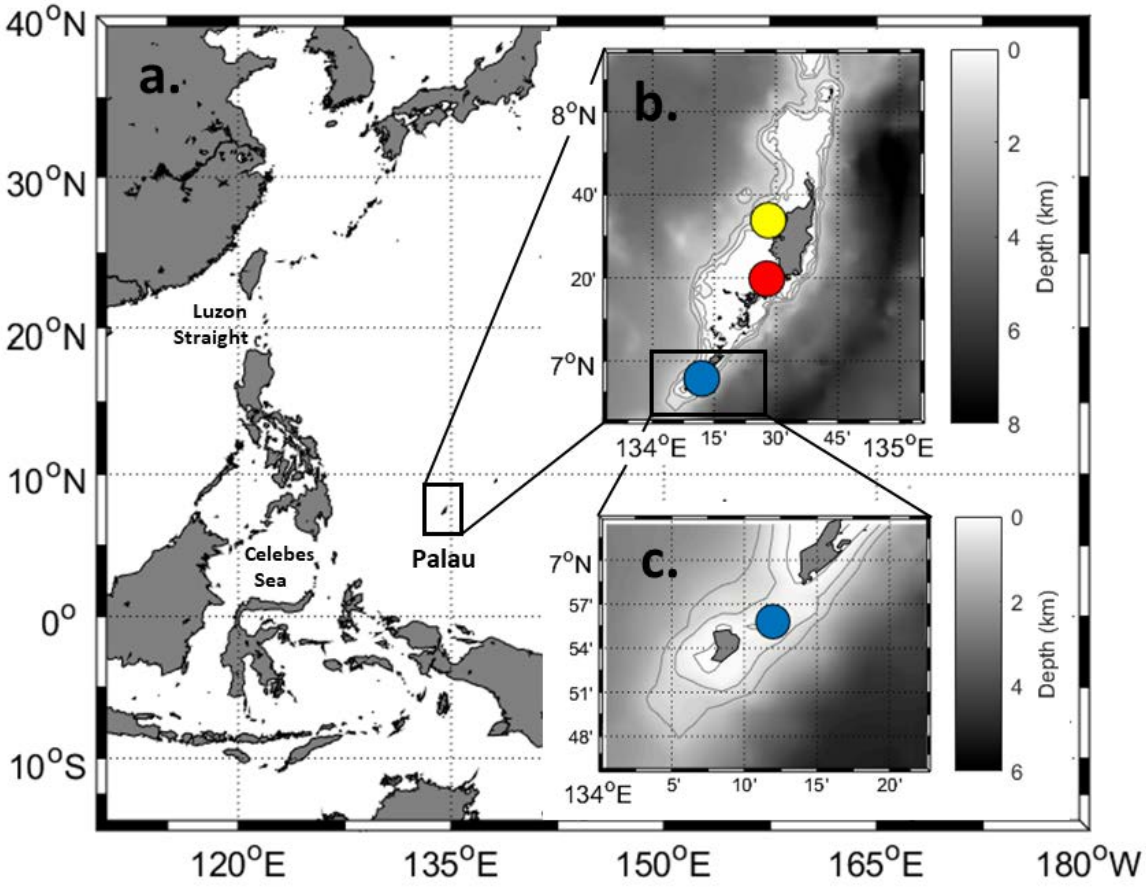

Figure 4.1: **a**. Regional map of the western tropical Pacific with a black box denoting the region around the island nation of Palau, as depicted in b. **b**. Palau is shown with gray contours denoting th 100, 500 and 1000 m isobaths. The locations of the acoustic Doppler current profiler (blue circle), UH tide gauge station in Malakal Harbor (red circle) and West Channel bottom mounted temperature array (yellow circle) are shown. **c**. The channel between Peleliu (north) and Angaur (south) islands is shown with the location of the ADCP denoted by a blue circle. The 100, 500 and 1000 m contours are shown in the same color. The depth range shown with the colormap in (b) is 0-8 km, and is 0-6 km in (c).

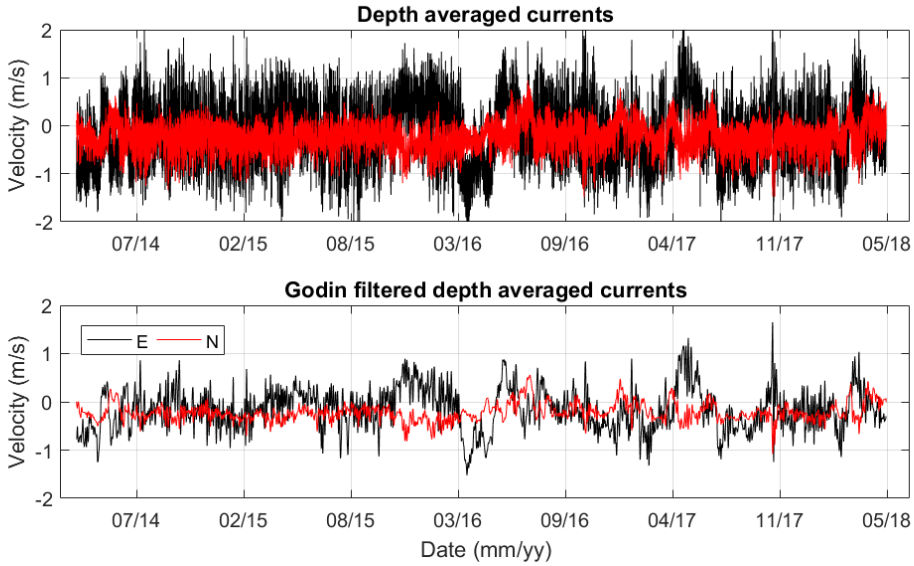

***Figure 4.2**:* **Top**. Depth-averaged East (black) and North (red) current vectors shown between March 2014 and June 2018. **Bottom**. Godin filtered depth-averaged current vectors show the subtidal frequency signals observed through the 4-year observational record.

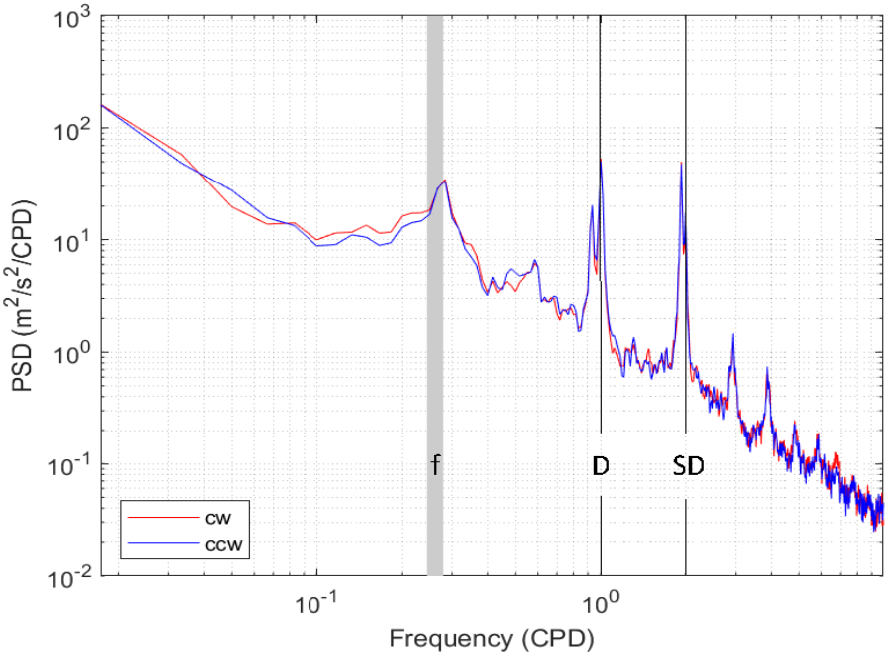

***Figure 4.3**:* Rotary spectra of the depth-averaged currents between Mar2014-Jun2017. There is elevated energy in the dirnal (D) and semidiurnal (SD) tidal bands as well as their harmonics. Broadband excitation is seen around the inertial band denoted by the gray vertical band. Additional energy is seen in the ~2 day band.

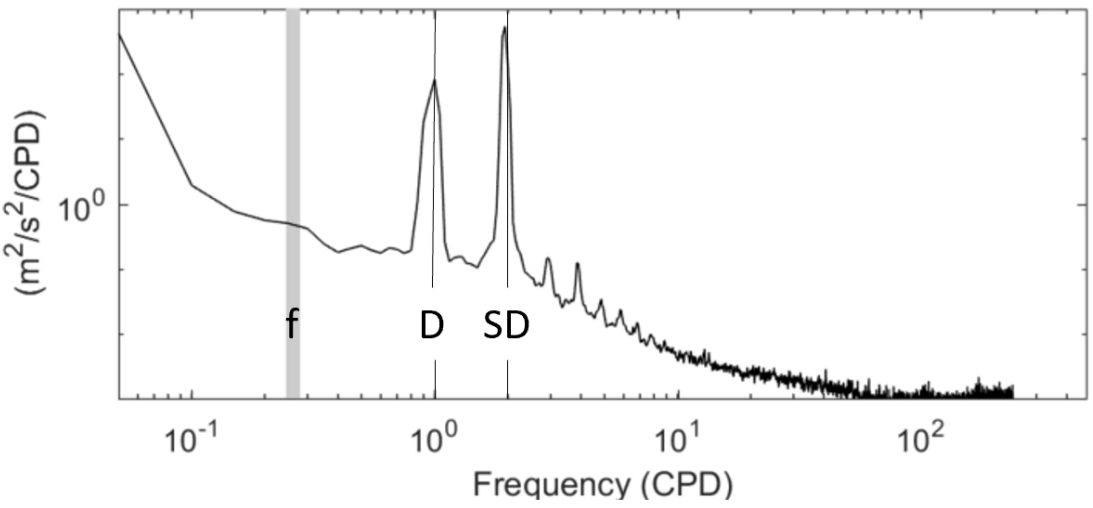

Figure 4.4: Spectra of the sea level observations made by the ADCP located on Hydrographers Bank. Elevated energy is seen at the diurnal (D) and semidiurnal (SD) bands as well as the tidal harmonics.

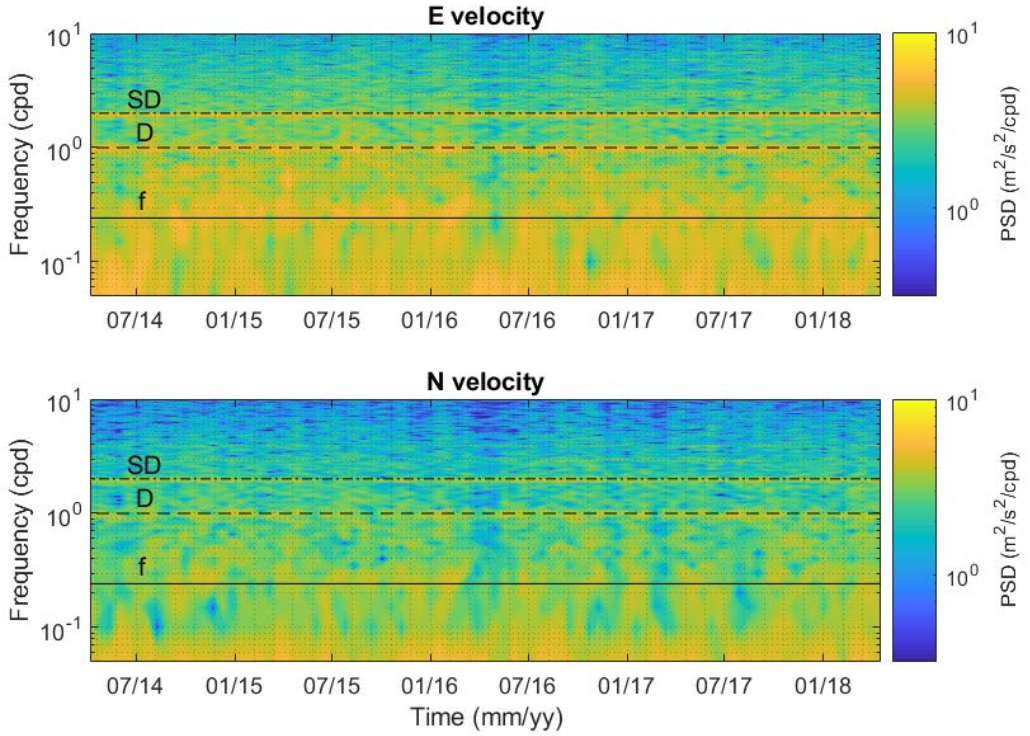

Figure 4.5: Spectrograms of depth-averaged current vectors, East (top) and North (bottom), between March 2014 and June 2018. There is elevated energy at the semidiurnal (dash dot line), diurnal (dashed line) and inertial (solid line) bands. Energy levels are higher in the E velocity component.

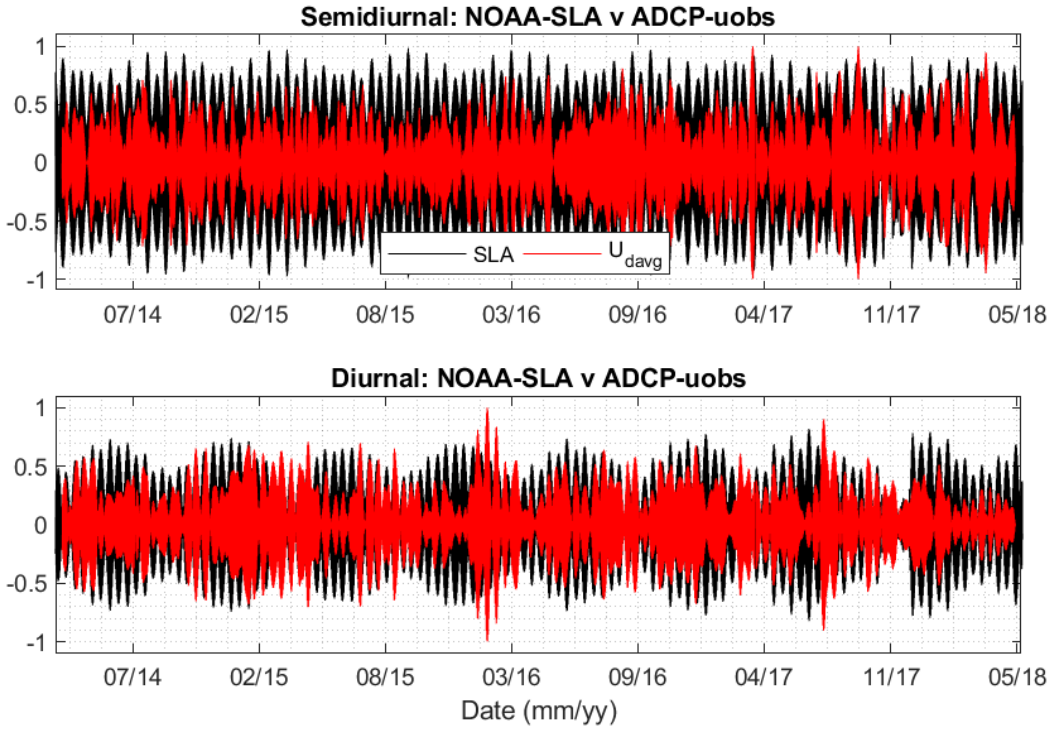

Figure 4.6*:* Top. Sea level anomaly observations from Malakal Harbor (black) and rotated depth-averaged currents (red), both normalized by their repsective variances, band passed for the semidiurnal band. **Bottom**. SLA data from Malakal Harbor (black) and rotated depth-averaged currents (red), both normalized by their respective variances, band passed for the diurnal band.

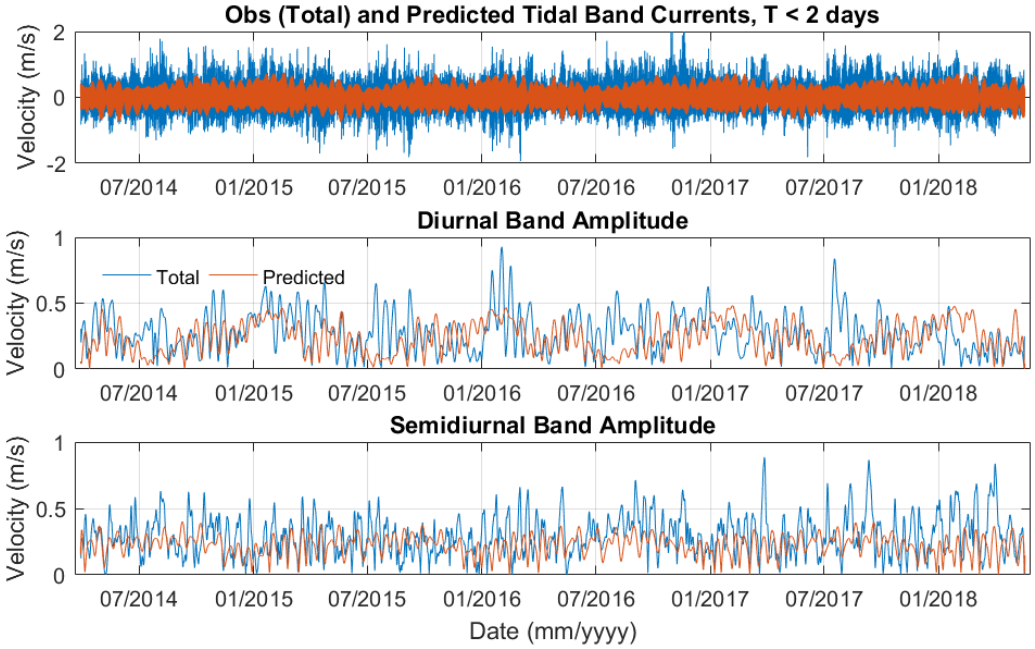

Figure 4.7: **Top**. Observed currents were high-pass filtered (blue), maintaining periods less than 2 days. Tidal constituents were computed using the observations from March 2014 through March 2015 and then tides were predicted for the whole observational window of March 2014 through June 2018 (orange). Observed and predicted tidal currents were bandpass filtered around the diurnal (**Middle**) and semidiurnal (**Bottom**) bands. Amplitude of the currents was determined using a Hilbert transform on the time series. The total amplitude of tidal band currents (blue) and predicted (orange) amplitude of the tidal band currents are shown.

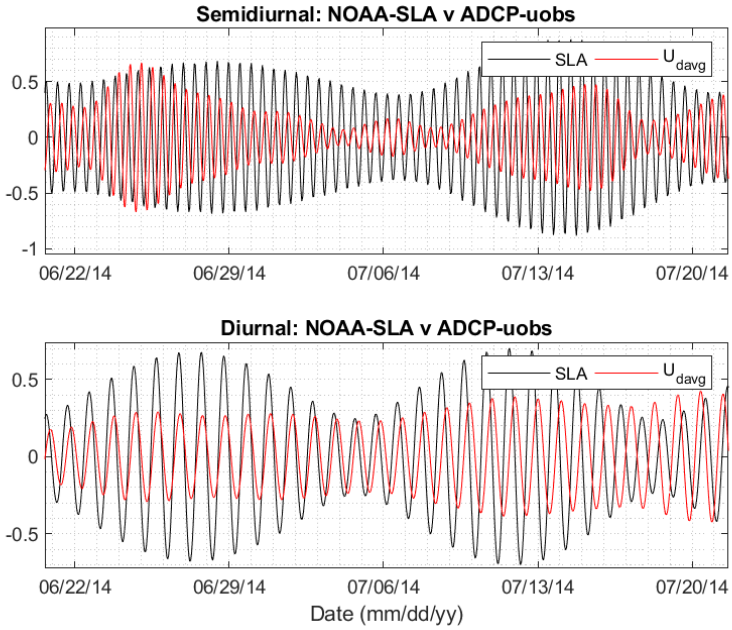

Figure 4.8*:* **Top.** The sea level anomaly observations from Malakal Harbor (black) and rotated depth-averaged currents (red), both normalized by their respective variances, band passed for the semidiurnal band. **Bottom.** SLA data from Malakal Harbor (black) and rotated depth-averaged currents (red), both normalized by their respective variances, band passed for the diurnal band.

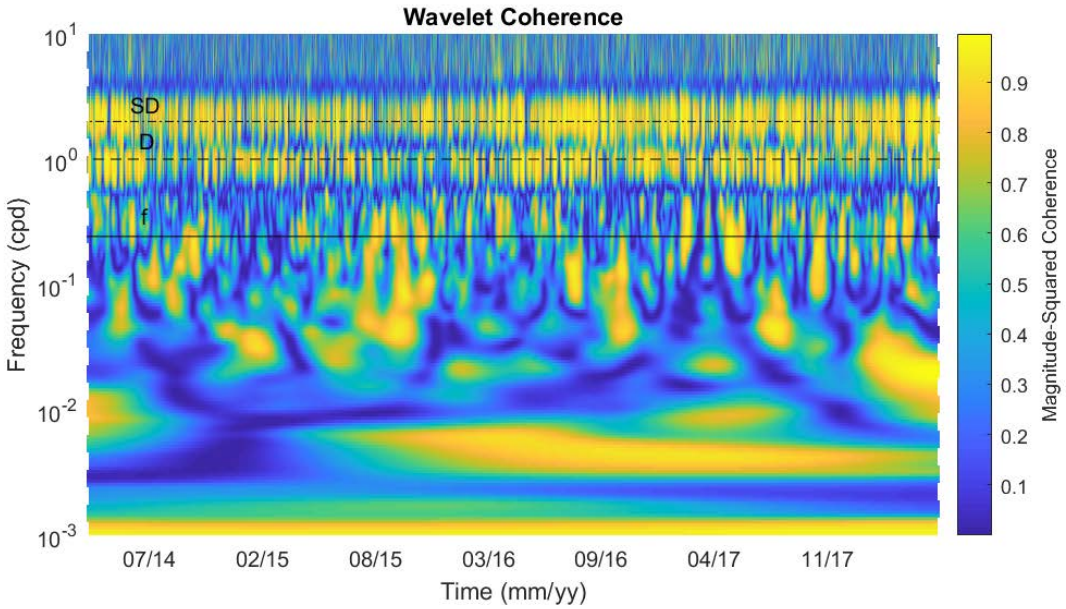

***Figure 4.9**:* Wavelet coherence is shown between the surface tide, represented by the SLA observed by the ADCP for this computation, and major-axis velocity in the semidiurnal and diurnal bands between March 2014 and March 2015. Elevated levels of coherence are seen at the semidiurnal and diurnal bands. There is no clear relationship between the variability in the coherence and the timeseries of the water level observed by the ADCP. The amplitude of the total observed and predicted tidal currents in each respective band are show in b and d.

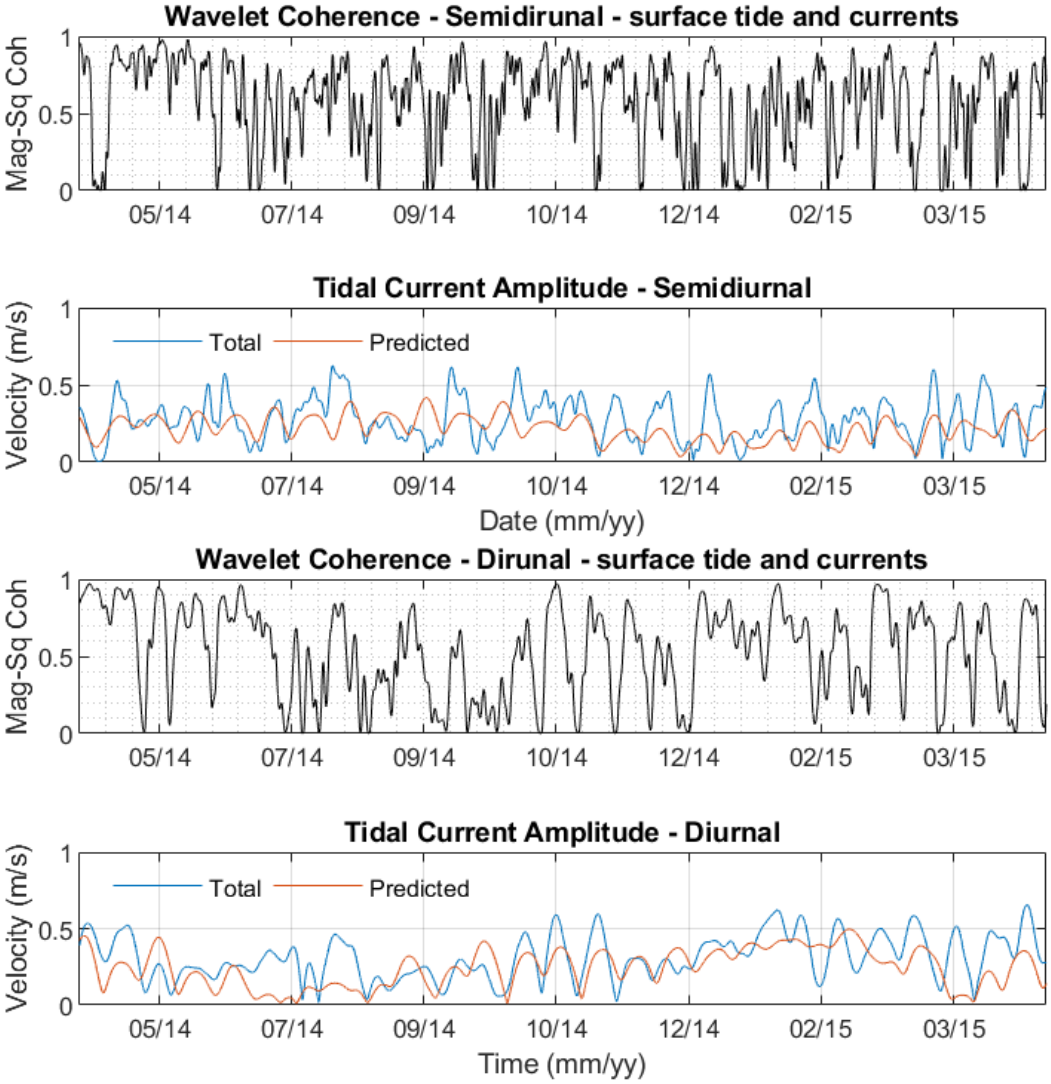

Figure 4.10: Wavelet coherence is shown between the surface tide, represented by the SLA observed by the ADCP for this computation, and major axis velocity in the (a) semidiurnal and (c) diurnal bands between March 2014 and March 2015. Elevated levels of coherence are seen at the semidiurnal and diurnal bands. There is no clear relationship between the variability in the coherence and the timeseries of the water level observed by the ADCP. The amplitude of the total observed and predicted tidal currents in each respective band are show in b and d.

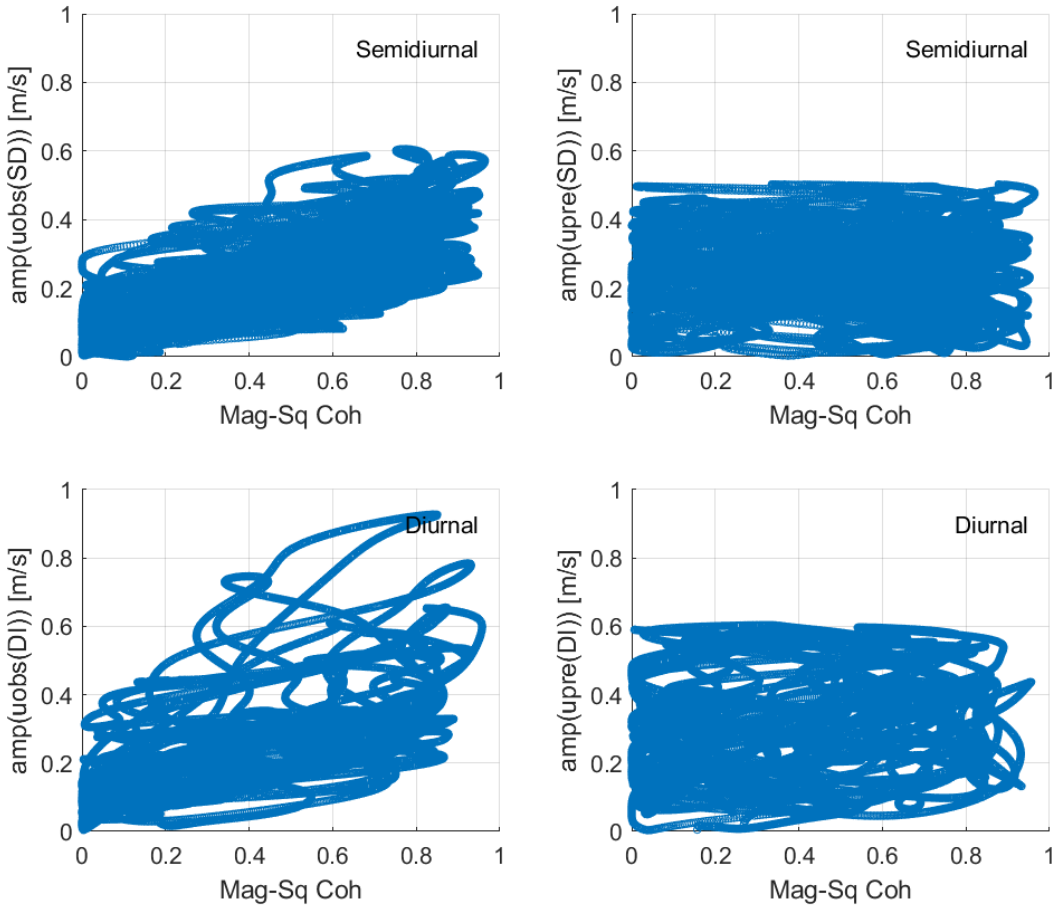

Figure 4.11*:* Wavelet coherence between SLA observed by the ADCP and tidal band currents (x-axis) versus the amplitude of the tidal band currents. Semidiurnal (top row) and diurnal (bottom row) bands both show a relationship between the coherence between the surface tide and observed tidal currents verses the amplitude of the observed tidal currents (left column). The amplitude of the predicted tidal currents (right column) do not show this same relationship.

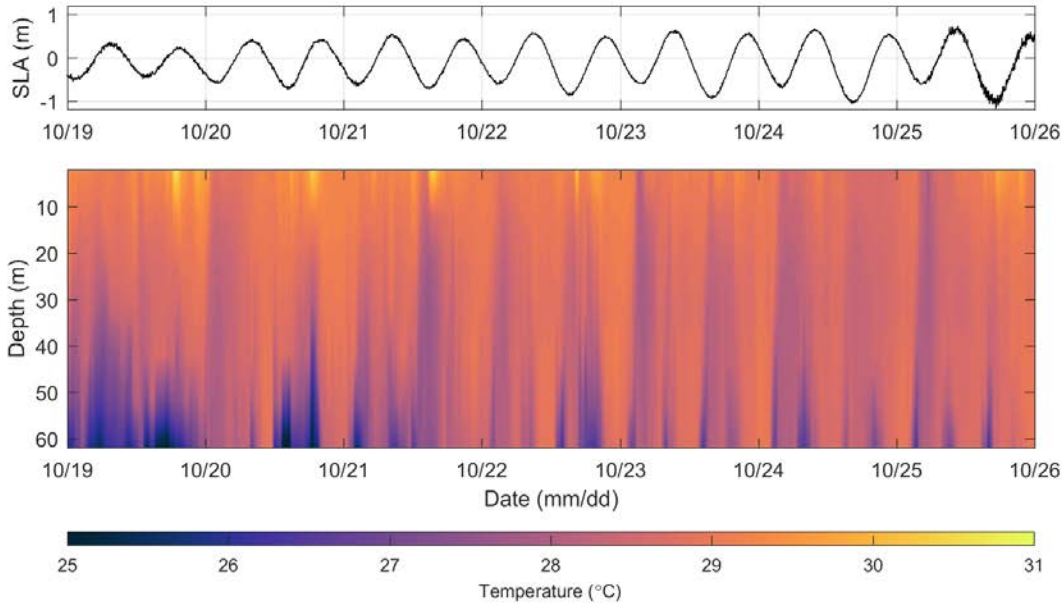

Figure 4.12*:* Sea level anomaly (top) and the depth profile of temperature at West Channel between 0 and 65 m of depth (bottom) are compared. An internal tide corresponding with peak low tide is present during this time period in October of 2014. Sea level anomaly and the zonal flows over Hydrographers Bank are positively correlated during this time period.

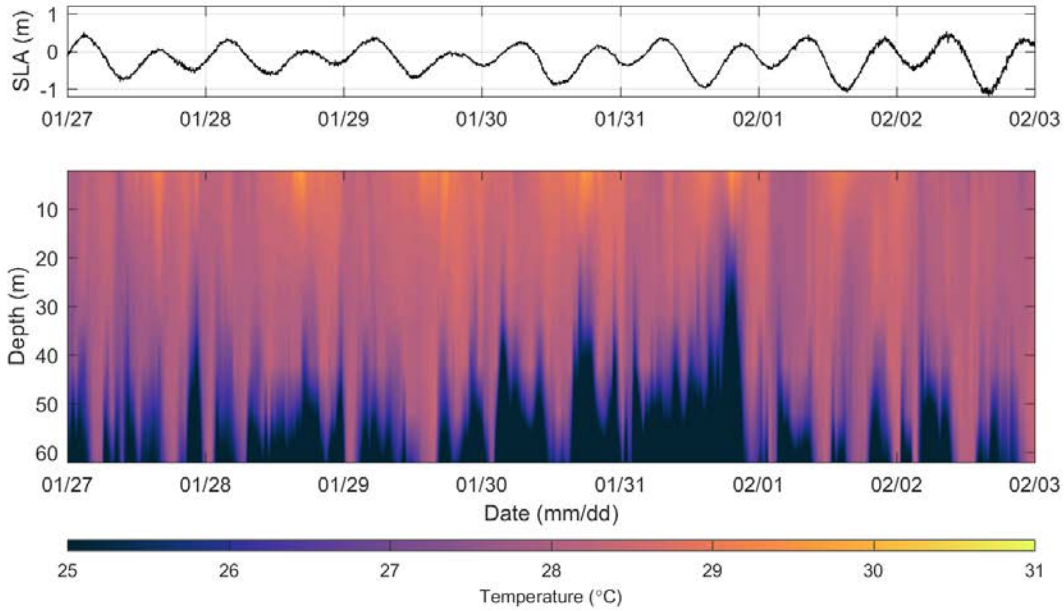

Figure 4.13*:* Sea level anomaly (top) and the depth profile of temperature at West Channel between 0 and 65 m of depth (bottom) are compared. Large amounts of internal wave driven variability is present during this time period in January and February of 2015. Sea level anomaly and the zonal flows over Hydrographers Bank are negatively correlated during this time period.

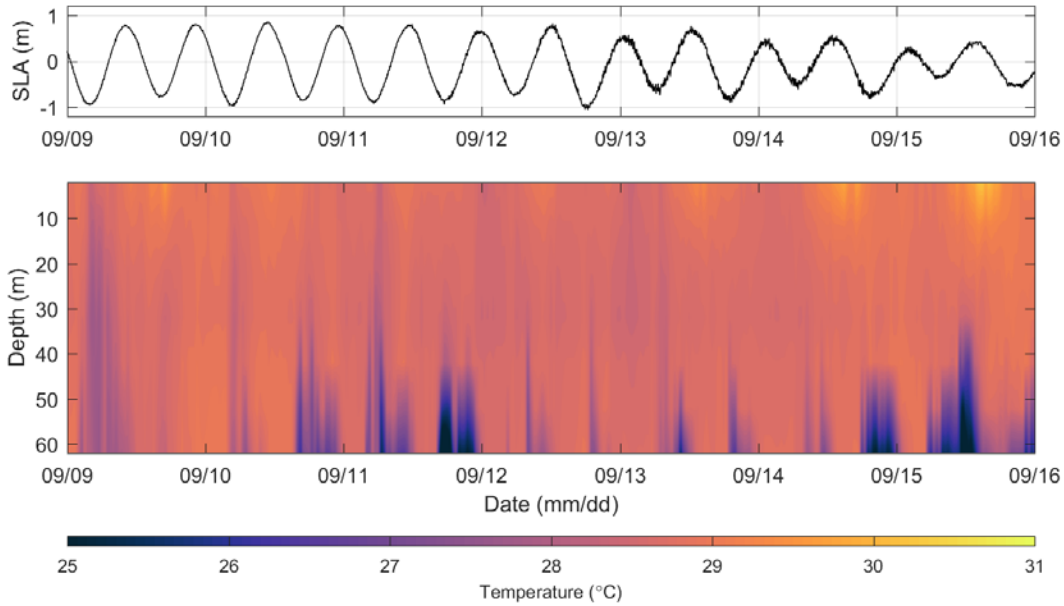

***Figure 4.14**:* Sea level anomaly (top) and the depth profile of temperature at West Channel between 0 and 65 m of depth (bottom) are compared. An internal tide corresponding with peak low tide is present during this time period in September 2014. Sea level anomaly and the zonal flows over Hydrographers Bank are not correlated during this time period.

4.6 References

Alford, M. H. (2003). Redistribution of energy available for ocean mixing by long-range propagation of internal waves. *Nature*, *423*(March), 159–162. https://doi.org/10.1038/nature01628

Caldwell, P. C., Merrifield, M. A., & Thompson, P. R. (2017). Sea level measured by tide gauges from global oceans as part of the Joint Archive for Sea Level (JASL) from 1846-01-01 to 2015-07-31. *National Oceanographic Data Center, NOAA.* https://doi.org/10.7289/V5V40S7W

Chavanne, C., Flament, P., Carter, G., Merrifield, M., Luther, D., Zaron, E., & Gurgel, K.-W. (2010). The Surface Expression of Semidiurnal Internal Tides near a Strong Source at Hawaii. Part I: Observations and Numerical Predictions. *Journal of Physical Oceanography*, *40*(6), 1155–1179. https://doi.org/10.1175/2010JPO4222.1

Colin, P. L. (2009). *Marine environments of Palau*. Taiwan: Indo-Pacific Press. Retrieved from http://coralreefpalau.org/wp-content/uploads/2017/04/Colin-PL-2009-Marine-Environments-of-Palau.pdf

Daubechies, I., Lu, J., & Wu, H.-T. (2011). Synchrosqueezed wavelet transforms: An empirical mode decomposition-like tool. *Applied and Computational Harmonic Analysis*, *30*(2), 243–261. https://doi.org/10.1016/j.acha.2010.08.002

Dumas, F., Le Gendre, R., Thomas, Y., & Andréfouët, S. (2012). Tidal flushing and wind driven circulation of Ahe atoll lagoon (Tuamotu Archipelago, French Polynesia) from in situ observations and numerical modelling. *Marine Pollution Bulletin*, *65*(10), 425–440. https://doi.org/10.1016/j.marpolbul.2012.05.041

Egbert, G. D., & Ray, R. D. (2001). Estimates of M2 Tidal Energy Dissipation from TOPEX/Poseidon Altimeter Data. *Journal of Geophysical Research*, *106*, 475–502. https://doi.org/10.1029/2000JC000699

Egbert, G. D., Bennett, A. F., & Foreman, M. G. G. (1994). TOPEX/POSEIDON tides estimated using a global inverse model. *Journal of Geophysical Research: Oceans*, *99*(C12), 24821–24852. https://doi.org/10.1029/94JC01894

Eich, M. L. (2004). Structure and variability of semidiurnal internal tides in Mamala Bay, Hawaii. *Journal of Geophysical Research*, *109*(C5). https://doi.org/10.1029/2003JC002049

Godin, G. (1972). *The Analysis of Tides* (Vol. 1). Toronto, Buffalo: University of Toronto Press.

Mitchum, G. T. (1994). Comparison of TOPEX sea surface heights and tide gauge sea levels. *Journal of Geophysical Research: Oceans*, *99*(C12), 24541–24553. https://doi.org/10.1029/94JC01640

Munk, W. H., & Cartwright, D. E. (1966). Tidal Spectroscopy and Prediction. *Philosophical Transactions of the Royal Society A: Mathematical, Physical and Engineering Sciences*, *259*(1105), 533–581. https://doi.org/10.1098/rsta.1966.0024

Munk, W. H., Zetler, B., & Groves, G. W. (1965). Tidal Cusps. *Geophysical Journal of the Royal Astronomical Society*, *10*(2), 211–219. https://doi.org/10.1111/j.1365-246X.1965.tb03062.x

Nagai, T., & Hibiya, T. (2015). Internal tides and associated vertical mixing in the Indonesian Archipelago. *Journal of Geophysical Research: Oceans*, *120*(5), 3373–3390. https://doi.org/10.1002/2014JC010592

Pawlowicz, R., Beardsley, B., & Lentz, S. (2002). Classical tidal harmonic analysis including error estimates in MATLAB using T_TIDE. *Computers & Geosciences*, *28*(8), 929–937. https://doi.org/10.1016/S0098-3004(02)00013-4

Ray, R. D., & Zaron, E. D. (2011). Non-stationary internal tides observed with satellite altimetry. *Geophysical Research Letters*, *38*(17). https://doi.org/10.1029/2011GL048617

Schramek, T. A., Colin, P. L., Merrifield, M. A., & Terrill, E. J. (2018). Depth-Dependent Thermal Stress Around Corals in the Tropical Pacific Ocean. *Geophysical Research Letters*, *0*(0). https://doi.org/10.1029/2018GL078782

Simmons, H. L., Hallberg, R. W., & Arbic, B. K. (2004). Internal wave generation in a global baroclinic tide model. *Deep Sea Research Part II: Topical Studies in Oceanography*, *51*(25), 3043–3068. https://doi.org/10.1016/j.dsr2.2004.09.015

Symonds, G., Black, K. P., & Young, I. R. (1995). Wave-driven flow over shallow reefs. *Journal of Geophysical Research: Oceans*, *100*(C2), 2639–2648. https://doi.org/10.1029/94JC02736

Wolanski, E., Imberger, J., & Heron, M. L. (1984). Island wakes in shallow coastal waters. *Journal of Geophysical Research: Oceans*, *89*(C6), 10553–10569. https://doi.org/10.1029/JC089iC06p10553

Wolanski, E., Colin, P., Naithani, J., Deleersnijder, E., & Golbuu, Y. (2004). Large amplitude, leaky, island-generated, internal waves around Palau, Micronesia. *Estuarine, Coastal and Shelf Science*, *60*(4), 705–716. https://doi.org/10.1016/j.ecss.2004.03.009

Zilberman, N. V., Merrifield, M. A., Carter, G. S., Luther, D. S., Levine, M. D., & Boyd, T. J. (2011). Incoherent Nature of M2 Internal Tides at the Hawaiian Ridge. *Journal of Physical Oceanography*, *41*(11), 2021–2036. https://doi.org/10.1175/JPO-D-10-05009.1